Development of block copolymer lithography for device structure fabrication

Ramsankar Senthamaraikannan

Department of Chemistry,

University College Cork,

Ireland.

This thesis is presented to the National University of Ireland for the degree of

Doctor of Philosophy

September 2014

Supervisor: Prof. Michael A Morris

Head of Department: Prof. Martyn Pemble

Declaration

I Ramsankar Senthamaraikannan verify that this Thesis is my own work and I have not acquired a degree in this university or elsewhere on the foundation of this Ph.D thesis.

Ramsankar. S Date:

This thesis investigated well-ordered block copolymer (BCP) thin film characteristics and their use for nanoscale pattern formation using a series of polystyrene-*block*-polymethylmethacrylate (PS-*b*-PMMA), polystyrene-*block*-polydimethylsiloxane (PS-*b*-PDMS) and polystyrene-*block*-poly(ethylene oxide) (PS-*b*-PEO) systems of various molecular weights. BCP thin films, which act as an 'on-chip' etch mask and material templates, are highly promising self-assembling process for future scalable nanolithography. Unlike conventional BCP processing methods, the work in this thesis demonstrates that well-ordered patterns can be achieved in a few seconds compared to several hours by use of a non-conventional microwave assisted technique. As a result, well-ordered BCP nanoscale structures can be developed in industry appropriate periods facilitating their incorporation into current technologies. An optimised and controlled plasma dry etch process was used for successful pattern transfer to the underlying silicon substrate. Long range ordered BCP templates were further modified by selective metal inclusion technique to form a hard mask template towards fabrication of high aspect ratio nanopillars and nanowires. The work described here is centred on how these templates might be used to generate function at substrate surfaces. Herein we describe a number of innovations which might allow their successful uptake in a number of applications.

First and foremost, I would like to thank my supervisor, **Prof. Michael A Morris** for giving me this opportunity and providing his support throughout my research. I am also thankful to ***Science Foundation Ireland*** for giving me the funding opportunity. I would like to extend my thanks to **Prof. Justin D Holmes** for giving me advices.

Heartfelt thanks to **Dr. Dipu Borah**, PDRF**,** Chemistry department, University College Cork for being along with me all the time, constantly guiding me in the research as well as in personal life.

Special thanks to **Dr. Tandra Ghoshal**, PDRF, Chemistry department, University College Cork for encouraging and guiding me throughout the research.

I am very much thankful to **Dr. Parvaneh Mokarian Tabari** and all the members of **lab 343** and **Poly Team**.

I would like to thank friend **Mr. Sozaraj Rasappa** for his valuable research support all the times in UCC, CRANN lab and in personal life.

I put my sincere thanks to D**r. Colm Macmanamon**, **Dr. Atul Thorat**, **Mr. Timothy Collins**, **Mr. Cian Cummins**, **Mr. Atul Chaudhari**, **Ms. Elsa Giraud** and **Lab- 115** researchers for excellent knowledge transfer.

I would like to extend my thanks to **Dr. Peter Fleming**, CRANN for helping me in carrying out XPS analysis.

A special thanks to **Dr. Matthias Jauch** for all the IT assistance over the past few years. I am always thankful to the administrative and technical staff of UCC-chemistry department for putting up with me for in my Ph.D: **Ms. Mary O'Neill, Ms. Eileen O'Callaghan, Ms. Colette Pettit, Ms. Christine Dennehy** and **Mr. Terry Horgan**.

My deep sense of gratitude to my initial Microscopy guide **Dr. Colm Faulkner, e**xperimental Officer, AML, CRANN**,** for his whole hearted encouragement even in holidays.

I am very much pleased to inscribe my sense of gratitude to senior experimental officer **Mr. Tarek Lutz,** AML, CRANN. I express my sincere thanks to **Mr. Cathal McCauley,** Operational manager, AML, CRANN and **Mr. Dermot Daly,** AML, CRANN**,** for their constant help throughout the completion of my Ph.D.

I would like to record my sincere gratitude to **Mr. Des Keany,** Senior attendant, CRANN and **Mr. James Dempsey**, Facilities manager, CRANN for their social support throughout this research work.

My regards further reach all the members of **Integration Group of Theme – II**, **CRANN** for constant help in my research work. I wish to express my sincere thanks to all the professors, faculty members, nonteaching staffs and friends in CRANN, Tyndall and UCC for their constant help.

I am pleased to thank **Dr. A. Nirmala Grace**, for motivating me to do Ph.D and encouraging me.

I have no words to thank my parents **Mr. R. Senthamaraikannan** and **Mrs. S. Baggiyalakshmi** who were always with me in all my success and failures. Not but not least I would like to extend my thanks to my life partner **Mrs. G. Madhura Bashini**.

Dedicated to my parents and my life partner

List of published papers

[1] T. Ghoshal, R. Senthamaraikannan, M. T. Shaw, J. D. Holmes, M. A. Morris, Nanoscale, **2012**, 4 (24), 7743-7750.

[2] T. Ghoshal, R. Senthamaraikannan, M. T. Shaw, J. D. Holmes, M. A. Morris, Advanced Materials, **2014**, 26 (8), 1207-1216.

[3] D. Borah, R. Senthamaraikannan, S. Rasappa, B. Kosmala, J. D. Holmes, M. A. Morris, ACS nano, **2013**, 7 (8), 6583-6596.

[4] S. Rasappa, D. Borah, R. Senthamaraikannan, C. C. Faulkner, M. T. Shaw, P. Gleeson, J. D. Holmes, M. A. Morris, Thin Solid Films, **2012**, 522, 318-323.

[5] D. Borah, S. Rasappa, R. Senthamaraikannan, B. Kosmala, M. T. Shaw, J. D. Holmes, M. A. Morris, ACS applied materials & interfaces, **2012**, 5 (1), 88-97.

[6] D. Borah, S. Rasappa, R. Senthamaraikannan, M. T. Shaw, J. D. Holmes, M. A. Morris, Journal of colloid and interface science, **2013**, 393, 192-202.

[7] S. Rasappa, D. Borah, R. Senthamaraikannan, C. C. Faulkner, J. J. Wang, J. D. Holmes, M. A. Morris, Science of Advanced Materials, **2013**, 5 (7), 782-787.

[8] D. Borah, S. Rasappa, R. Senthamaraikannan, J. D. Holmes, M. A. Morris, Langmuir, **2013**, 29 (28), 8959-8968.

[9] T. Ghoshal, T. Maity, R. Senthamaraikannan, M. T. Shaw, P. Carolan, J. D. Holmes, S. Roy, M. A. Morris, Scientific reports, **2013**, 3.

[10] D. Borah, C. D. Simao, R. Senthamaraikannan, S. Rasappa, A. Francone, O. Lorret, M. Salaun, B. Kosmala, N. Kehagias, M. Zelsmann, C. M. Sotomayor-Torres, M. A. Morris, European Polymer Journal, **2013**, 49 (11), 3512-3521.

[11] D. Borah, S. Rasappa, R. Senthamaraikannan, J. D. Holmes, M. A. Morris, Advanced Materials Interfaces, **2014**, 1, 1300102.

[12] S. Rasappa, D. Borah, R. Senthamaraikannan, C. C. Faulkner, J. D. Holmes, M. A. Morris, Journal of Nanoscience and Nanotechnology, **2014**, 14 (7), 5221-5227.

1-D – One-Dimensional

AFM – Atomic Force Microscopy

AOE – Advanced Oxide Etch

ARDE – Aspect Ratio-Dependent Etching

BCP - Block copolymer

DC – Direct current

DI – De-ionized

DSA - Directed Self-Assembly

FFT – Fast-Fourier Transforms

FIB – Focused Ion Beam

FTIR - Fourier Transform Infra-Red

HMDS – Hexamethyldisilazane

HO-PS-*r*-PMMA - Hydroxyl-terminated polystyrene-*r*-polymethylmethacrylate

ICP - Inductively Coupled Plasma

IPA - Iso-propanol

ITRS – International Technology Roadmap for Semiconductor

LPCVD – Low-Pressure Chemical Vapour Deposition

M_n – Molecular weight

M_w/M_n – Polydispersity index

NIL - NanoImprint Lithography

NBOHCs – Non-Bridging Oxygen Hole Centers

ODT – Order-to-Disorder Transition

PDMS - polydimethylsiloxane

PDMS-OH - Hydroxyl-terminated polydimethylsiloxane

PL – Photo Luminescence

PMMA - polymethylmethacrylate

PMMA-OH - Hydroxyl-terminated polymethylmethacrylate

PS-*b*-PDMS - polystyrene-*block*-polydimethylsiloxane

PS-*b*-PEO – polystyrene-*block*-poly (ethylene oxide)

PS-*b*-PMMA - polystyrene-*block*-polymethylmethacrylate

PS – Polystyrene

PS-OH - Hydroxyl-terminated polystyrene

RF – Radio Frequency

RIE - Reactive Ion Etching

Si - Silicon

SIA – Semiconductor Industry Associations

SEM - Scanning Electron Microscopy

SOI – Silicon-On-Insulator

T_g – Glass transition temperature

TEM – Transmission Electron Microscopy

TMS - Trimethylsily

XPS - X-ray Photoelectron Spectroscopy

1. Perspective challenges and its solutions for semiconductor industry

In the last decade we have seen a tremendous increase in the widespread use of semiconductor devices and these have had a great influence in our day to day life. Semiconductor industries follow a roadmap produced every year by a group of semiconductor industry experts in the Semiconductor Industry Associations (SIA) called the International Technology Roadmap for Semiconductors (ITRS) which acts as a driving technology reference for the semiconductor industry. It also ensures that cost-effective advancements are made in the performance of the integrated circuits (ICs) and the products that employ such devices, thereby continuing to maintain the health and success of the semiconductor industry. Its' objective is to consider the challenges in semiconductor technology and provide solutions to the satisfaction of Moore's Law **[1]**. Moore's Law predicts that the number of transistors on ICs increases exponentially, doubling approximately every 18 months. The increased speed, processing capability and low power use of these devices leads to strong increases in demand for electronic devices and this in turn leads to continued scaling of transistors **[2, 3]**. Transistor scaling has been achieved by top-down light lithography using a ultraviolet wavelength at 193 nm **[4, 5]**.

Conventional ultra violet photolithography is the most common top-down approach for fabrication of device structures in ICs **[6]**. However, the current photolithographic process is limited by the available photoresist materials and by wavelength of light used to attain smaller feature size. So, it is becoming technically challenged for future technology nodes (which are below 14 nm pitch), demanded by the semiconductor industry. Using shorter wavelength (deep-UV and x-ray) to achieve better resolution is hindered by the lack of readily available light sources at those wavelengths **[7-9]**. Even as such sources become available, other problems such as line edge roughness and critical dimension control might hinder further shrinking of features that could be patterned. The other top-down processes like nanoimprint lithography **[10]** and electron beam lithography which are capable of fabricating nanopatterns below 45 nm suffer from low throughput and high fabrication cost.

Other disadvantages of photolithography are that it is becoming time consuming and becoming an even more complicated component of the fabrication

process. In order to overcome these issues in top-down lithography other process called the bottom-up lithographic approach may prove to be significant **[11]**. Bottom-up approaches to nanofabrication use chemical or physical forces operating at the nanoscale between molecules or objects to assemble basic units into larger structures. As device size reduces, these bottom-up approaches may provide an increasingly important compliment to top-down techniques **[12]**. Bottom-up nanofabrication processes involve spontaneous self-assembly. Lithographic methods can be developed using the bottom-up approach of self-assembly and materials such as block copolymers, colloidal particles, biocompatible materials **[13]** can generate pattern through local chemical interactions between molecules or particles. These patterns formed can then be used as an on-chip mask for transfer of the patterns to the substrate. Block copolymers are perhaps the most popular materials for self-assembly in device fabrication. Here chemically distinct blocks microphase separate from each other to form nanoscale domains in a regular periodic structure **[11]**. Microphase separation is a spontaneous development in a polymer solution or melt of block copolymer of micro- and nanoscale regions (domains) with predominant content of segments (sections) of just one type which results in development of organised structures. The main advantage of self-assembly using block-copolymers is that it is cost effective and conceptually an easier fabrication method compared to the current, complex photolithography technique **[12, 11]**. We believe that block copolymer lithography may provide a variable form of device manufacture if combined with a conventional or novel form of top-down lithography.

1.2. Diblock copolymers and their phase diagram

In general, polymers are made by polymerizing many identical, similar, or complementary monomers into molecular chains. Copolymers, also called heteropolymers, are polymers with two (or more) different types of monomers in molecular chains and they can be categorized into several types based on the way monomers are arranged along chains: random copolymer, alternating copolymer, graft copolymer, and block copolymer. This thesis deals with block copolymers which consist of two blocks of different polymerized monomers which are covalently connected each other **[14, 15]**. These can be properly described as

"diblock copolymer". The blocks in diblock copolymer will tend to phase separate into nanodomains forming different mesophase structures when the incompatibility of the different blocks provides a shorter range repulsive interaction. **Scheme 1.1** depicts the schematic of diblock copolymer where two monomers A and B are covalently bonded.

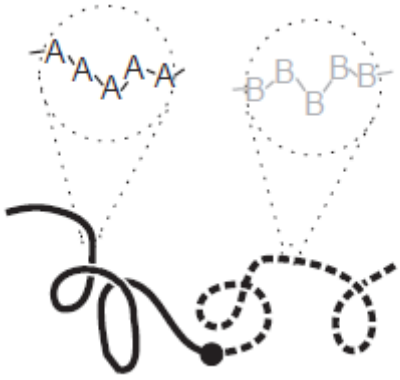

Scheme 1.1. Schematic of diblock copolymer where block A monomer and block B monomer are covalently bonded

The possible block copolymer nanostructures that are formed originate from the molecular weight of each of the blocks. The structures or morphologies formed minimize the block-block repulsions (since they are chemically dissimilar) by minimizing the interfacial area between the blocks. Various morphologies of diblock copolymers, such as lamellar, double diamond, double gyroid, cylindrical, and spherical morphologies, can be obtained depending on the composition, as shown in **Figure 1.1(a). Figure 1.1(b)** shows the different phases formed by self-assembly of diblock copolymers in the bulk (when the intermolecular interaction between blocks is sufficiently large) as a function of the volume fraction of one of the blocks (f). This thesis deals only with diblock copolymers forming lamellar and cylindrical morphologies which lead to device structure formation.

The critical parameters of phase separation of block copolymer are:

f = volume fraction of one block (the minority block)

χ = Flory-Huggins interaction parameter, which is inversely proportional to temperature. The Flory-Huggins interaction parameter is a measure of the chemical dissimilarity of the blocks.

N = degree of polymerization.

When χN is large, there is a large incompatibility between the two blocks and phase separation is favoured.

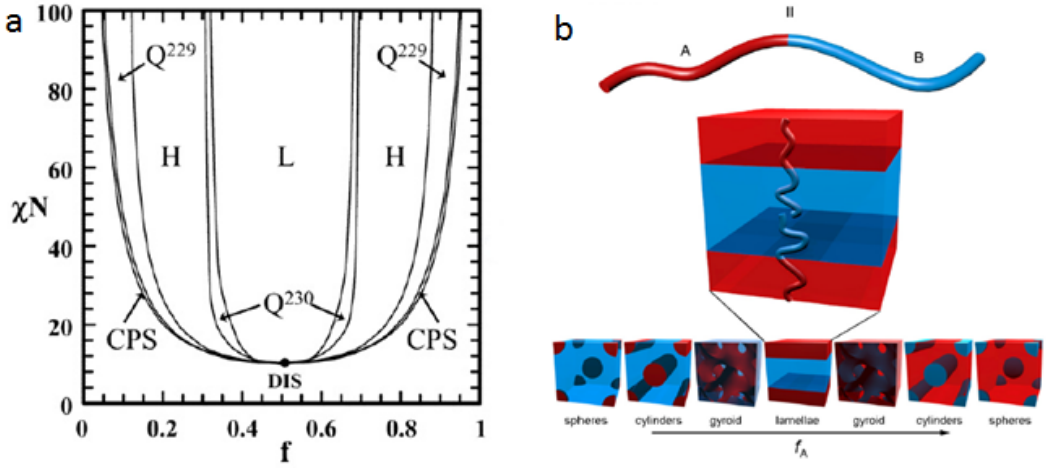

Figure 1.1. (**a**) Phase diagram of diblock copolymer as a function of volume fraction of A **[16]**. (**b**) Schematic diagram of structures forming as a function of A **[17]**. Where, L: lamellae, H: hexagonally packed cylinders, Q230: double-gyroid phase, Q229: body-centered spheres, CPS: closed-packed spheres and DIS: disordered.

The structure range from close packed spheres (fA:fB ~ 80:20), to cylindrical rods (fA:fB ~ 70:30) and lamellae (fA:fB ~ 50:50). As sufficiently high fA, they form the inverse structures. Though other more complex features i.e. double gyroid can be formed, the most interesting for lithography applications are the regular ordered structures.

It is possible to control the microstructures and hence macroscopic properties of the BCP by changing the molecular properties of the polymer. The entropic component of phase behaviour is determined by N and fA, while the enthalpic component is determined by χ. When N is large, there is an energy advantage to losing configurational entropy by local ordering to reduce the contact between the A and B blocks and phase separation occurs **[6]**. When $\chi$is large, there is a large incompatibility between the two blocks and phase separation is favoured. Lowering the temperature has the effect as increasing χ. The conditions for ordering are described by an order-to-disorder transition (ODT) that dependent on N, χ, and the temperature and can be quantified by the term χN which determines the degree of microphase separation. Depending on χN, two different regimes can be

distinguished: the weak-segregation limit (WSL) for $\chi N \leq 10.5$, with the future size given by D $\dot{\alpha}N^{½}$and the strong segregation limit (SSL) for $\chi N >> 10.5$, with the future size D $\dot{\alpha}\, \chi^{1/6}\, N^{2/3}$. The focus of this thesis will be on diblock copolymers in the strong segregation limit, where well-ordered phase behaviour is exhibited.

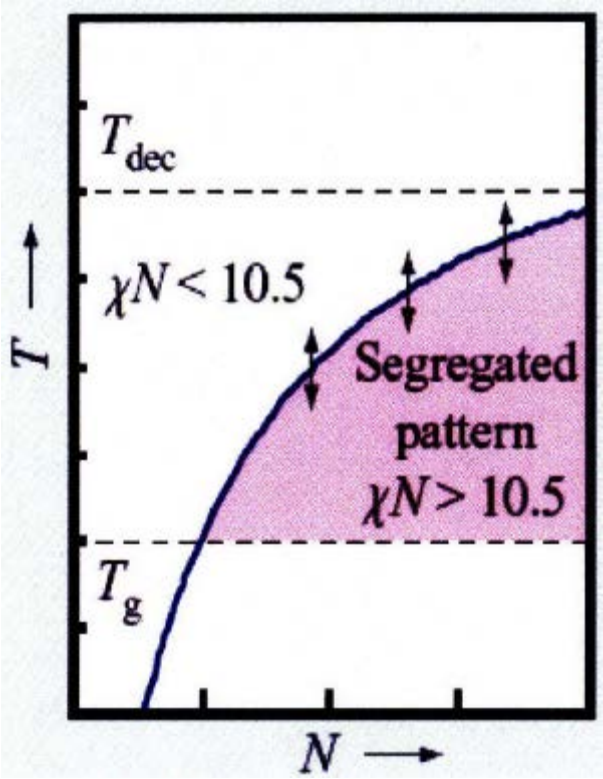

Figure 1.2. Phase diagram for forming a segregated pattern in BCP films.

In order for ordering to occur, χN must be greater than 10.5. **Figure 1.2** graphically describes the conditions for ordering based on temperature and molecular weight. The temperature must be above the glass transition temperature (T_g) of the block copolymer to allow sufficient mobility for reorganization. However, above the decomposition temperature (T_{dec}), the polymer will degrade. Therefore, the stability of the segregated pattern decreases with increasing temperature and a minimum N must be met for self-assembly to occur. It is possible for ordering to occur above the bulk order-disorder temperature (T_{odt}) by modifying the surface energy of the substrate to cause preferential adsorption of one block and subsequent patterning of the thin film block copolymers **[7]**.

1.3. Block copolymer as thin film

The block copolymer thin film is prepared using techniques like spin casting, spin coating and dip coating. The most common method for film deposition is spin coating since this provides regular thickness over large areas. The block copolymer is dissolved in a solvent that is mutually suitable for both blocks to form a low weight percentage polymer solution. Then the solution is deposited on a substrate via spin coating. The polymer film is deposited on a substrate with uniform thin films over large areas with low surface roughness. Spin speed, concentration of the block copolymer solution and solvent volatility are the factors that control the film thickness and uniformity. Faster spin speeds reduce film roughness while increased solvent volatility results in increased roughness **[18]**. Finally, annealing at elevated temperatures causes spontaneous ordering of the structures. Solvent annealing can be used to lower the glass transition temperature (T_g) of both blocks to enhance chain movement so that annealing can occur at lower temperatures **[19]**. However, the self-assembly processing times can be inordinately long and for it to be introduced into manufacturing there is a need to reduce these times from the usual hours to minutes. With the help of microwave annealing the structures organize themselves into very regular patterns extremely quickly – reducing the processing time from days to less than few minutes **[20]**. As will be seen here a BCP thin film can be used as a promising template for metal or metal oxide nanostructure fabrication.

1.4. Directed self-assembly

Directed self-assembly (DSA) is the process to improve the pattern quality and attain the well aligned long-range ordered nanopatterns. Grapheoepitaxy (physically patterned) **[21]** and chemoepitaxy (chemically patterned) **[22]** are the two main categories of DSA. In this thesis we are only focused on graphoepitaxy substrates which are patterned using either e-beam lithography or conventional photolithography (from Intel). One of the main advantage of DSA is defect density will be significantly reduced and the number of features patterned within the trenches can be determined using the trench width. Side walls of the physically patterned substrates can be modified using brush chemistry **[23]**. These DSA methods provide very much increased periodicity compared to the nanostructures

fabricated on the planar substrates. Graphoepitaxy has a wide range of application for e.g. in the field of recording media dot patterns where it is notably the most well-developed commercially **[24]**. Nanostructures fabricated using DSA can be locally determined using fixed positions on a substrate and other great advantage towards real device fabrication in the aspect of interconnecting the multiple layers which are fabricated using conventional optical lithography. It is essential to establish strict methods to control the morphology of BCPs, since some applications require addressability and the BCP microdomains must be perfectly aligned and oriented.

1.5. Surface functionalization

Brush chemistry is one of the major research fields in block copolymer lithography for controlling orientation of microphase separation. BCP systems offer excellent control over pattern dimension and structure, lamellar, cylindrical, spherical and gyroid (as shown in **Figure 1.1)**. However, the use of BCP methods can prove a challenge because the interfacial interactions of the polymer blocks with the substrate and the environmental can influence pattern formation and, in particular, pattern orientation for use of BCP in lithography. In cylinder or lamellae forming BCP systems the micro domain orientation can be either parallel or vertical to the substrate surface plane depending on preferential interface interactions of the blocks or surface energy effects. Very frequently, a perpendicular domain orientation in thin films is desirable so it can be used as an effective template or mask for substrate feature development as outlined above **[25]**. The use of a host of methods such as solvent annealing, thermal annealing, and electric field application, homopolymer blending and chemical modification of substrate is used to improve the wetting behaviour and to control the interfacial and surface energies to control surface coverage and pattern orientation **[26]**. The concept of attaching random copolymers to a substrate surface as a ‘brush’ so that surfaces neutral to both blocks can be created is well established **[27]**. Molecular grafting of random copolymers like HO-PS-*r*-PMMA, HO-PS-*r*-PDMS (note r indicates a random arrangement of the polymer units), PS-OH and PDMS-OH to a substrate surface can result in a thin, uniform and non-preferential (i.e. chemically neutral to both blocks) brush layer. The brush enables the control of wetting behaviour and interfacial interactions of the

diblock copolymer components and the substrate. It, thus, defines a perpendicular or parallel orientation of the pattern. Brush chemistry is well developed. For the BCP system of PS-*b*-PMMA and the relative composition of the HO-PS-*r*-PMMA brush layer has been carefully tuned to define maximum order **[28]**.

Andreozzi *et al.,* **[29]** have studied brush effects on the dimensions and orientation of cylinder forming PS-*b*-PMMA noting strong cylinder diameter changes. The PS-*b*-PMMA system has particular relevance to the microelectronics industry as a potential alternative to conventional photolithography (since PS and PMMA are used as resists in current fabrication) and it is of considerable interest to understand the interaction and the effect of the polymer brush with the pattern forming BCP. PS-*b*-PDMS (polystyrene-*b*-polydimethylsiloxane) is also a potential BCP system for creation of large area alignment. For the PS-*b*-PDMS BCP system two major issues arise: strong surface dewetting due to high hydrophobicity and difficulties in controlling feature orientation, particularly, for definition of parallel versus vertical cylinder alignment. To overcome these limitations, a surface pre-treatment with a PDMS brush is usually required. However, it should be noted that whilst the use of a PDMS brush can improve these BCP thin films, dewetting the BCP coverage at the substrate and regions of irregular thickness can remain problematic as reported here and elsewhere **[28]**. However, despite the imperfect nature of these potentially important films, reports of methods of tuning the surface chemistry of PDMS brush in an effort to improve the BCP film and control orientation is scant. In order to improve the brush chemistry using simple, reproducible and facile processing we have developed a methodology using hexamethyldisilazane (HMDS) exposure to facilitate highly regular self-assembly of this PS-*b*-PDMS system over large substrate areas **[30]**. Results are highly promising and proves the ability of the technique to yield an “on-chip mask” for etch transfer to the substrate surface.

1.6. Pattern transfer

As we have said earlier, the ITRS clearly points to a number of solutions to overcoming barriers to ultra-small (<14 nm) feature size **[31]**. One of these involves the use of directed self-assembly where chemical interactions between moieties

results in the spontaneous formation of a regular pattern at a substrate surface. These patterns then act as a resist for transfer to a device layer essentially acting as an "on-chip" etch mask **[31]**. However, as feature size decreases high-fidelity pattern transfer is becoming more challenging and this form of chemical patterning will be used to illustrate some of the more interesting challenges facing plasma etch methodologies in the next few years **[32]**.

Plasma etch technology is a versatile way of pattern transferring to underlying silicon substrates using the BCP as a sacrificial layer. In conventional photoresist based lithography, it can be challenging to transfer the patterns to substrate, since it includes two to three etch methodologies **[33]**. Whereas, in BCP lithography, it is conceptually a quite straight forward single etch process. BCP techniques can be a breakthrough for UV lithography as they can develop a soft mask in sub 10 nm region. Plasma etch techniques for application in BCP soft mask structures is highly promising and reported in many of our papers with high quality aspect ratio silicon nanowire structures demonstrated. In this thesis, **chapter 6** deals with the fabrication of vertical nanowire silicon nanopillar and nanowire arrays **[34]** with high aspect ratio and **chapter 7** details the fabrication of ordered horizontally aligned silicon nanowires **[35]**.

A plasma is a partially ionized gas containing, ions, radicals and neutrals. The energy to create the plasma is obtained via the coupling of an external magnetic field to the plasma gas. Industrial IC manufacture has been realized by two plasma etching techniques; RIE (Reactive Ion Etching) and ICP (Inductively Coupled Plasma) methods. RIE has been summarized by, e.g., Jansen *et al* **[36]**. A RIE apparatus consists of a glow-discharge-generated plasma where gas molecules (e.g. SF_6 for silicon etching) are dissociated and ionized to create reactive species. Substrates are placed on a RF (radio frequency) driven, capacitively coupled electrode to generate a DC (Direct Current) bias at the sample. Reactive species, such as fluorine radicals and ions, impinge on the surface creating volatile silicon species. In most practical processes, RIE is actually a combination of the reactive species reactions that are highly species selective and ion bombardment where the reaction is a physical process caused by kinetic energy transfer. Radical etching (or true plasma etching) is limited to neutral radicals and the plasma is normally excited by microwaves. These

plasma etches are chemical in nature and can have very high selectivity and impart little damage. They are in essence 'isotropic'. This type of selective etch is used to remove photoresist after pattern transfer. One of the main challenges will be how to produce topographic features in a substrate with high fidelity and low roughness when mask materials may not be of ideal composition or thickness. High aspect ratio (depth/feature size) features require 'anisotropic' etches and is achieved using plasmas that generate both radicals (i.e. chemical selectivity) and ions (physical removal of substrate species) and is described by the generic term RIE. Schematic representation of difference in isotropic and anisotropic etching is shown in **Scheme 1.2.**

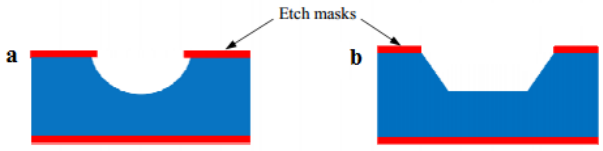

Scheme 1.2. Schematic depicting the difference between (**a**) isotropic and (**b**) anisotropic etching **[46].**

In RIE, plasma exposure develops a negative charge at the substrate from electrons produced in the plasma. This charge accelerates positive ions towards the surface in a direction normal to the surface plane. This ion bombardment occurs causing accelerated substrate removal as well as roughening the surface to create more reactive surfaces. In order to achieve higher ion bombardment rates the RIE plasmas are characterized by low plasma potentials (<100 V) and high RF biases (>500 V) compared with conventional plasma etching where there is only low sample bias (<10 V).

Sidewalls of the features formed at the substrate are largely unaffected by the bombardment process (due to physical shadowing) and so the sidewalls etch at a much lower rate than the substrate base allowing high aspect ratio features to be generated with vertical sidewalls and little change in resist feature size and spacing **[27]**. It is important to note that RIE is a true combinatorial technique in that etch rates for RIE are higher than the total etch rate that might be achieved by ion beam and chemical etching separately **[38]**. Etch directionality in RIE can be achieved in two main ways. The first of these is simple ion-induced RIE where ion modification of the exposed surface leads to enhanced removal **[39]**. The most common technique

in the microelectronics industry is ion-inhibition RIE where the as-created sidewalls are coated with a passive film that resists etching **[36]**. This film can be created by the use of gases that, e.g., form stable non-volatile carbon halogen materials **[40]**, trapping volatile silicon products at the trench walls by cryogenic cooling **[41]**, using gases (e.g. C_4F_8) that form polymeric barrier layers **[42]** and erosion/re-deposition of mask materials such as metal halogens. Typical examples are chlorine- and bromine-based silicon etches, whilst SF_6–O_2 based plasmas can also be used as anisotropic etches. An ever more important issue in RIE is aspect ratio-dependent etching (ARDE) **[43, 44]**. This has been important in micromachining for some time as high-aspect-ratio features are required.

However, as device feature size reduces, the issue of pattern transfer is becoming a general problem in nanocircuitry fabrication. ARDE describes the loss of fidelity that occurs in small feature sizes where the feature width is comparable to or less than the feature depth. ARDE is a result of several issues, e.g. deflection via ion scattering of ions towards the sidewall, diffusion effects in reactants/product reaching/leaving the base of the feature and diverging electric fields in the feature. The ICP technique can achieve much higher etch rates than RIE etching as they can operate at high plasma densities **[45]**. In comparison with RIE tools where the RF frequency is capacitively coupled to the plasma gas, in an ICP etcher power is input inductively. ICP etchers have their impedance matched to the plasma and consequently achieve high coupling efficiency between the plasma electrons and the applied field. Further, the plasma is much more controllably contained in ICP tools which further improve efficiency. ICP tools operate at low pressures (<20 mT) which have important consequences. The general principles of plasma etching described above (such as etch chemistry, etch anisotropy and sidewall modification) for RIE are maintained for ICP systems but there are proven advantages of the ICP technique. The low pressure improves diffusion of reactive species into small features enhancing the rather low etch rates achieved by RIE in very small feature sizes. It also reduces ion scattering and so improves the anisotropy of an etch. There are also distinct disadvantages of the ICP etch process. The low pressure reduces selectivity of the etch process and so results in mask damage and removal. The use of thick etch masks limits feature depth. For these reasons, combination ICP – RIE

etch tools are frequently used to achieve optimum results. In this work we have made particular effort to not only show pattern transfer but also pioneer pattern transfer.

The data in the following chapters are organized in the following way. ***Chapter 2 & 3*** centres on pattern formation using PS-*b*-PDMS self-assembly using various random copolymer brushes and HMDS monolayer on silicon. ***Chapters 4*** describes how substrate features may be produced in few seconds of microwave annealing using PS-*b*-PDMS and PS-*b*-PMMA. ***Chapters 5 & 6*** deals with the fabrication method of vertical and horizontal arrays of silicon nanopatterns formation using *insitu* hardmask from PS-*b*-PEO templates towards technological applications. ***Chapter 7*** provides an overall summary of the work and future perspective.

All the following chapters have been published in part or whole in peer-reviewed journals.

1.7. Reference

[1] Mack, C. A.; *IEEE T* Semiconduct *M*. **2011**, 24, 202.

[2] Freebody, M.; *Photonic Spectra* **2011**, *45*, 45.

[3] Mack, C. A.; *IEEE Trans. Semicond. Manuf.* **2011**, *24*, 202.

[4] Jeong, S. J.; Moon, H. -S.; Shin, J.; Kim, B. H.; Shin, D. O.; Kim, J. Y.; Lee, Y. -H.; Kim, J. U.; Kim, S. O.; *Nano Lett.* **2010**, *10*, 3500.

[5] Farrell, R. A.; Fitzgerald, T. G.; Borah, D.; Holmes, J. D.; Morris, M. A.; *J. Mol. Sci.* **2009**, *10*, 3671.

[6] Ito, T.; Okazaki, S.; *Nature* **2000**, *406*, 1027.

[7] Wissen, M.; Bogdanski, N.; Moellenbeck, S.; Scheer, H. C.; *In Strategies for Hybrid Techniques of UV Lithography and Thermal Nanoimprint* **2008**.

[8] Chung, S.; Felts, J. R.; Wang, D.; King, W. P.; De Yoreo, J. J.; *Appl. Phys. Lett.* **2011**, *99*, 193101.

[9] Yang, L.; Lee, D. H.; Chen, H. Y.; Chang, C. Y.; Liu, S. D.; Huang, C. C.; *VLSI Symp. Tech. Dig.* **2004**, 196.

[10] Li, Z.; Chen, Y.; Li, X.; Kamins, T. I.; Nauka, K.; Williams, R. S.; *Nano Lett.* **2004**, *4*, 245.

[11] Borah, D.; Shaw, M. T.; Rasappa, S.; Farrell, R. A.; O'Mahony, C. T.; Faulkner, C. M.; Bosea, M.; Gleeson, P.; Holmes, J. D.; Morris, M. A.; *J. Phys. D: Appl. Phys.* **2011**, *44*, 174012.

[12] Banerjee, S.; Elakkumanan, P.; Chidambarrao, D.; Culp, J.; Orshansky, M.; *Proc. SPIE*. **2008**, *6925*, 59250K.

[13] Hamley, I. W.; *Angew. Chem. Int. Edit.* **2003**, *42*, 1692.

[14] Bates F.S.; and Fredrickson, G.H.; *Phys.Today.* **1999**, 52, 32.

[15] Bates, F.S.; *Annu. Rev. Phys. Chem.* **1990**, 41, 525.

[16] Cochran, E.W.; Garcia-Cervera, C.J.; Fredrickson, G.H.; *Macromolecules*, **2006**, *39*, 2449.

[17] Botiz, I.; Darling, S. B.; *Mater. Today*, **2010**, *13*, 42.

[18] Strawhecker, K.E.; Kumar, S. K.; Douglas, J. F.; and Karim, A.; *Macromolecules*, **2001**, 34, 4669.

[19] Sinturel, C.; Vayer, M.; Morris, M. A.; Hillmyer, M. A.; *Macromolecules*, **2013**, 6, 5399.

[20] Xiaojiang, Z.; Kenneth, D.H.; Nathanael. L.Y. Wu.; *ACS Nano*, **2010**, 11, 7021.

[21] Guerrero, D, J.; Hockey, M. A.; Wang, Y.; Calderas, E.; *Proc. SPIE 86801*, 2013, March 26, **2013**.

[22] Delgadillo, P.; Gronheid, R.; Thode, C. J.; et. al.; *J. Micro/Nanolith. MEMS MOEMS*. **2011,** 3, 0313021.

[**23**] Borah, D.; Rasappa, S.; Senthamaraikannan, S.; Kosmala, B.; Shaw, M. T.; Holmes, J. D.; and Morris, M. A.; *ACS Appl. Materials & Interfaces,* **2013**, 5, 88.

[24] Yang, X. M.; Xiao, S.; Hsu, Y.; Feldbaum, M.; Lee, K.; and Kuo, D.; *Journal of Nanomaterials*, **2013**, 2013, 1.

[25] Rasappa, S.; Borah, D.; Senthamaraikannan, R.; Faulkner, C. C.; Shaw, M. T.; Gleeson, P.; Holmes, J. D.; Morris, M. A.; *Thin Solid Films,* **2012**, 522, 318.

[26] Farrell, R. A.; Petkov, N.; Shaw, M. T.; Djara, V.; Holmes, J. D.; Morris, M. A.; *Macromolecules*, **2010**, 43, 8651.

[27] Mansky, P.; Liu, Y.; Huang, E.; Russell, T. P.; Hawker, C.; *Science*, **1997**, *275*, 1458.

[**28**] Borah, D.; Rasappa, S.; Senthamaraikannan, R.; Shaw, M. T.; Holmes, J. D.; Morris M. A.; *J Colloid Interface Sci.* **2013**, 393, 192.

[**29**] A Andreozzi, *et. al.; Nanotechnology,* **2011**, 22, 185304.

[30] Borah, D.; Rasappa, S.; Senthamaraikannan, R.; Holmes, J. D.; Morris, M. A.; *Adv. Mater. Interfaces,* **2004**, 1300102.

[31] 2009 International Technology Roadmap for Semiconductors (ITRS), **2009**, Edition Lithography ITRS.

[**32**] Liu, C.; Ramírez-Hernández, A.; Han, E.; Craig, G. S.W.; Tada, Y.; Yoshida, H.; Kang, H.; Ji, S.; Gopalan, P.; Pablo, J. D.; and Nealey, P. F.; *Macromolecules*, **2013**, 46 ,1415.

[**33**] Castenmiller, T., *et. al.; Proc. SPIE 7640*, **2010**, 76401N.

[**34**] Ghoshal, T.; Senthamaraikannan, R.; Shaw, M. T.; Holmes, J. D.; and Morris, M. A.; *Nanoscale*, **2012**, 4, 7743.

[**35**] Ghoshal, T.; Senthamaraikannan, R.; Shaw, M. T.; Holmes, J. D.; and Morris, M. A.; *Approach. Adv. Mater.*, **2014**, 26, 1207.

[36] Jansen, H.; Gardeniers, H.; De Boor, M.; Elwenspoek, M.; and Fluitman, J.; *J. Micromech. Microeng.* **1996,** 6, 14.

[37] Tzeng, Y.; Lin, T. H.; and Waddell, J.; *J. Electrochem. Soc*. **1990**, 137, 2612.

[38] Winters, H. F.; and Coburn, J. W.; *Surf. Sci. Rep., **1992***, 14, 161.

[39] Oehrlein, G. S.; (Park Ridge, NJ: William Andrew Publishing), **1990**, p196.

[40] Legtenberg, R.; Jansen, H.; De Boer, M.; and Elwenspoek, M.; *J. Electrochem. Soc.***1995**, 142, 2020.

[41] Aachboun, S.; Ranson, P.; Hilbert, C.; and Boufnichel, M.; *J. Vac.Sci. Technol.* A, **2000**, 18, 1848.

[42] Kenoyer, L.; Oxford, R.; and Moll, A.; *Proc. 15th Biennial University/Government/Industry Microelectronics Symp. (Boise, ID),* **2003**, 338.

[43] Yeom, J.; Wu, Y.; and Shannon, M. A.; *The 12th Int. Conf. on Solid State Sensors, Actuators and Microsystems (Boston, MA),* **2003**, 1631.

[44] Lai, S. L.; Johnson, D.; and Westerman, R.; *J. Vac. Sci. Technol.* A, **2006**, 24, 1283.

[45] McAuley, S. A.; Ashraf, H.; Atabo, L.; Chambers, A.; Hall, S.; Hopkins. J.; and Nicholls, G.; *J. Phys. D: Appl. Phys.*, **2001**, 34, 2769.

[46] Dennis, J. O.; Ahmad, F.; and Khir, H.; *CMOS compatible bulk micromachining*, **2013,** 121.

2.1. Abstract

Block copolymer (BCP) microphase separation at substrate surfaces might enable the generation of substrate features in a scalable, bottom-up fashion provided that the pattern structure, orientation and alignment can be strictly controlled. The PS-*b*-PDMS (polystyrene-*block*-polydimethylsiloxane) system is attractive as it can form small features and the two blocks can be readily differentiated during pattern transfer. However, PS-*b*-PDMS offers a considerable challenge because of the chemical differences in the blocks which leads to poor surface-wetting, poor pattern orientation control and structural instabilities. These challenges are considerably greater when line patterns have to be created and this is the focus of the current work. This chapter deals with the controlled pattern formation in cylinder forming PS-*b*-PDMS by anchoring different types of hydroxyl-terminated homopolymer and random copolymer brushes on planar and topographically patterned silicon substrates for the fabrication of nanoscale templates. It is demonstrated that non-PDMS-OH containing brushes may be used which offers advantage for substrate feature formation. To demonstrate the *3-D* film structure and show the potential of this system towards device-like structure generation, the PDMS patterns were transferred to underlying substrate to fabricate nanoscale features with a feature size of ~ 14 nm.

2.2. Introduction

The development of micro- and nano- technology depends on the ability to fabricate micro and nanosized structures with high precision. Top-down lithographic techniques include UV **[1]**, thermal **[2]**, e-beam **[3, 4]**, X-ray **[5]** methods and the manufacturing, state-of-the-art, pitch size is now approaching around 16 nm. In parallel to the physical engineering of substrate features, the bottom-up approach based on hierarchical self-assembly of structures ranging from molecular building blocks through to nanoparticulates and macromolecular structures is the subject of intense research **[6]**. There are advantages and drawbacks in both approaches. In top-down methodologies further downsizing is critically related to light wavelengths, light-material interactions and also thermal management **[1, 7, 8]**. On the other hand,

it is highly challenging to achieve long-range translational order and sufficient pattern robustness of systems fabricated with bottom-up approaches **[9-11]**.

Directed self-assembly (DSA) based on graphoepitaxy is a technique that exploits the complementarity of the two approaches **[12-15]**. The confinement of BCP structures within narrow, topographical features can guide BCP patterns into alignment and was first reported by Li *et al.* for polystyrene-*block*-polymethylmetacrylate (PS-*b*-PMMA) **[16]**. Many authors have subsequently studied this system since it is compatible with established resist technologies **[17, 18]**. However, PS-*b*-PMMA has a relatively low Flory-Huggins parameter (χ) and results in minimum feature size dimensions that are well above that of the established UV-lithography method. Other polymers can exhibit lower minimum feature size and polystyrene-*block*-polydimethylsiloxane (PS-*b*-PDMS) is attracting much research effort. This is because its' Flory-Huggins parameter ($\chi = 68/T - 0.037$) is relatively high allowing sub - 10 nm feature size scaling **[19]** as demonstrated for line forming non-symmetric PS-*b*-PDMS using a nanoimprint lithography (NIL)-assisted DSA approach **[20]**. A further attractive feature of this system is its' chemistry and composition that allows it to be relatively easily processed into an on-chip etch mask that can be used for pattern transfer by selective etch methods **[21, 22]**.

However, in the PS-*b*-PDMS system two major issues arise: strong surface dewetting due to its' high hydrophobicity and difficulties in controlling feature orientation, particularly for definition of parallel versus vertical cylinder alignment. To overcome these limitations, a surface pre-treatment with a PDMS-OH brush is usually required **[21, 22]**. However, it should be noted that the use of a PDMS-OH brush may present further problems for pattern transfer into the substrate. Briefly, the PDMS-OH brush layer produces (on its own or with the BCP) a PDMS layer at the substrate-polymer interface and this will increase the thickness of the surface passive silica layer and minimize the effectiveness of any selective $Si:SiO_2$ dioxide etch chemistry used for pattern transfer **[23]**. However, to tune the surface chemistry of the substrate to improve wetting characteristics of the BCP as well as conferring orientational control of the pattern, reports of the use of other hydroxyl-terminated homopolymer and copolymer brushes as an alternative to PDMS-OH brush is scant **[22]**. In order to address the deficit in alternative non-PDMS-OH containing brush

chemistry, hydroxyl-terminated homopolymer and copolymer brushes with different characteristics were investigated at both planar and topographically patterned substrates.

2.3. Materials and methods

2.3.1. Materials

The planar substrates used were polished, test grade 8" silicon <100> wafers (*p*- type, B doped, thickness 650 μm, and resistivity 6-14 Ω.cm) with a native oxide layer of ~ 2 nm. No attempt was taken to remove the native oxide. The

Table 2.1. Details of polymer characteristics used in the present study

molecular weight, (M_n), g/mol	polydispersity index, M_w/M_n	mole fraction of PS, %	volume fraction of PDMS, ϕ_{PDMS}	description
10,000	1.05	-	-	hydroxy-terminated PS
9,500	1.10	-	-	hydroxy-terminated PMMA
12,400	1.25	0.58	-	hydroxy-terminated PS-*r*-PMMA
5,000	1.07	-	-	hydroxy-terminated PDMS
45,500	1.15	0.60	0.34	cylindrical PS-*b*-PDMS

topographically patterned substrates (fabricated *via* 193 nm UV lithography) were etched silicon <100> wafers with an insulating SiO_2 layer of 150 nm. The channel width and depth were 280 nm and 60 nm, respectively. Hydroxyl-terminated polystyrene (PS), polymethylmethacrylate (PMMA), polydimethylsiloxane (PDMS), a random copolymer composed of styrene (S) and methyl methacrylate (MMA) (PS-*r*-PMMA) and an asymmetric, cylinder-forming PS-*b*-PDMS diblock copolymer were all purchased from Polymer Source, Inc., Canada, and used as received. Detailed descriptions of the polymers are summarized in **Table 2.1**. Toluene (99.8%, anhydrous), sulfuric acid (98%) and hydrogen peroxide (30%) were purchased from

Sigma-Aldrich and used without further purification unless otherwise stated. De-ionized water was used wherever necessary.

2.3.2. Polymer brush attachment

Substrates (planar and channel cut) were cleaned in a piranha solution (*1:3* v/v 30% H_2O_2:H_2SO_4) at 363 K for 60 min, rinsed with deionized water (resistivity ≥ 18 MΩ cm^{-1}) several times and were dried under N_2. The piranha activation removes any organic contaminant and creates a high density of hydroxyl groups on the silicon substrates. Polymer brush solutions (1.0 wt % in toluene) were used and mixed brush solutions (50:50 volume mixtures) were prepared by addition. The brush solutions were spin-coated onto the substrates at 3000 rpm for 30 s. Samples were annealed in a vacuum oven (Townson and Mercer EV018) at 443 K under vacuum for 6 h. This procedure provides chemically anchored brushes by condensation reactions between silanol groups at the substrate surface and on the brush. Unbound polymers were removed by sonication (Cole-Palmer 8891 sonicator) and rinsing in toluene.

2.3.3. Preparation of BCP thin films

Thin films of PS-*b*-PDMS were prepared by spin coating (3200 rpm and 30 s) a 1.0 wt % toluene solution of the BCP onto the brush layer. As-cast films were solvent annealed in glass jars under a saturated toluene environment at room temperature (~288 K) for 30 min or 3 h. Samples were removed from the glass jars after the desired anneal time and allowed to evaporate the trapped solvent at ambient conditions.

2.3.4. Etch processes and pattern transfer to silicon

Following BCP film formation, atomic force microscopy cannot readily show the microphase separated structure because of the presence of a surface wetting layer of PDMS which must be removed to reveal the BCP arrangement **[21, 22]**. Thus, an etch process (ETCH1) was developed to reveal the PS-*b*-PDMS pattern. This etch was one component of a multi-step process that allowed pattern transfer to the substrate. Solvent annealed PS-*b*-PDMS films were first treated with a CF_4 (15 sccm) plasma for 5 s to remove any surface PDMS layer. This was followed by an O_2 (30 sccm) plasma for 10 s with an inductively coupled plasma (ICP) and reactive ion etching (RIE) powers of 1200 W and 30 W, respectively, at 2.0 Pa with a helium backside cooling pressure of 666.6 Pa. These steps follow a similar methodology

developed by Ross *et al* **[22]**. The process removes the PS component and forms an oxidized form of PDMS on the substrate. The oxidized PDMS cylinders were then used as an etch mask for pattern transfer (i.e. ETCH2). This second processing methodology involves a CHF_3 (80 sccm) and Ar (30 sccm) plasma etch for 5 s with an ICP and RIE powers of 400 W and 30 W, respectively, at 1.6 Pa to remove any residual PDMS wetting layer at the substrate surface. This milder etch treatment is critical and needed careful optimisation. It is used to remove passive silica and any PDMS components at the silicon substrate surface without removing the 'etch mask'

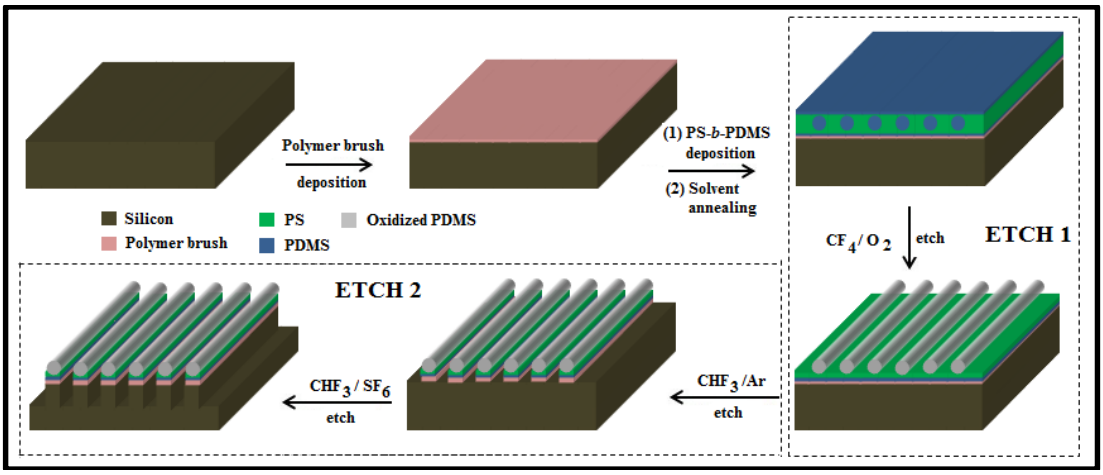

Scheme 2.1. Schematic of the process flow depicting PS-*b*-PDMS self-assembly on silicon substrate pre-coated with PDMS-OH homopolymer brush and subsequent plasma etching to remove PDMS wetting layer, PS matrix and pattern transfer to underlying silicon. See text for details.

formed by the oxidised PDMS cylinders. This process was followed by a selective silicon etch using CHF_3 (80 sccm) and SF_6 (15 sccm) gases for 15 s with an ICP and RIE powers of 1200 W and 30 W, respectively, at 2.0 Pa with a helium backside cooling pressure of 1333.2 Pa to transfer the patterns into the underlying substrate. The etching processes were accomplished in an OIPT Plasmalab System100 ICP180 etch tool.

The detailed self-assembly steps starting with PDMS-OH brush grafting, resultant structure formation and sequential etching steps are schematically shown in **Scheme 2.1**. Microphase separation of PS-*b*-PDMS results in a morphology where

the PDMS cylinders in a PS matrix are buried underneath a wetting PDMS layer **[21, 22]**.

2.3.5. Characterization of brush and BCP films

2.3.5.1. Contact angle measurements

Advancing contact angles (θ_a) of deionized water on the substrates were measured using a Data Physics Contact Angle (model: OCA15) goniometer. Contact angles were measured on the opposite edges of at least three drops and averaged. The values were reproducible to within 1.5^o.

2.3.5.2. Film thickness measurements

BCP thin film thicknesses were determined by ellipsometry (Plasmos SD2000 Ellipsometer). An average of three readings collected from different locations on a sample surface was used as the film thickness result.

2.3.5.3. Fourier Transform Infra-Red (FTIR) measurements

An IR 610, Varian infrared spectrometer was used to record the FTIR spectra in transmission mode. The measurements were performed in the spectral range of 400-500 cm^{-1}, with a resolution of 4 cm^{-1} and data were averaged over 32 scans.

2.3.5.4. Scanning Electron Microscopy (SEM)

Top-down and cross-sectional scanning electron microscope (SEM) images of etched samples were obtained by a high resolution (< 1 nm) Field Emission Zeiss Ultra Plus-Scanning Electron Microscope with a Gemini® column operating at an accelerating voltage of 5 kV.

2.3.5.5. Focused Ion Beam (FIB)

An FEI Strata 235-Focused Ion Beam (FIB) tool was used to generate FIB lamellae cross-sections. E-beam produced platinum was deposited at the substrate followed by the ion-beam deposited platinum. Milling and polishing of the samples were carried out at the lower aperture size and the specimen was imaged under the higher resolution Zeiss Ultra Plus-SEM.

2.4. Results and discussion

2.4.1. Self-assembly of PS-b-PDMS on PDMS-OH brush

The PDMS-OH brush (thickness ~4.3 nm as measured by ellipsometry) ensures that the self-assembly in the PS-*b*-PDMS film results in wetting PDMS

layers at the surface and substrate interface due to favourable PDMS-PDMS interactions and surface energies **[22]**. The formation of this sandwich structure will strongly promote the formation of a microphase separated pattern where the cylinders are orientated parallel to the surface plane since any vertical orientation will lead to increases in surface energy. **Figure 2.1(a)** shows oxidised PDMS cylinders (as revealed by ETCH1) obtained from the microphase separated PS-*b*-PDMS films deposited on the PDMS-OH brush. The cross-section SEM image presented in **Figure 2.1(b)** for a single monolayer of PDMS cylinders clearly demonstrates the efficacy of the etch chemistry to reveal the cylindrical patterns.

It is evident from the data in **Figure 2.1** that well-ordered phase separation is seen over macroscopic distances. The mean PDMS cylinder spacing, L_0, and line width, <d>, were found to be 33.4 nm and 16.2 nm, respectively. It can be seen from the cross-section image that the oxidized PDMS domains have become rounded during the ETCH1 process. This may reflect the original PDMS cylindrical structure rather than being due to an etch process. The oxidation of the PDMS cylinders during this pre-etch step is confirmed by FTIR with the detection of a Si-O-Si signal at 1098 cm^{-1} **[24]** as displayed in **Figure 2.1(c)**. Dewetting is a major issue with PS-*b*-PDMS system leading to multilayer pattern formation in some locations on the substrate. Indeed, even with the use of the PDMS-OH brush, a poor coverage of ~60 % of the overall substrate area is observed (**Figure 2.1(d)**). The oval/round shaped areas (islands) in **Figure 2.1(d)** are dewetted regions of BCPs that have a dome-like structure as shown by AFM topography (not shown for convenience). This dewetting is not due to an incoherent brush layer (**Figure 2.1(e)**) as the brush appears to be very homogeneous without any obvious signs of island formation/defect sites. The consequences of dewetting causing multilayer formation can be observed in **Figure 2.1(f)**. Multilayers of PDMS cylinders can be seen in the cross-section SEM image. It is evident that the upper PDMS cylinders are well-ordered from the top-down images but the structure and order within lower layers requires cross-sectional images to reveal the packing arrangement. The high resolution FIB cross-section SEM image in **Figure 2.1(g) and 2.1(f)** provides such data. These data clearly show the multilayer stacking of cylinders and suggest that order is seen in both the in-plane and out-of-plane cylinder arrangement. The images further reveal the presence

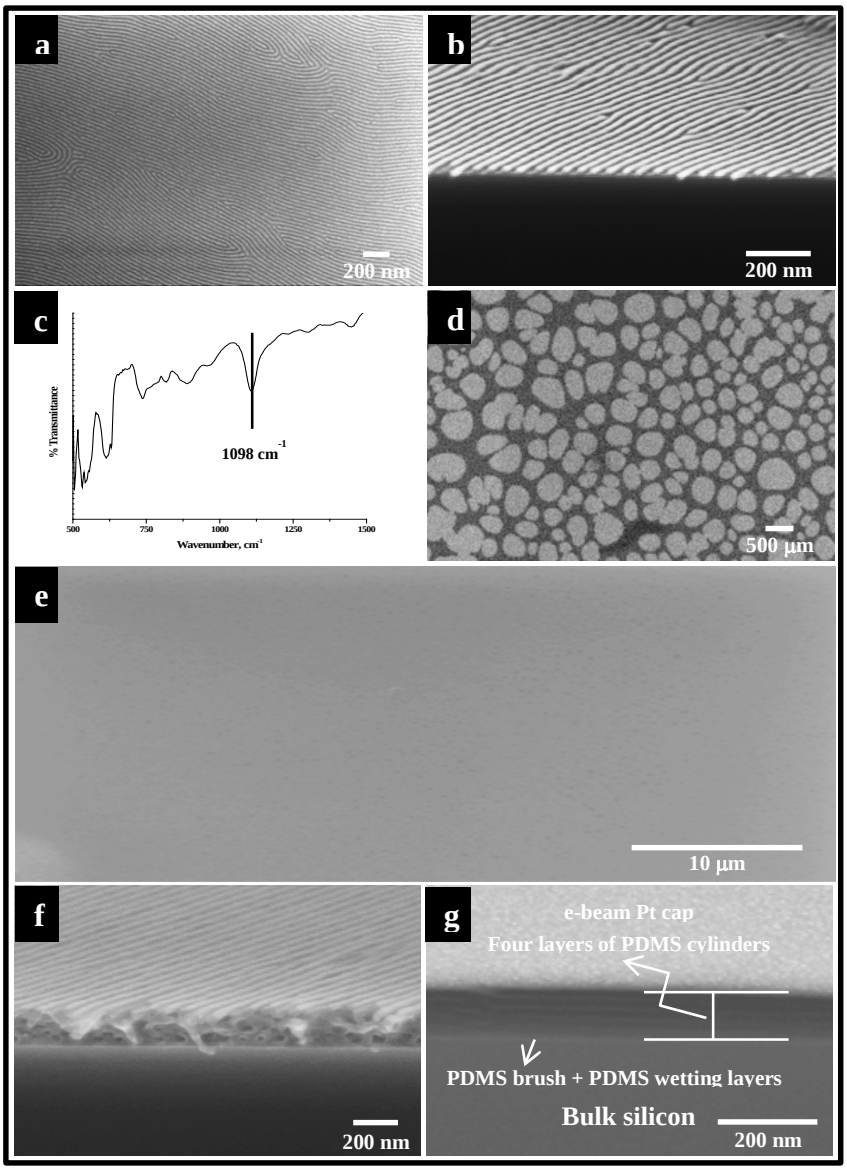

Figure 2.1. (a) Top-down SEM images of the PS-*b*-PDMS pattern (as revealed by ETCH1) formed using a 3 h solvent anneal on PDMS-OH brush modified silicon substrates. **(b)** A cross-section SEM image showing monolayer of PDMS cylinders. **(c)** An FTIR spectrum of the oxidized PDMS cylinders formed from the PS-b-PDMS using ETCH1. **(d)** An SEM image of microphase separated PS-*b*-PDMS film showing the poor wetting and low film coverage. **(e)** An SEM image of PDMS-OH brush anchored silicon substrate. **(f)** A cross-section SEM image and **(g)** FIB cross-section SEM image of etched PS-*b*-PDMS films showing multiple layers of PDMS cylinders.

of the expected wetting PDMS layer is unaffected by the CF_4 and O_2 etches. The wetting layer is significantly thicker (~8 nm) compared to the thickness of the

PDMS-OH brush layer (~ 4 nm) and strongly suggests that a strong PDMS-OH (brush) - PDMS (BCP) interaction exists and is the cause of the relatively thick wetting layer at this interface.

2.4.2. Surface characteristics of different polymer brushes

As briefly detailed above, exploration of alternative (to PDMS-OH based brushes) brush chemistry is scantly reported although Ross *et al.* studied the effect of

Table 2.2. Water contact angle and film thickness data of polymer brush and diblock copolymer films on silicon substrates

surface finish	contact angle (+/- 1.5º)	film thickness (nm)	film thickness brush and BCP (nm)
SiO_2/Si (as received)	44.7	-	-
SiO_2/Si (piranha)	29.5	-	27.3
PS-OH	97.9	7.3	33.6
PMMA-OH	78.6	4.5	30.8
HO-PS-*r*-PMMA	83.2	5.8	32.4
PDMS-OH	112.6	4.3	31.6
PS-OH + PMMA-OH	100.8	6.5	32.8
PS-OH + HO-PS-*r*-PMMA	99.2	6.3	33.1
PMMA-OH + HO-PS-*r*-PMMA	79.2	4.3	30.5
PS-OH + PMMA-OH + HO-PS-*r*-PMMA	100.0	5.9	32.6

a PS-OH brush on PS-*b*-PDMS self-assembly on planar and topographically patterned substrates **[22]**. A key advantage of these alternative brushes is the

reduction in the thickness of the PDMS layer that could form at the substrate interface. Here, this work is extended towards PS-OH, PMMA-OH, HO-PS-*r*-PMMA brushes and combinations thereof. Firstly, the influence of the brush type on the water contact angle of the brush layer on planar silicon substrates is summarized in **Table 2.2**. The static water contact angle of as-received silicon substrate is found to be ~45^{o} which is reduced significantly to 30^{o} on piranha treatment. This is consistent with the piranha activation creating silanol-OH groups making the surface more hydrophilic with a lower contact angle. All the brushes increase the contact angle of the surface from that of the piranha treated surfaces by significant amounts. As might be expected, from known solvent parameters etc. **[25]**, the PDMS-OH brush has the highest contact angle (most hydrophobic) and the PMMA-OH brush the lowest and the others between those values. The HO-PS-*r*-PMMA brush has an average value of the individual PS-OH and PMMA-OH brushes whilst the HO-PS-*r*-PMMA and PMMA-OH brush mixture has a value between the values of the individual components. However, the mixed brush systems containing the PS-OH brush all give contact angles around 100° which are around that of the PS-OH alone. This might be explained because the PS-OH brush film thickness is significantly greater than that of the other brushes (**Table 2.2**) and suggests that the chemistry of the surface is dominated by the thicker PS component.

FTIR measurements can provide evidence about the presence of the polymer brushes and qualitative information about relative concentrations based on the intensity of the peaks. Typical FTIR data of the polymer brushes on silicon substrates are shown in **Figure 2.2** and bands that can be associated with both the polymer films and the substrate (marked in **Figure 2.2**) can be observed. The FTIR spectrum of the PDMS-OH brush anchored silicon substrate (**Figure 2.2(a)**) show a well-resolved Si-O-Si vibration band near 1098 cm^{-1} indicative of silica materials **[24]**. The high intensity of the vibration band is due to high silicon content of the polymer brush which is ~36% based on its molecular weight. However, there may be a minor contribution from the native oxide layer of the silicon substrate as seen below. The FTIR spectrum of the brush layer also shows a medium strength OH valence vibration band near 2630 cm^{-1}. The presence of the OH band is probably due to hydroxylation and attached water through hydrogen bonding. The peaks observed

at 1395, 2825 and 2883 cm^{-1} can be assigned to CH_3, CH_2 and CH stretching vibrations **[25]**, respectively.

FTIR spectra of the other polymer brushes are presented in **Figure 2.2** and also reveal the presence of a Si-O-Si vibration band near 1098 cm^{-1} indicative of silica materials. Since these polymers are non-Si containing, it is clear that these features arise from the underlying SiO_2 at the silicon substrate. Note, however, that intensity

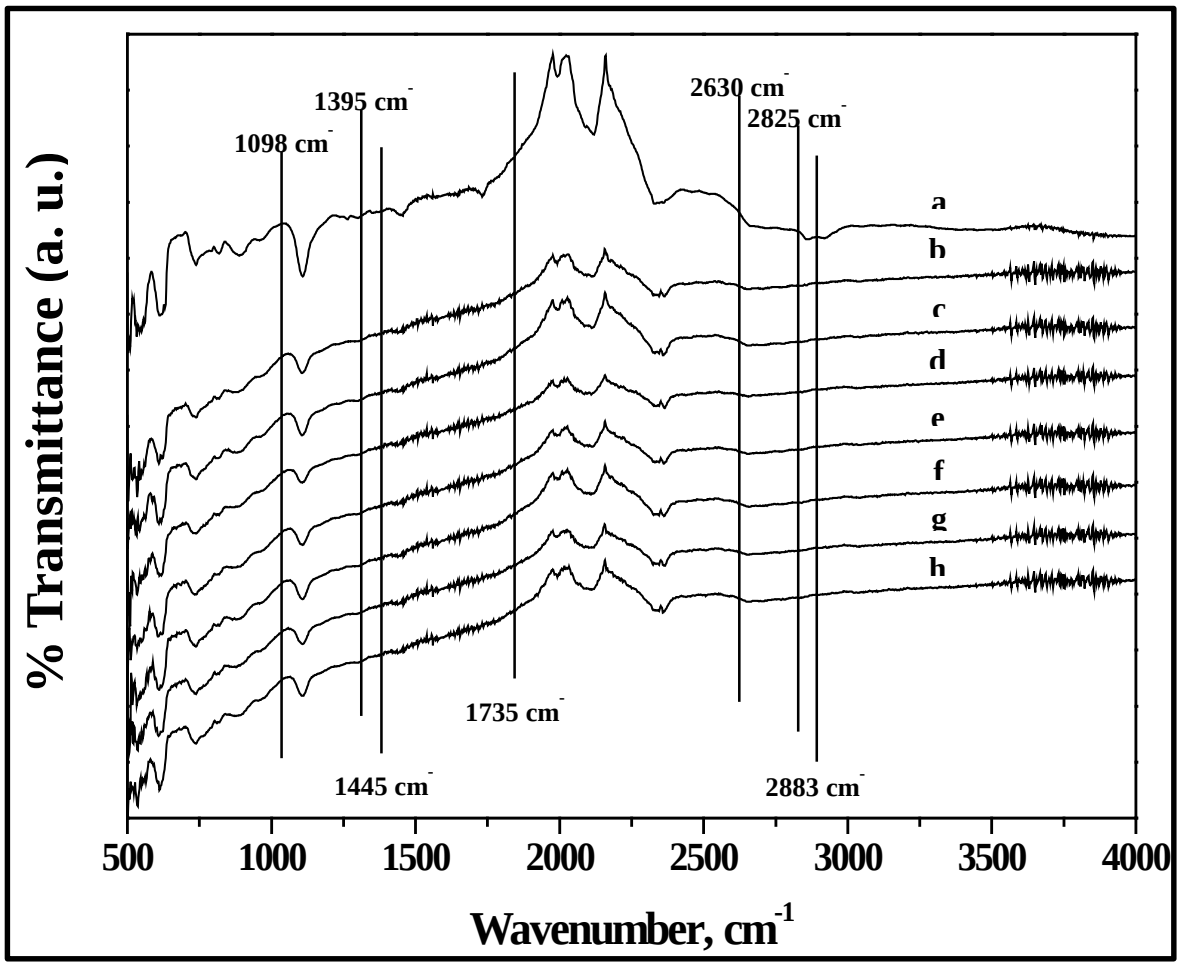

Figure 2.2. FTIR spectra of **(a)** PDMS-OH, **(b)** HO-PS-*r*-PMMA, **(c)** PS-OH, **(d)** PMMA-OH, **(e)** PS-OH + PMMA-OH, **(f)** HO-PS-*r*-PMMA + PS-OH, **(g)** HO-PS-*r*-PMMA + PMMA-OH and **(h)** HO-PS-*r*-PMMA + PS-OH + PMMA-OH polymer brushes anchored planar silicon substrates after cleaning.

of this band is much weaker than in the data of the PDMS-OH brush and suggests that the contribution of silicon oxide type species following ETCH1 are much more significant compared to that of SiO_2 from the substrate. Other vibrational bands from the polymer brushes are difficult to observe but bands associated with CH_3, CH_2

and CH stretching vibrations can be identified at 1395, 2825 and 2883 cm^{-1}. The rather low intensity of these features is consistent with the presence of the thin brush layers (**Table 2.2**). A C-CH_3 deformation band was observed at 1445 cm^{-1} in all the spectra. The C=O stretching vibration band arising from the PMMA-OH and HO-PS-*r*-PMMA and their combinations with/without PS-OH brush could be detected at 1735 cm^{-1} **[26]**. However, the C-O-C stretch usually observed at 1105 cm^{-1} **[26]** could have merged with the Si-O-Si band. Though the presence of the polymer brushes was evidenced from the FTIR, it could not reveal the relative concentrations of the brushes and any preferential grafting in the brush combinations. XPS might provide greater quantifiable analysis of these mixed brush modified surfaces. However, in our experiments it added little because of the much larger C1s signals from aryl and aliphatic carbon signals.

The brush treated surfaces were further characterized using ellipsometery and the results are presented in **Table 2.2**. The thickness of the brush layers lies in the range of 4-7 nm and is in the range expected from simple calculations. Polystyrene and polymethylmethacrylate adopt a random coil structure and is modelled by $\langle h^2 \rangle_0 = M_w * 0.43$ and $\langle h^2 \rangle_0 = M_w * 0.42$, respectively, where $\langle h^2 \rangle_0$ is the mean-square end-to-end distance of the polymer coil and M_w is the molecular weight **[27]**. The random coil size estimated for PS-OH and PMMA-OH are 6.6 nm and 6.3 nm, respectively, compared to measured sizes of 7.3 and 4.5 nm. The coil size calculated for HO-PS-*r*-PMMA considering $\langle h^2 \rangle_0 = M_w * 0.425$ and found to be 7.3 nm (experimental value = 5.8 nm). Assuming $\langle h^2 \rangle_0 = M_w * 0.425$ for PDMS-OH, the value estimated is 4.6 nm and measured at 4.3 nm. These data are in reasonable agreement with the measured brush layer thickness since some surface strain/relaxation in the thin film is expected. This would suggest that a complete monolayer of polymer molecules is formed from the brush procedure used here and provides an excellent surface for BCP deposition. The PS-OH brush shows significantly greater thickness than that estimated by ellipsometry suggesting distortions in the random coil structure. The thickness values for the mixed brushes seem to have values between those of the two components and are consistent with attachment of both polymers rather than preferential adsorption and reaction of one component.

2.4.3. Effect of polymer brushes on PS-b-PDMS self-assembly

Microscopic examination of BCP films on the brush modified surfaces suggest that exposure to the solvent anneal process for longer periods can lead to significant dewetting **[28]**, and coverages on, e.g. the PDMS-OH brush drop from around 90% (30 min) to about 60% (3 h). In this way, any structures are best viewed as metastable. Thus, in this work, shorter (30 min) and longer (3 h) anneal times were investigated to understand their effect on microphase separation. Generally, the non-PDMS based brushes showed coverages of greater than 80-90% even after the longer

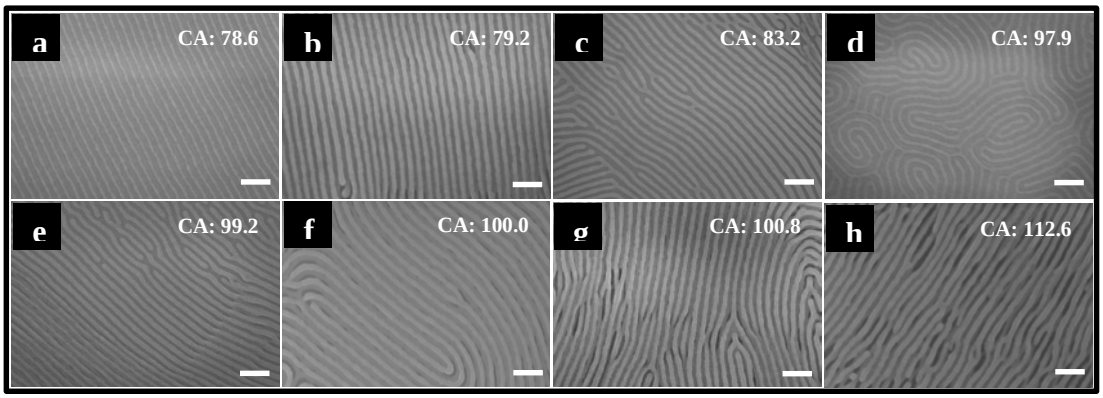

Figure 2.3. Top-down SEM images (image scale bar: 100 nm) of microphase separated PS-*b*-PDMS films as revealed by ETCH1 on the following modified substrates, **(a)** PMMA-OH, **(b)** HO-PS-*r*-PMMA + PMMA-OH, **(c)** HO-PS-*r*-PMMA, **(d)** PS-OH, **(e)** HO-PS-*r*-PMMA + PS-OH, **(f**) HO-PS-*r*-PMMA + PS-OH + PMMA-OH, **(g)** PS-OH + PMMA-OH and **(h)** PDMS-OH brush coated silicon substrates. Data were recorded after a 30 min solvent anneal.

anneal time and this is a key advantage of their use. The effect of anneal time was combined with the effect of surface treatment by different polymer brushes and the results are presented in **Figure 2.3** and **Figure 2.4** for 30 min and 3 h, respectively. SEM images were taken at different locations on the substrate and show that the orientation is homogeneous over the entire surface. Representative images are shown in the figures. On first examination the data from the 30 min and 3 h solvent anneal times are essentially similar with well-ordered films formed of parallel cylinder orientation. However, if these are examined closely, it can be seen that some images consist of multi-layer features as described above. This can be seen in **Figure 2.3(f) to 2.3(h)** where dark areas can be seen due to stacked cylinders exposed by the etch treatment. As discussed earlier, these multi-layer regions exist because of dewetting

and formation of island structures. It is apparent that this dewetting behaviour is more likely at the surfaces of higher contact angle (i.e. more hydrophobic). For longer solvent anneal periods, dewetting is generally increased and in several cases multilayer formation is visible at lower contact angles, 78.6°, 79.2° and 83.3°. However, surfaces displaying contact angles of 97.9° and 99.2° were resistant to dewetting (PS-OH and PS-OH + HO-PS-*r*-PMMA brushes). It is suggested that these surfaces have optimal properties for interaction with the PS-*b*-PDMS BCP.

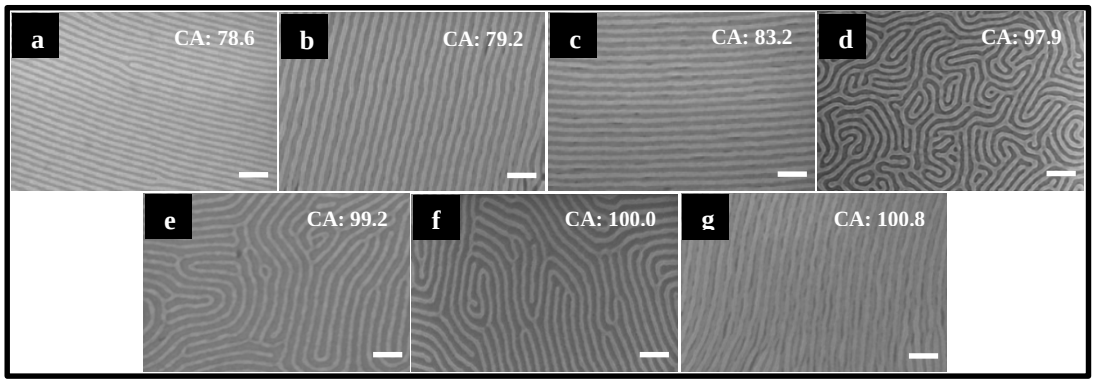

Figure 2.4. Top-down SEM images (image scale bar: 100 nm) of microphase separated PS-*b*-PDMS films as revealed by ETCH1 on **(a)** PMMA-OH, **(b)** HO-PS-*r*-PMMA + PMMA-OH, **(c)** HO-PS-*r*-PMMA, **(d)** PS-OH, **(e)** HO-PS-*r*-PMMA + PS-OH, **(f)** HO-PS-*r*-PMMA + PS-OH + PMMA-OH and **(g)** PS-OH + PMMA-OH brush coated silicon substrates. Data were recorded after a 3 h solvent anneal.

2.4.4. Directed self-assembly by hard graphoepitaxy

As discussed earlier, surface treatment with polymer brushes facilitates self-assembly, short-range domain ordering, defect minimization, and improves the wetting property of the BCP. However, to achieve long-range pattern ordering, this surface treatment can be combined with the graphoepitaxy technique to direct self-assembly in PS-*b*-PDMS and has been demonstrated in several articles **[22, 29, 30]**. These topographically patterned surfaces are also extremely useful in understanding the changes in surface chemistry that has been varied by use of the various polymer brushes. This is because top-down imaging can be used to determine preferred block orientation at the sidewall. As above, the patterned substrates were pre-coated with different hydroxyl-terminated polymer brushes and their mixtures in different combinations prior to BCP deposition. **Figures 2.5 and 2.6** show the results of the PS-*b*-PDMS pattern after ETCH1 following a short (30 min) and long (3 h) solvent

anneal. It can be seen from **Figure 2.5 and 2.6** that the brushes are all generally compatible with graphoepitaxial alignment of the PS-*b*-PDMS. Generally, for the hexagonal structure, preferred alignment should be achieved when the sidewalls preferentially interact with the majority block compared to the minor component. If the sidewalls are neutral and interact equally with both blocks (thus favouring the presence of both

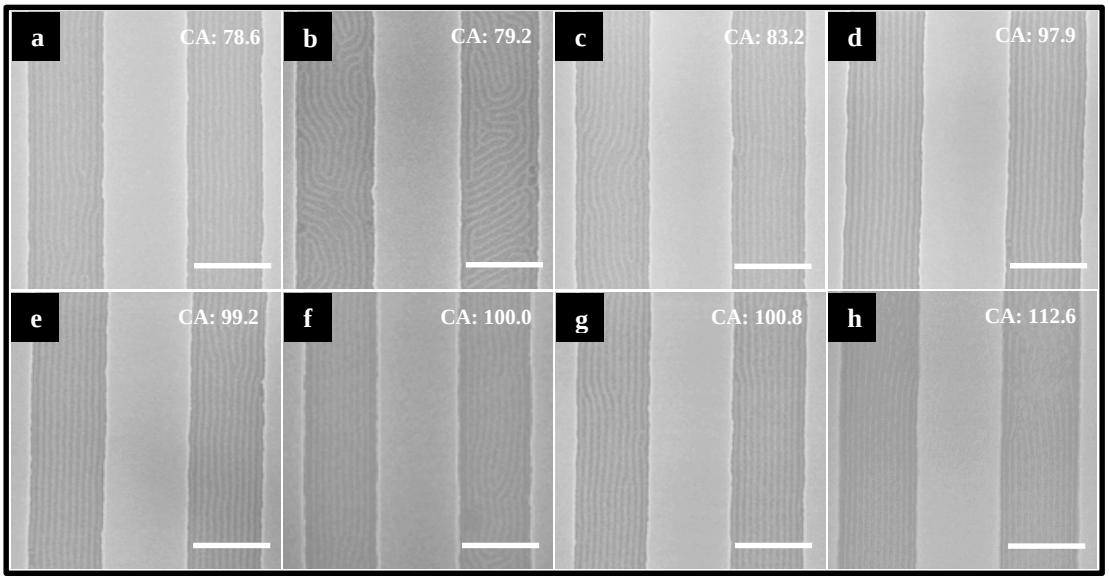

Figure 2.5. Top-down SEM images (image scale bar: 300 nm) of microphase separated PS-*b*-PDMS films as revealed by ETCH1 on **(a)** PMMA-OH, **(b)** HO-PS-*r*-PMMA + PMMA-OH, **(c)** HO-PS-*r*-PMMA, **(d)** PS-OH, **(e)** HO-PS-*r*-PMMA + PS-OH, **(f**) HO-PS-*r*-PMMA + PS-OH + PMMA-OH, **(g)** PS-OH + PMMA-OH and **(h)** PDMS-OH brush coated patterned substrates. The solvent anneal time was 30 min.

hexagonal structure preferred alignment should be achieved when the sidewalls preferentially interact with the majority block compared to the minor component. If the sidewalls are neutral and interact equally with both blocks (thus favouring the blocks at the sidewall), a non-aligned structure is formed. For the samples solvent annealed for 30 min, it is only the mixture of PMMA-OH and HO-PS-*r*-PMMA brushes that leads to poor alignment and functionality at the wall that could be described as neutral. For the 3 h solvent anneal, the quality of the alignment appears to be significantly worse for most samples and more defects can be seen in the images presented **Figure 2.6**. However, this is not easy to quantify because a majority of the defects observed arise from defects in the sidewall which cause local

variations in the channel width. However, neutral type alignment can be clearly seen in the data recorded for the PMMA-OH and the combined PMMA-OH and HO-PS-*r*-PMMA brush layers. It should also be noted that the data from the combined HO-PS-*r*-PMMA brush system also shows mixed morphology with regions of vertical and perpendicular alignment of the cylinders. This does confirm neutrality of the sidewall and suggests the PMMA-OH/HO-PS-*r*-PMMA base is neutral enough to allow some vertical alignment of the cylinders.

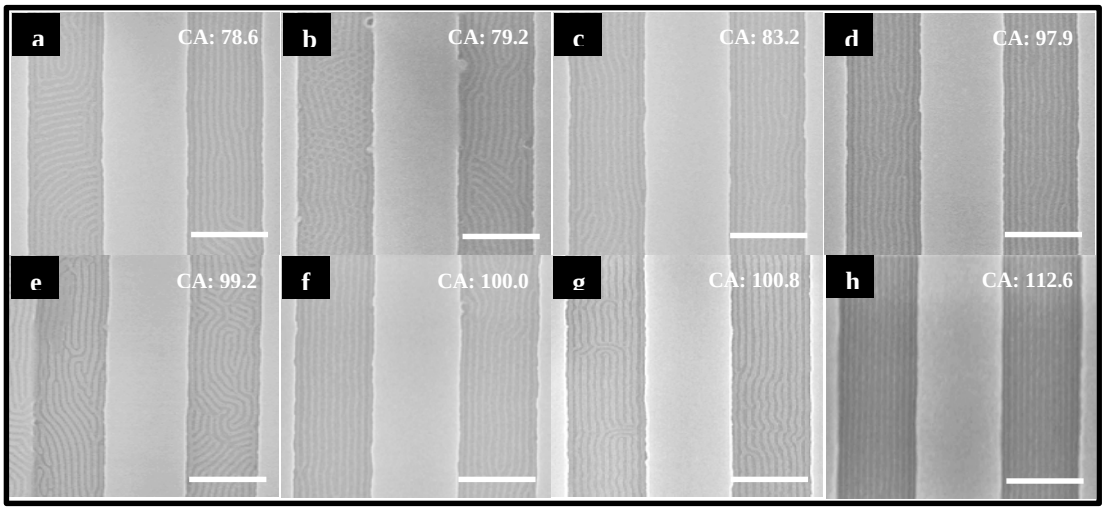

Figure 2.6. Top-down SEM images (image scale bar: 300 nm) of microphase separated PS-*b*-PDMS films as revealed by ETCH1 on **(a)** PMMA-OH, **(b)** HO-PS-*r*-PMMA + PMMA-OH, **(c)** HO-PS-*r*-PMMA, **(d)** PS-OH, **(e)** HO-PS-*r*-PMMA + PS-OH, **(f)** HO-PS-*r*-PMMA + PS-OH + PMMA-OH, **(g)** PS-OH + PMMA-OH and **(h)** PDMS-OH brush coated patterned substrates. The solvent anneal period was 3 h.

2.4.5. Pattern transfer of films into the underlying substrate

To demonstrate the usefulness of this system for application in microelectronic fabrication, the patterns obtained following ETCH1 were pattern transferred into the substrate (ETCH2). The pattern transfer of PS-*b*-PDMS BCP to the substrate is not a straight forward process unlike that for more well-established polymer systems e.g., PS-*b*-PMMA **[23, 31]**, and PS-*b*-PEO **[32]** because of the complex structure of the PS-*b*-PDMS films. It should be noted that for an effective pattern transfer process that the O_2 etch used in ETCH1 has to be carefully optimized so that the cylinder structure is not undercut. However, if this is achieved, the oxidized, silica like cylinders can act as a hard mask for pattern transfer. **Figure 2.7(a, b)** shows the top-down and cross-section SEM images of the silicon nanowires on the silicon substrate

obtained after the etches were used to remove the silica-like materials at the substrate surface and then to selectively remove silicon. The cross-section SEM image shows the nanowire line width of ~14 nm with a pattern depth of ~26 nm. The FIB cross-section SEM images shown in **Figure 2.7(c, d)** provide a more detailed image of the

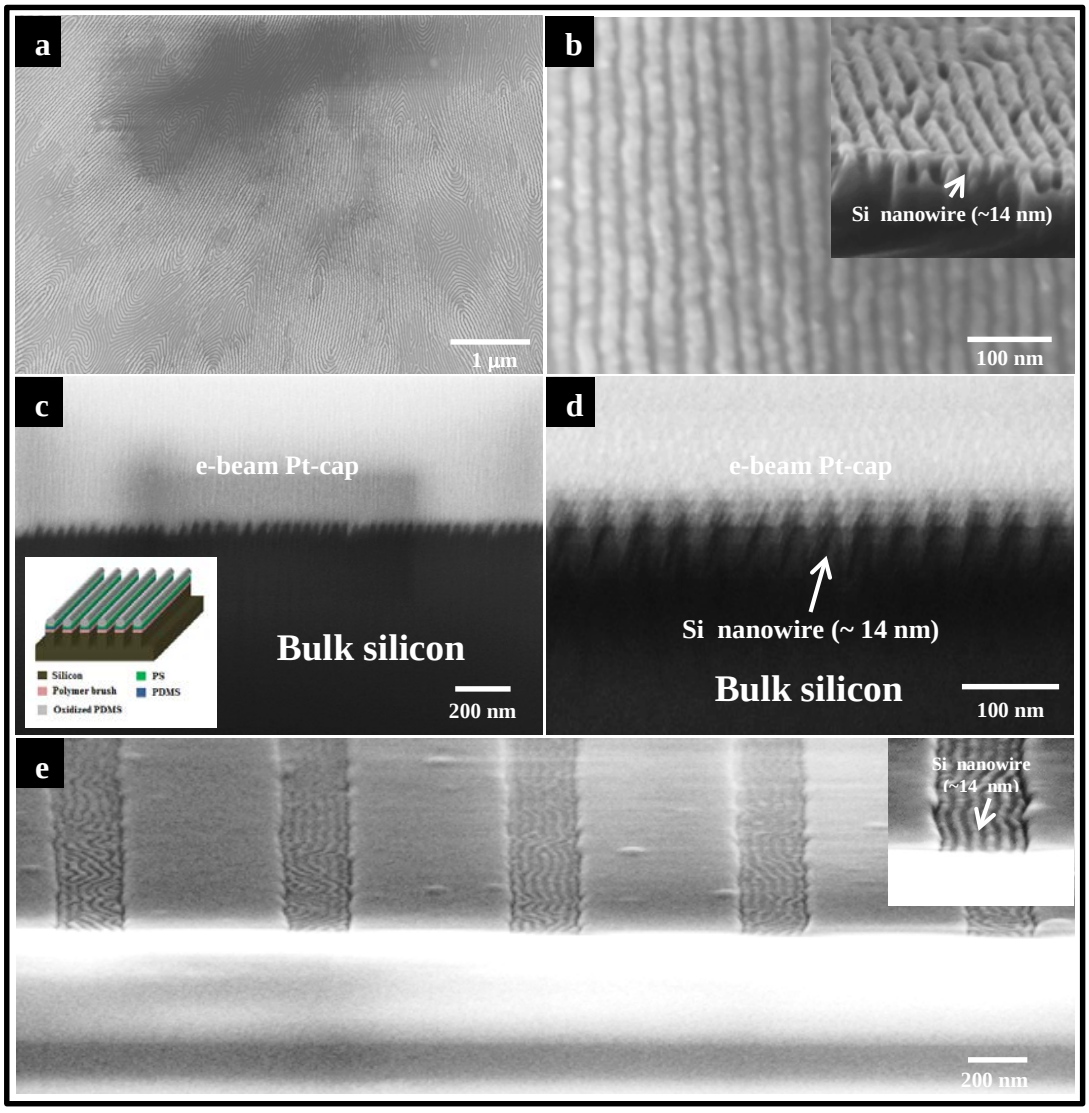

Figure 2.7. (a) Low resolution and **(b)** high resolution top-down SEM images of PDMS cylindrical patterns transferred to underlying silicon substrate. The inset of **(b)** is a corresponding cross-section SEM image. **(c)** Low resolution and **(d)** high resolution focused ion beam (FIB) - cross-section SEM images of PDMS cylindrical patterns transferred to underlying silicon substrate. The inset of **(c)** is a schematic showing oxidized PDMS cylinders on silicon nanowires. **(e)** Tilted SEM image of PDMS cylindrical patterns transferred to underlying SiO_2 on a topographically patterned substrate (the inset to **(e)** is a corresponding high resolution SEM image).

silicon nanowires fabricated in this way. The silicon features on the substrate are slightly narrower than the width of the initial oxidized PDMS cylinders due to a partly isotropic etching process. A reasonable aspect ratio of ~1.3 was obtained. The tilted and cross-section SEM images of the silicon nanowires on the topographically patterned silicon substrate are shown in **Figure 2.7(e)**. The silicon nanowires formed are aligned within the channel and appear to be reasonably smooth. The tilted SEM images (**Figure 2.7(e)** and inset image) show that the pattern transfer process is successful with a line width of ~13.6 nm and a pattern depth of ~25.3 nm - consistent with that recorded from the planar substrate.

2.5. Conclusions

The first conclusion of this work is that the choice of a suitable interfacial brush for control of BCP orientation is not facile and choices may require very careful consideration if wetting layers are to be avoided or if the brush is to be used within topographically patterned substrates for alignment control. It might be imagined that a PDMS-OH brush would be an ideal choice for this system but in terms of wetting characteristics, it is far from ideal and, indeed, island like structures are observed as solvent anneal times increase. The reason for this might lie in the surface roughness of the surfaces with this island structure. Because of the greater surface area, the surface energy will be significantly reduced because of the increased area of the low surface energy PDMS wetting layer that forms in these systems. As the surfaces are made less hydrophobic, wetting appears to improve which appears to be counter intuitive. However, this may be because they favour the PS component and prevent a PDMS interface layer forming. Multilayer formation seems, once again, to become more likely at the lowest contact angles suggesting the BCP brush layer are becoming less favourable again. It is clear that rationalising these effects on just water contact angle is not possible. Instead, the chemical interaction of a brush and the BCP as well as the structure of the film must be considered. Here, it might be suggested that regular thickness, coherent films are more likely to be formed when the brush has a majority PS component and this must be because of favourable PS-PS interactions at the brush-BCP interface. At the most hydrophilic surfaces, i.e. those based on majority PMMA-OH systems, the system

favours neither PS nor PDMS and island formation becomes probable. However, despite the complexity, the correct choice of brush can allow highly coherent films of regular thickness to be formed. Importantly, the formation of a PDMS wetting layer can be avoided with the correct choice of brush.

Whilst the brush can be chosen to control wetting phenomena on planar surfaces, it also influences the regularity of DSA structures formed in topographically patterned substrate surfaces. However, an important point to note is that optimal surface wetting may not be consistent with the greatest structural alignment. In this system, it appears that wetting is favoured by having a surface that is less favourable to PDMS but it appears from the data that the most hydrophobic surfaces lead to surface neutrality and alignment is decreased and the number of pattern defects increases.

Tuning the surface chemistry in this system is important for the possible applications described herein whereby ultra-small features can be created for device development. The presence of multilayers due to wetting cannot be tolerated because pattern transfer results in complex *3-D* structures. Further, a surface PDMS wetting layer is not favoured (but note, even with this layer pattern transfer may be achieved) because it introduces additional (silica removal) steps which compromises the function of the polymer derived structure as an on-chip etch mask and achieving high selectivity and good aspect ratio of the formed silicon features is difficult.

It, thus, seems that very fine control of surface chemistry is required to optimise a number of factors that are not necessarily compatible. The number of well optimised surface chemistries for the DSA of BCP systems is relatively few. This work demonstrates that simple contact angle comparisons are not sufficient to predict behaviour and considerable further work is needed to provide a definitive understanding of surface functionalization to control pattern formation as well as to provide methods by which the correct surface chemistry might be predicted from standard analytical methods.

2.6. References

[1] Wissen, M.; Bogdanski, N.; Moellenbeck, S.; Scheer, H. C.; *Mask and Lithography Conference (EMLC)*, Jan. **2008**, 1, 11.

[2] Chung, S.; Felts, J. R.; Wang, D.; King, W. P.; De Yoreo, J. J.; *Appl. Phys. Lett.* **2011**, 99, 193101.

[3] Grigorescu, A. E.; Hagen, C. W.; *Nanotechnology*, **2009**, 20, 292001.

[4] Namatsu, H.; Watanabe, Y.; Yamazaki, K.; Yamaguchi, T.; Nagase, M.; Ono, Y.; Fujiwara, A.; Horiguchi, S.; *J. Vac. Sci. Technol. B* **2003**, 21, 1.

[5] Hirai, Y.; Hafizovic, S.; Matsuzuka, N.; Korvink, J. G.; Tabata, O. *J. Microelectromech. S.* **2006**, 15, 159.

[6] Hamley, I. W. *Angew. Chem. Int. Edit.* **2003**, 42, 1692.

[7] Mack, C. A. *IEEE T Semiconduct M*. **2011**, 24, 202.

[8] Freebody, M. *Photon Spectra* **2011**, 45, 45.

[9] Kumar, P. *Nanoscale Res. Lett.* **2010**, 5, 1367.

[10] Ariga, K.; Hill, J. P.; Lee, M. V.; Vinu, A.; Charvet, R.; Acharya, S. *Sci. Technol. Adv. Mater.* **2008**, 9, 014109.

[11] Hawker, C. J.; Russell, T. P. *MRS Bull.* **2005**, 30, 952.

[12] Guo, L. J. *Adv. Mater.* **2007**, 19, 495.

[13] Gates, B. D.; Xu, Q.; Stewart, M.; Ryan, D.; Willson, C. G.; Whitesides, G. M. *Chem. Rev.* **2005**, 105, 1171.

[14] Mårtensson, T.; Carlberg, P.; Borgström, M.; Montelius, L.; Seifert, W.; Samuelson, L. *Nano Lett.* **2004**, 4, 699.

[15] Chou, S. Y.; Krauss, P. R.; Renstrom, P. J. *Appl. Phys. Lett.* **1995**, 67, 3114.

[16] Li, H. -W.; Huck, W. T. S. *Nano Lett.* **2004**, 4, 1633.

[17] Farrell, R. A.; Kehagias, N.; Shaw, M. T.; Reboud, V.; Zelsmann, M.; Holmes, J. D.; Sotomayor Torres, C. M.; Morris, M. A. *ACS Nano* **2011**, 5, 1073.

[18] Salaün, M.; Kehagias, N.; Salhi, B.; Baron, T.; Boussey, J.; Sotomayor Torres, C. M.; Zelsmann, M. *J. Vac. Sci. Technol. B* **2011**, 29, 06F208.

[19] Politakos, N.; Ntoukas, E.; Avgeropoulos, A.; Krikorian, V.; Pate, B. D.; Thomas, E. L.; Hill, R. M. *J. Poly. Sci. Part B Polym. Phys.* **2009**, 47, 2419.

[20] Park, S. M.; Liang, X.; Harteneck, B. D.; Pick, T. E.; Hiroshiba, N.; Wu, Y.; Helms, B. A.; Olynick, D. L. *ACS Nano* **2011**, 5, 8523.

[21] Hobbs, R. G.; Farrell, R. A.; Bolger, C. T.; Kelly, R. A.; Morris, M. A.; Petkov, N.; Holmes, J. D. *ACS Appl. Mater. Interfaces*, **2012**, 4, 4637.

[22] Jung, **Y. S.;** Ross, C. A. *Nano Lett.* **2007**, 7, 2046.

[23] Borah, D.; Shaw, M. T.; Rasappa, S.; Farrell, R. A.; O'Mahony, C. T.; Faulkner, C. M.; Bosea, M.; Gleeson, P.; Holmes, J. D.; Morris, M. A. *J. Phys. D: Appl. Phys.* **2011**, 44, 174012.

[24] Kirk, C. T. *Physical Review B.* **1998,** 38, 1255.

[25] Bernaerts, K. V.; Du Prez, F. E. *Polymer* **2005,** 46, 8469.

[26] Bodas, D. S.; Mahapatra, S. K.; Gangal, S. A. *Sensor. Actuat. A- Phys.* **2005,** 120, 582.

[27] Fetters, L. J.; Lohse, D. J.; Richter, D.; Witten, T. A.; Zirkel, A. *Macromolecules* **1994,** 27, 4639.

[28] Yang, J.; Wang, Q.; Yao, W.; Chen, F.; Fu, Q. *Appl. Surf. Sci.* **2011,** 257, 4928.

[29] Jung, Y. S.; Jung, W. C.; Tuller, H. L.; Ross, C. A. *Nano Lett.* **2008**, 8, 3776.

[30] Jeong, J. W.; Park, W. I.; Do, L. -M.; Park, J. -H.; Kim, T. -H.; Chae, G.; Jung, Y. S. *Adv. Mater.* **2012**, 24, 3526.

[31] Farrell, R. A.; Petkov, N.; Shaw, M. T.; Djara, V.; Holmes, J. D.; Morris, M. A. *Macromolecules* **2010**, 43, 8651.

[32] Ghoshal, T.; Maity, T.; Godsell, J. F.; Roy, S.; Morris, M. A. *Adv. Mater.* **2012**, 24, 2390.

3.1. Abstract

In block copolymer nanolithography, microphase separated polystyrene-*block*-polydimethylsiloxane (PS-*b*-PDMS) thin films are particularly attractive as they can form small features and the two blocks can be readily differentiated during pattern transfer. However, PS-*b*-PDMS is challenging because the chemical differences in the blocks can result in poor surface-wetting, poor pattern orientation control and structural instabilities. Usually the interfacial energies at substrate surface are engineered with the use of a hydroxyl-terminated polydimethylsiloxane (PDMS-OH) homopolymer brush. Herein, we report a facile, rapid and tuneable molecular functionalization approach using hexamethyldisilazane (HMDS). The work is applied to both planar and topographically patterned substrates and investigation of graphoepitaxial methods for directed self-assembly and long-range translational alignment of BCP domains is reported. The hexagonally arranged *in-plane* and *out-of-plane* PDMS cylinders structures formed by microphase separation were successfully used as on-chip etch masks for pattern transfer to the underlying silicon substrate. The molecular approach developed here affords significant advantages when compared to the more usual PDMS-OH brushes used.

3.2. Introduction

Block copolymer (BCP) lithography is a thin film self-assembly process based around the microphase separation of the blocks and as a technique offers promise for the fabrication of nanopatterns of sub-10 nm feature size and has the potential to integrate into existing manufacturing processes **[1]**. BCP nanolithographic methods may find industrial application for the fabrication of:- nanowire electronic devices **[2]**, magnetic storage devices **[3]**, nanoporous membranes **[4]**, etc. Excellent control over pattern dimension and structure can be achieved in BCP systems through variation of the polymer molecular weight (N), relative volume fraction (ϕ) and the segmental interaction parameter (χ) and a number of different ordered microdomain arrangements *viz.*, lamellar, cylindrical, spherical, gyroidal, etc **[5, 6]**. can all be formed.

BCPs containing inorganic components, e.g., polydimethylsiloxane (PDMS) are particularly useful because they can be processed to directly yield an oxide

nanostructure without any selective polymer inclusion or modification procedure **[7, 8]**. The polystyrene-*block*-polydimethylsiloxane (PS-*b*-PDMS) BCP system has particular relevance because of its high Flory-Huggins parameter (χ ~0.26) **[19]** which allows delivery of sub-10 nm feature size structures. However, in the PS-*b*-PDMS system two major issues arise: strong surface dewetting due to its' high hydrophobicity and difficulties in controlling feature orientation, particularly for definition of parallel versus vertical cylinder alignment. Other authors point to the presence of 'pinning' sites at the substrate surface that result in high defect densities **[20-22]**. To overcome the substrate limitations, a surface pre-treatment with a hydroxyl-terminated polydimethylsiloxane (PDMS-OH) homopolymer brush is usually required **[7, 13]**. However, it should be noted that the use of a PDMS-OH brush may present further problems for pattern transfer into the substrate. Briefly, the PDMS-OH brush layer produces (on its' own or with the BCP) a PDMS layer at the substrate-polymer interface and this will increase the thickness of the surface passive silica layer and minimize the effectiveness of any selective Si: SiO_2 dioxide etch chemistry used for pattern transfer **[23]**. However, reports of alternative methods such as molecular functionalization that might enable tuning the surface chemistry of the substrate so as to improve wetting characteristics of the BCP as well as conferring orientational control of the pattern, are scant **[7]**.

Herein, we report a simple and rapid method for hexamethyldisilazane (HMDS) surface functionalization as an alternative to the standard polymer brush system usually used for surface chemistry control for a PS-*b*-PDMS BCP. A monolayer of the HMDS would add negligible depth to the passive silica layer. The effectiveness of the approach was shown by demonstrating that PS-*b*-PDMS microphase separated structures can be used to create nanoscale patterns at both planar and topographically patterned substrates.

3.3. Materials and methods

3.3.1. Materials

The planar substrates used were highly polished single-crystal silicon <100> wafers (*p*- type) with a native oxide layer of ~2 nm. To study directed self-assembly (DSA) by graphoepitaxy, the topographically patterned substrates used were etched

silicon <100> and $\mathbf{M_n}$: number average molecular weight, $\mathbf{M_w}$: weight average molecular weight, and ϕ: volume fraction processed by means of conventional 193 nm photolithography, mask and etch techniques. The lithographic channels used had nominal widths and depths of 250/500 nm and 50 nm, respectively. A hydroxyl-terminated polydimethylsiloxane (PDMS-OH) homopolymer and a cylinder-forming

Table 3.1. Details of the polymers used

molecular weight, (M_n), g/mol	polydispersity, M_w/M_n	mole fraction of PS, %	volume fraction of PS/PDMS, $\phi_{PS/PDMS}$
5,000	1.07	-	-
45,500	1.15	0.60	0.34

polystyrene-*block*-polydimethylsiloxane (PS-*b*-PDMS) BCP (Polymer Source, Inc.) were used as received. Detailed characteristics of the polymers are summarized in **Table 3.1**. Hexamethyldisilazane (HMDS) (99.8%), toluene (99.8%, anhydrous), dehydrated absolute ethanol, acetone (99.0%, anhydrous), iso-propanol (IPA) (99.0%, anhydrous), sulphuric acid (98.0%) and hydrogen peroxide (30.0%), all Sigma-Aldrich, were used as received unless otherwise stated. De-ionized (DI) water was used wherever necessary.

3.3.2. Preparation of brush anchored substrates

Planar and patterned substrates were cut into 2.0 cm^2 pieces and then degreased by ultrasonication in acetone and IPA solutions for 5 min each, dried in flowing N_2 gas and baked for 2 min at 393 K in an ambient atmosphere to remove any residual IPA. This was followed by cleaning in a piranha solution (*1:3* v/v 30% H_2O_2 : H_2SO_4) (***may cause explosion in contact with organic material***) at 363 K for 60 min, rinsed with DI water (resistivity ≥ 18 MΩ cm^{-1}) several times, acetone, ethanol and dried under N_2 flow. Piranha treatment removes any organic contaminant and creates hydroxyl groups on the silicon substrates. A hydroxyl-terminated PDMS brush solution of 1.0 wt. % in toluene was spin-coated (P6700

Series Spin-coater, Speciality Coating Systems, Inc., USA) onto silicon wafers at 3000 rpm for 30 s. Samples were annealed in a vacuum oven (Townson & Mercer EV018) at 443 K under vacuum (*-100 kPa*) for 6 h. This allows the end-functional hydroxyl groups of the homopolymer to bond to the substrate *via* condensation reactions. Unbound polymers were removed by sonication (Cole-Palmer 8891 sonicator) and rinsing in toluene.

3.3.3. HMDS functionalization of substrate surface

The piranha treated, hydroxylated substrates were immediately exposed to the HMDS vapour at 373 K in a beaker that contained liquid HMDS in equilibrium with its vapour. The substrates to be modified were placed in a sieve at the top of the beaker and exposed to vapour for various times (0.3 - 48 h). This followed procedure reported by Tasaltin *et al.*[24] Samples were subsequently washed with ethanol and then dried under a stream of nitrogen.

3.3.4. BCP Film Preparation and Solvent Anneal

BCP thin films were deposited onto polymer brush anchored and HMDS modified planar and patterned substrates by spin coating (3200 rpm and 30 s) from dilute solution (0.5-1.0 wt. %) of the BCP in toluene. As-cast films were solvent annealed in glass jars (150 mL) under a saturated toluene environment at room temperature (~288 K) for 3 h. Samples were removed from the glass jars after the desired anneal time and allowed to evaporate the trapped solvent at ambient conditions.

3.3.5. Plasma etch processes and pattern transfer to silicon

The BCP film microstructure cannot be revealed by conventional electron/force microscopy because of the presence of a surface wetting layer of PDMS **[7, 13]**. An etch process (ETCH1) was developed to reveal the PS-*b*-PDMS pattern. This etch was one component of a multi-step process that allowed pattern transfer to the substrate. Solvent annealed PS-*b*-PDMS films were first treated with a CF_4 (15 sccm) plasma for 5 s with an inductively coupled plasma (ICP) and reactive ion etching (RIE) powers of 400 W and 30 W, respectively, at 2.0 Pa with a helium backside cooling pressure of 1333.2 Pa to remove any surface PDMS layer. This was followed by an O_2 (30 sccm) plasma for 10 s with an ICP and RIE powers of 1200 W and 30 W, respectively, at 2.0 Pa with a helium backside cooling pressure of

666.6 Pa. These steps follow a similar methodology developed by Ross *et al.***[13]**. The process removes the PS component and forms an oxidized form of PDMS on the substrate. The oxidized PDMS cylinders were then used as an etch mask for pattern transfer (i.e. ETCH2). This second processing methodology involves a CHF_3 (80 sccm) and Ar (30 sccm) plasma etch for 5 s with an ICP and RIE powers of 400 W and 30 W, respectively, at 1.6 Pa to remove any residual PDMS wetting layer at the substrate surface. This milder etch treatment is critical and needed careful optimization. It is used to remove passive silica and any PDMS components at the silicon substrate surface without removing the 'etch mask' formed by the oxidised PDMS cylinders. This process was followed by a selective silicon etch using CHF_3 (80 sccm) and SF_6 (15 sccm) gases for 15 s with an ICP and RIE powers of 1200 W and 30 W, respectively, at 2.0 Pa with a helium backside cooling pressure of 1333.2 Pa to transfer the patterns into the underlying substrate. The polymers remaining after pattern transfer was removed by ETCH3. The residual oxidized PDMS cylinders were removed by a 10 s silica (SiO_2) etch based on CHF_3 (80 sccm) and Ar (15 sccm) gases with an ICP and RIE powers of 1200 W and 40 W, respectively, at 2.0 Pa with a helium backside cooling pressure of 1333.2 Pa. This is followed by 5 s O_2 (30 sccm) etch to remove the residual PS matrix and polymer brush underneath with an ICP and RIE powers of 2000 W and 100 W, respectively, at 1.3 Pa with a helium backside cooling pressure of 666.6 Pa. The etching processes were accomplished in an OIPT Plasmalab System100 ICP180 etch tool.

3.3.6. Characterization of materials

3.3.6.1. Contact angle measurements

Static contact angles (θ_a) of DI water were measured on the HMDS and polymer brush anchored surfaces at ambient temperature using a Data Physics Contact Angle (model: OCA15) goniometer. Contact angles were measured on the opposite edges of at least five drops and averaged. The values were reproducible to within 2^o.

3.3.6.2. Film thickness measurements

Film thickness was determined by ellipsometery (Plasmos SD2000 Ellipsometer) at a fixed incidence angle of 70^o. An average of five readings collected from different locations on a sample surface is reported. A two layer model (SiO_2 +

polymer brush/HMDS) for polymer brush/HMDS and a three layer model (SiO_2 + polymer brush + BCP) for total BCP film were used to fit the data.

3.3.6.3. Atomic Force Microscopy (AFM)

Atomic Force Microscope (DME 2452 DualScope Scanner DS AFM) was operated in AC (tapping) mode under ambient conditions using silicon microcantilever probe tips with a force constant of 60,000 N m^{-1} and a scanning force of 0.11 nN. Topographic and phase images were recorded simultaneously.

3.3.6.4. Scanning Electron Microscopy (SEM)

SEM images were obtained by a high resolution (< 1 nm) Field Emission Zeiss Ultra Plus-SEM with a Gemini® column operating at an accelerating voltage of 5 kV.

3.3.6.5. Focused Ion Beam (FIB)

An FEI Strata 235- FIB tool with resolution up to 10 nm was used for cross-sectional analysis. E-beam platinum was deposited above the nanowire patterns followed by the ion-beam platinum. Milling and polishing of the protective coatings was performed at the lower aperture size and then the specimen was imaged under the higher resolution Zeiss Ultra Plus-SEM.

3.4. Results and discussion

3.4.1. Surface molecular functionalization using HMDS

AFM imaging was used to characterize the surface after HMDS functionalization and the results are presented in **Figure 3.1**. AFM scans reveal a relatively flat surface irrespective of the concentration of HMDS used. There is no particulate contamination observed as shown in the images. The AFM derived root-mean-square roughness of the HMDS functionalized surfaces was in the range of 0.13–0.18 Å. As seen below, excellent coverage of the BCP on the molecular layer was observed. These observations suggest uniform surface functionalization was achieved.

The effect of HMDS functionalization was characterised by water contact angle measurements and compared with unmodified and PDMS-OH modified silicon surfaces. Data are presented in **Table 3.2**. The contact angle of as-received silicon substrates was ~45^o which was reduced to ~28^o on piranha treatment. This is

consistent with the creation of surface silanol-OH groups. The contact angle of the PDMS-OH treated surface is measured at 109^{o} and indicative of a hydrophobic surface. The contact angle of the HMDS treated substrates varied from 65-121^{o} depending on the HMDS exposure time suggesting that HDMS coverage increases with exposure time. The surfaces increase in hydrophobicity due to the formation of the low energy methyl-terminated surface layer **[24]**.

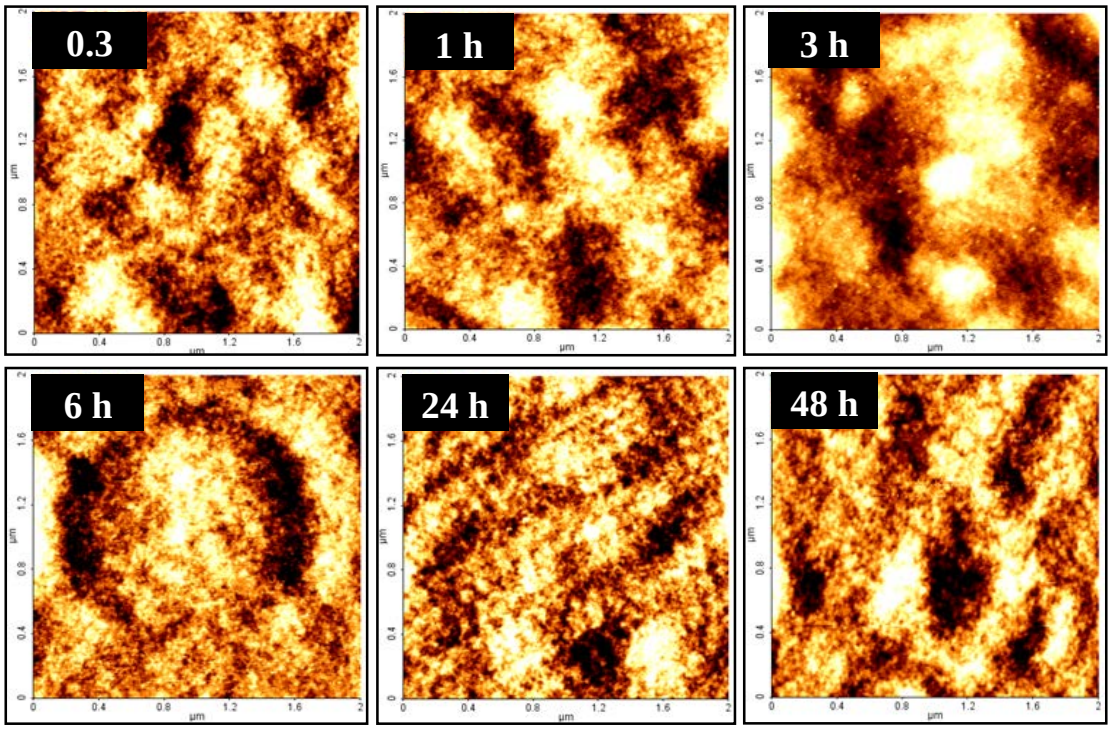

Figure 3.1. *2-D* tapping mode AFM topography images of silicon substrates functionalised with HMDS for exposure times as labelled in the images.

The HMDS functionalized surfaces were further analysed using ellipsometery and the results are presented in **Table 3.2**. Minor thickness increases are observed as the HMDS exposure increases, again consistent with increased HMDS coverage. It should be stressed that this technique cannot be used to quantify increased thickness or film density but does indicate an increase number of HMDS molecules.

The silanol-OH groups (either isolated and strongly H-bonded) developed while piranha activation reacts with HMDS, either in the vapour phase or in the liquid phase in solution to give trimethylsilyl (TMS) groups bound to the surface **[25, 26]**. The reaction between vapour phase HMDS and silanol-OH under present circumstances can be outlined below:

$$2Si\text{-}OH + (CH_3)_3Si\text{-}NH\text{-}Si(CH_3)_3 \rightarrow 2Si\text{-}O\text{-}Si(CH_3)_3 + NH_3$$

It should be noted that whether all the isolated OH groups are silylated by HMDS is not entirely clear **[25]** and attempts by ourselves to resolve this issue by FTIR and XPS were inconclusive.

Table 3.2. Film thickness and water contact angle data of the substrates prepared here

film type	HMDS or polymer concentration, wt. %	conditions of film preparation	film thickness, nm	contact angle, º
silicon substrate	-	as-received	-	42 ± 2
silicon substrate	-	piranha activation	-	28 ± 2
PDMS-OH brush layer	1.0	annealed and cleaned	4.35	109 ± 2
HMDS layer	-	vapour deposition for 0.5 h	1.31	65 ± 2
HMDS layer	-	vapour deposition for 1 h	1.37	72 ± 2
HMDS layer	-	vapour deposition for 3 h	1.41	84 ± 2
HMDS layer	-	vapour deposition for 6 h	1.56	98 ± 2
HMDS layer	-	vapour deposition for 24 h	1.67	115 ± 2
HMDS layer	-	vapour deposition for 48 h	1.82	121 ± 2
BC45	1.0	as-cast	33.77	-

3.4.2. Effect of polymer brush grafting on BCP self-assembly

A PDMS-OH brush is usually used to confer parallel (to surface plane) orientation of the PDMS cylinders in the BCP nanopattern **[7, 13]**. The PDMS-OH brush (thickness ~4.4 nm measured by ellipsometery) results in good BCP coverage but, because of favourable PDMS-PDMS interactions and a significantly lower PDMS surface energy compared to PS, results in a wetting PDMS layer at the substrate-polymer interface and at the polymer-air interface **[7, 13]**. **Scheme 3.1** shows the processing steps starting with substrate surface treatment PDMS-OH or HMDS, resultant structure formation and sequential etching steps. ETCH1 and

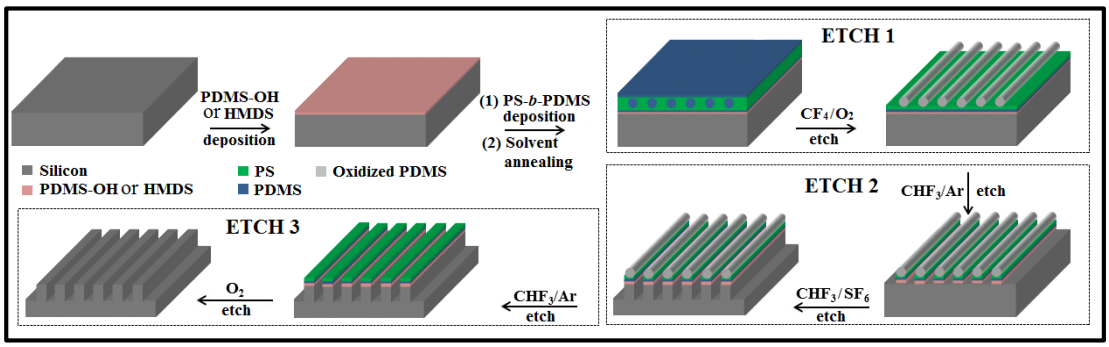

Scheme 3.1. Schematic of the process flow depicting PS-*b*-PDMS self-assembly on silicon substrate pre-coated with PDMS-OH or HMDS and subsequent plasma etching to remove PDMS wetting layer, PS matrix and pattern transfer to underlying silicon. See text for details.

subsequent SEM imaging reveal the pattern formed by the PS-*b*-PDMS BCP films in the absence **(a)** and presence **(c)** of PDMS-OH brush (**Figure 3.2)**. In the absence of the brush layer, the expected PDMS cylindrical pattern is observed with a mean correlation length around 200 nm as seen in **Figure 3.2(a)**. Macroscopic defects such as voids or regions of varying thickness (see image contrast in the SEM data) were also observed at this substrate. The BCP coverage was poor with significant dewetted regions together with multilayers of cylinders. The FIB cross-section SEM images in **Figure 3.2(b)** clearly show the presence of the varying height, multilayer stacking of cylinders but do demonstrate order is seen in both the *in-plane* and *out-of-plane* directions. The FIB-SEM image further reveals the presence of the expected wetting PDMS layer unaffected by the CF_4 and O_2 etches at the substrate-polymer interface. The presence of the wetting layer suggests that a strong substrate (SiO_2) - PDMS (BCP) interaction exists and is the origin of the wetting layer. In contrast,

with the brush layer present, the surface is significantly more conducive to the formation of controlled BCP films. The SEM data show that the film very effectively wets the entire surface in the presence of brush and produces a film thickness corresponding to a single monolayer of PDMS cylinders over the whole surface with

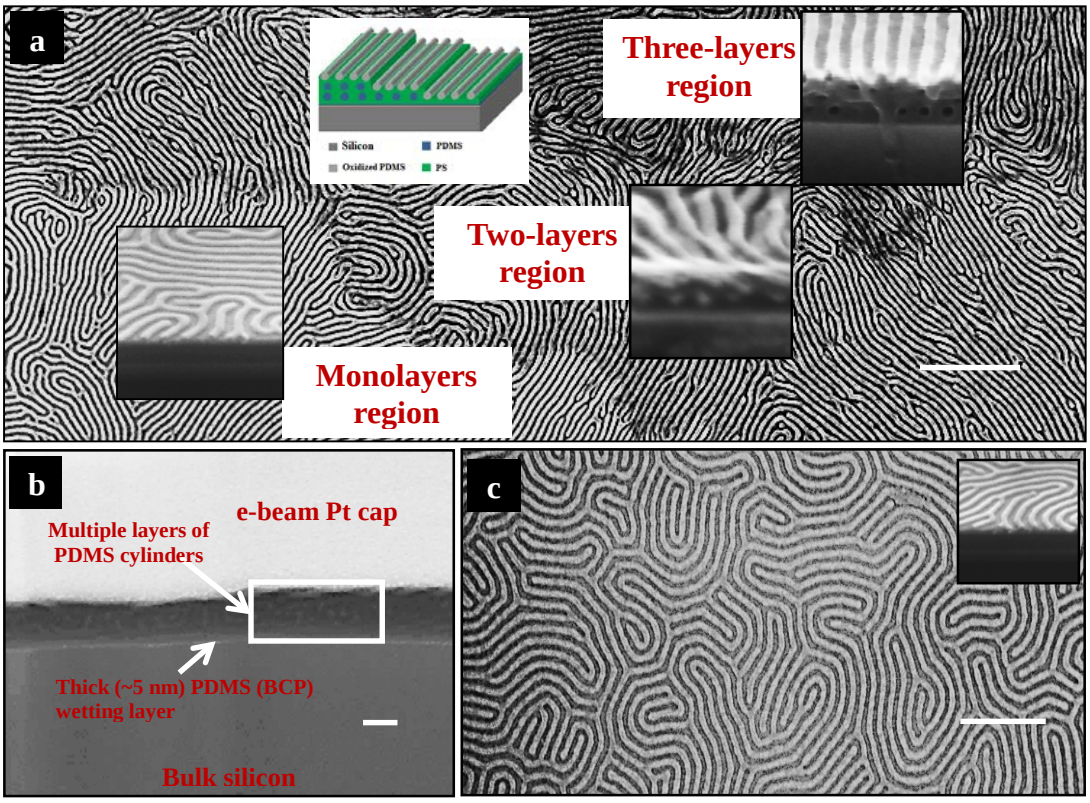

Figure 3.2. Top-down SEM images (following ETCH1) of PS-*b*-PDMS derived structures formed at **(a)** bare and **(c)** PDMS-OH functionalised silicon substrates. The insets in **(a)** and **(c)** are cross-section SEM images of monolayer and multilayers of PDMS cylinders. **(b)** FIB cross-section SEM image of etched PS-*b*-PDMS films demonstrating multiple layers of PDMS cylinders in thicker dewetted regions of **(a)**.

reasonable correlation length of the PDMS cylinders. The mean PDMS cylinder spacing, L_0, and line width, <d>, were found to be 34.7 nm and 16.3 nm, respectively and independent of use of the brush.

3.4.3. Effect of HMDS functionalization on BCP self-assembly

As seen above, the use of the PDMS-OH brush does enable good wetting and single monolayer formation at the substrate surface. It does, however, have two disadvantages. Firstly, domain orientation to the surface plane cannot be controlled and secondly, the formation of thick PDMS, silicon containing layers **(Figure**

3.2(b)) at the substrate-BCP interface because of favourable brush-PDMS block interactions. Alternative means of engineering the surface with molecular functionalization with HMDS is described here and described in **Figure 3.3**. For all HMDS exposure times, good wetting is achieved (> 90% surface area is covered). At low HMDS exposure times, vertical alignment of the cylinder structure was observed. For a 0.3 h exposure significant film thickness variation across the surface was seen. It is suggested that in this case the HDMS coverage is low and leads to an

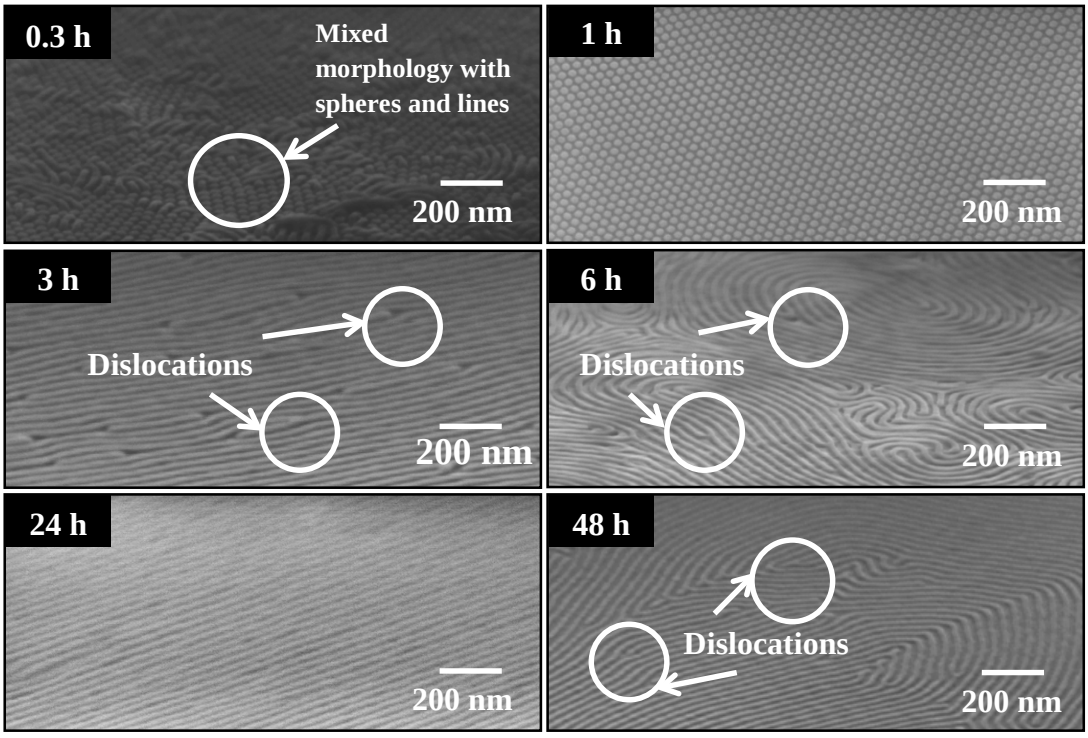

Figure 3.3. SEM images (15^{o} tilted) of ETCH1 processed PS-*b*-PDMS films on HMDS functionalised silicon substrates. Substrates were exposed to a saturated HMDS vapours for different time periods as labelled on the images.

inhomogeneous surface functionalization. This inhomogeneity is reflected in the appearance of films of mixed vertical and parallel alignment of (PDMS) cylinders as well as bilayer/multilayer arrangements. For 1 h exposure times the PDMS block orientates vertically and demonstrates the ability of HMDS to control orientation. For exposure times of 3 h and above, there was no observation of multilayer stacking or vertical cylinder orientation and the images show a highly regular structure with a progressive increase of the PDMS microdomain correlation lengths as exposure time is increased (to 24 h). The data suggest that the molecularly functionalized surface

performs equally as well as the brush technique. There is no obvious change in the mean L_0 and <d> values for these films and were similar to that observed for the PDMS-OH brush data. The PDMS *out-of-plane* cylinder diameter is measured at ~24 nm.

3.4.4. PS-b-PDMS directed self-assembly by graphoepitaxy

Further information on the HMDS functionalization and its effects on interfacial chemistry can be obtained by carrying out studies on topographically patterned substrates. These data show the capability of HMDS functionalization to combine with the topography to 'direct' the self-assembly process (DSA).

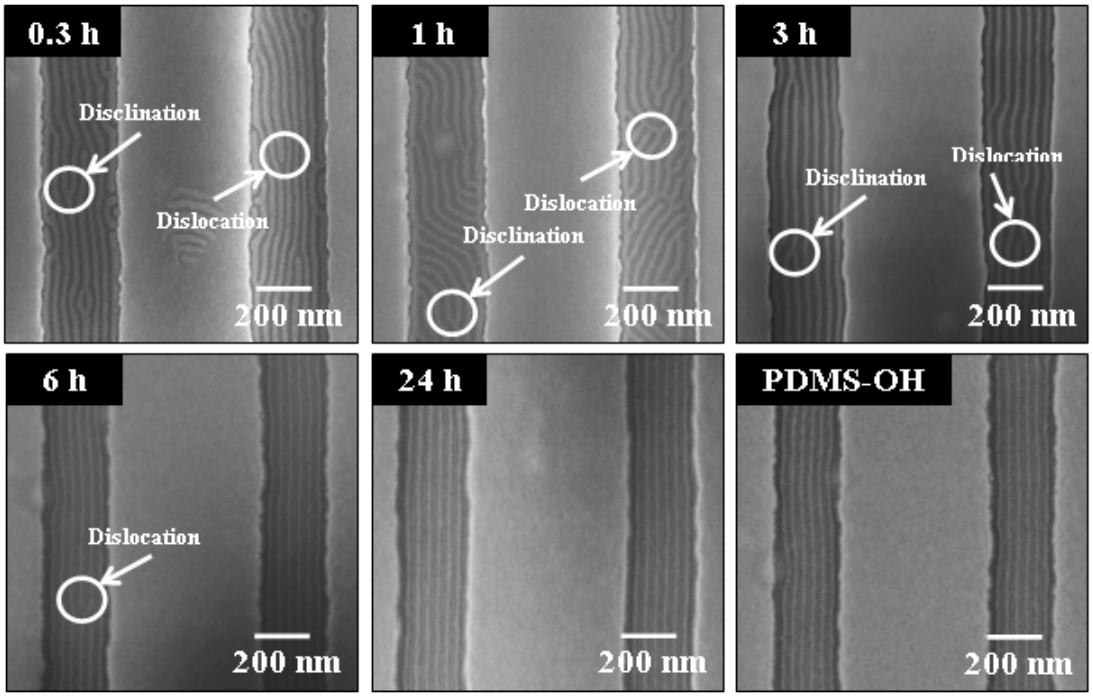

Figure 3.4. Top-down SEM images of the etched PS-*b*-PDMS films on patterned (channel width: ~250 nm) silicon substrates functionalised with HMDS and a PDMS-OH brush. The times in the figure indicate HMDS exposure periods.

Illustrative data are shown in **Figures 3.4 and 3.5** for patterned substrates with 250 nm and 500 nm channel widths and reveal that the molecularly functionalised topography is effective in bringing about DSA of the PS-*b*-PDMS system. As can be seen, HMDS can produce similar patterns and structures achieved by the PDMS-OH type brush. In all cases a horizontal orientation is maintained and no vertical morphologies could be observed. This may be because of the directing effect of the

topographical side walls. It can also be seen that alignment (to the topography) improves with the increase in HMDS exposure time irrespective of channel widths. The rather poor DSA observed at lower HMDS exposure times appears to be related to some surface neutrality at the side walls with regions of both PDMS and PS wetting observed. It is suggested that the surface of lower exposure are more 'neutral to both blocks and their 'directing' power weak. This is consistent with the data

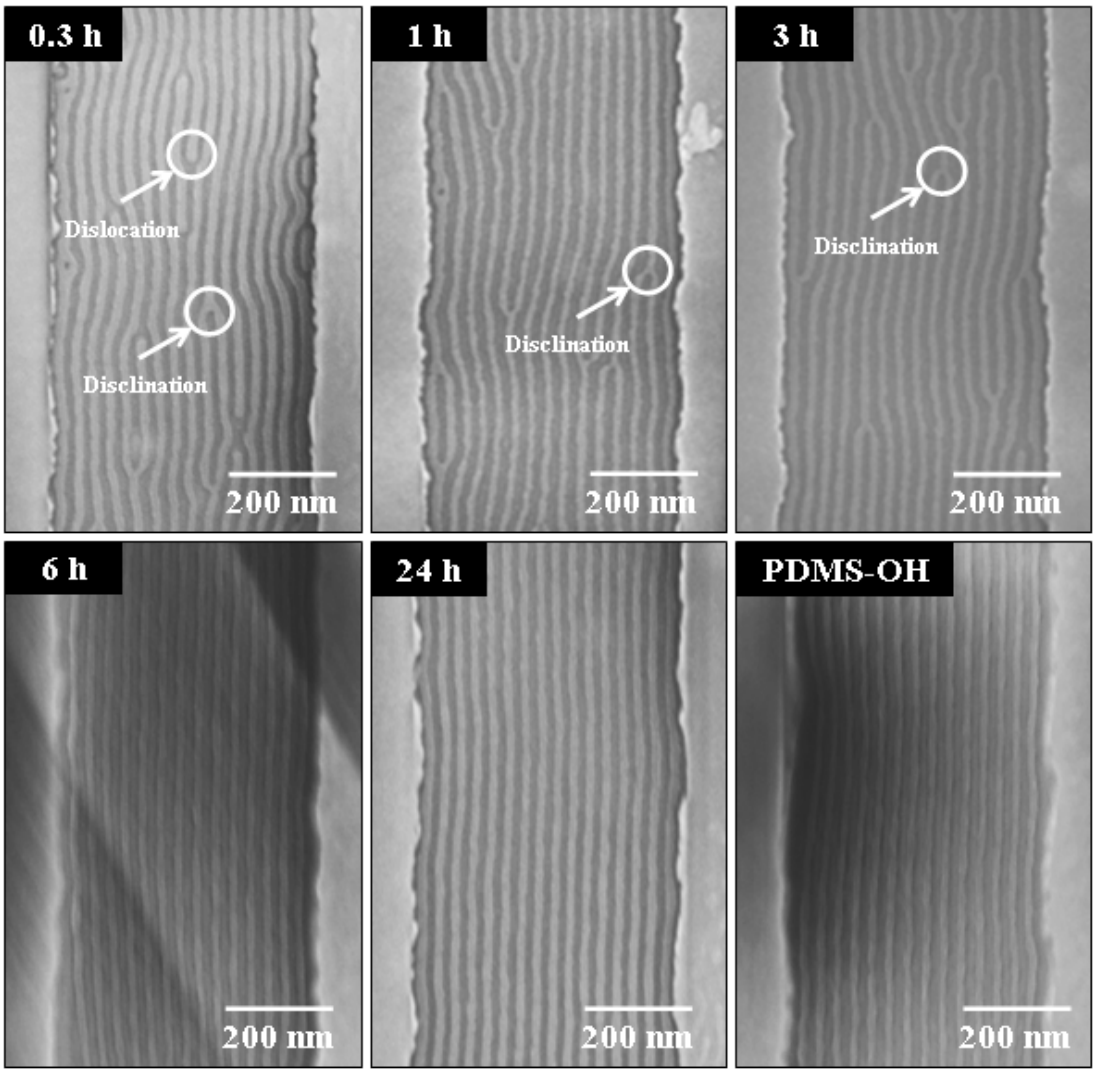

Figure 3.5. Top-down SEM images of etched PS-*b*-PDMS films on patterned (channel width: ~500 nm) silicon substrates functionalised with HMDS and PDMS-OH brush. See **Fig. 4** for details.

from the planar substrates described above. It should be noted that for exposure periods above 3 h, DSA shows little improvement. For these longer exposure periods

(and the PDMS-OH brush) DSA is highly efficient and we suggest that the majority of the defects are 'precipitated' by irregular side-wall profiles which change the width of the channel and precipitate the disclinations and dislocations observed here.

34.5. Pattern transfer to underlying substrate

The potential usefulness of the HMDS-BCP combination was demonstrated by pattern transfer to the silicon substrate was developed (*via* the ETCH 2 and ETCH 3

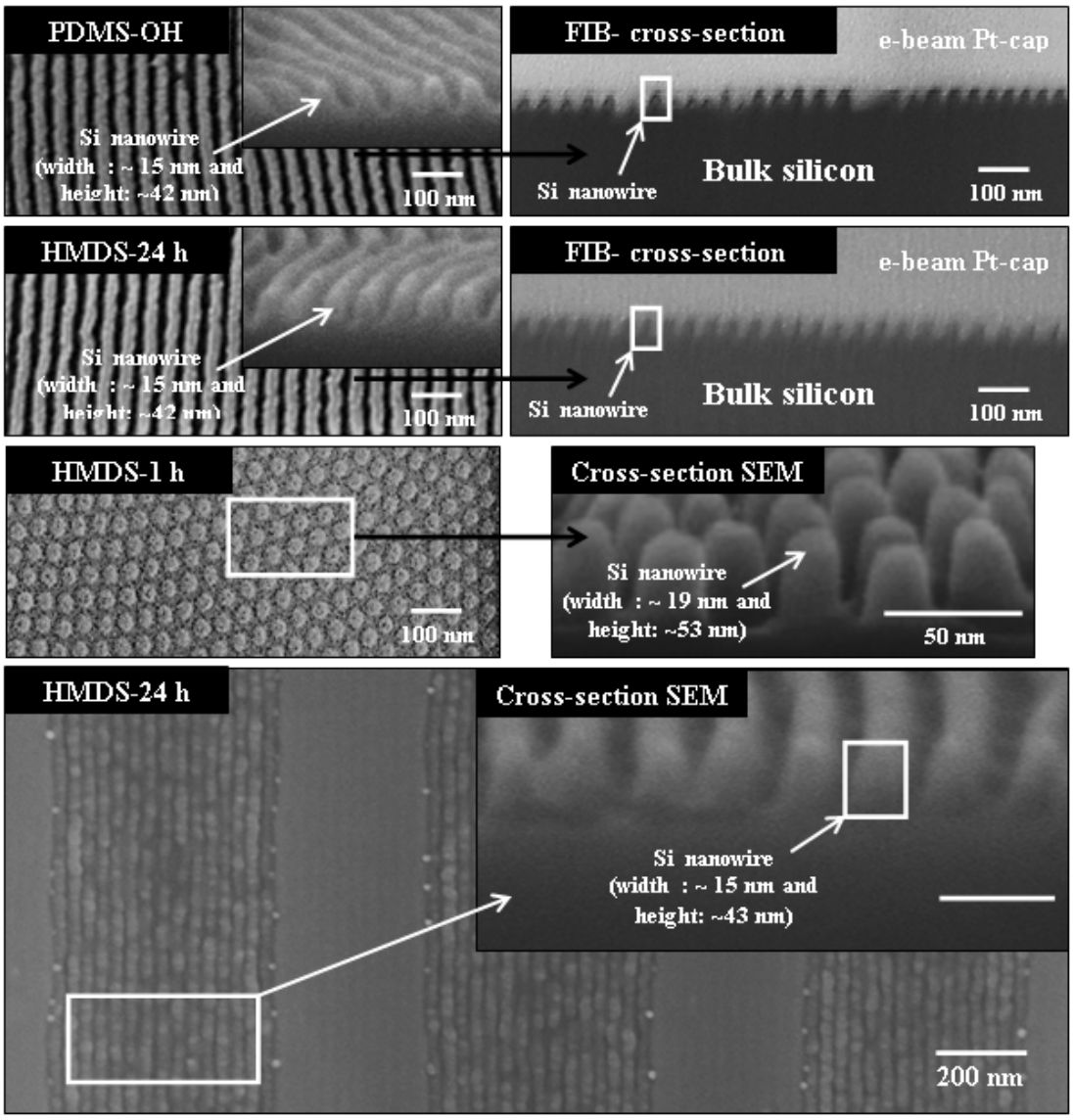

Figure 3.6. Low resolution top-down and high resolution cross-section SEM images of PDMS patterns transferred to underlying planar and patterned silicon substrates modified with PDMS-OH brush and HMDS as labelled in the images. The figure includes focused ion beam (FIB) cross-section SEM images of *in-plane* PDMS cylindrical patterns transferred to underlying silicon substrates modified with PDMS-OH brush and HMDS

procedures described above). **Figure 3.6** shows the top-down, cross-section SEM (20^o tilt) and FIB-SEM images of the silicon nanowires/pillars on planar and patterned silicon substrate pre-coated with PDMS-OH brush and HMDS obtained after the sequential etches. The HMDS and PDMS-OH functionalization show equivalent results apart from the 1 h HMDS exposure time. For PDMS-OH and longer HMDS exposure times, pattern transfer results in an arrangement of parallel nanowires at the substrate surface as shown in the SEM cross-section images. The nanowires have a width of ~15 nm and height of ~42 nm and comparison with data above suggest a high fidelity pattern transfer. The FIB cross-section SEM images confirm the SEM data. The etch process is not ideally anisotropic since the width of the nanowires is reduced slightly from the cylinder diameter seen in the data above (16.3 nm). For the HMDS exposure times of 1 h, the different orientation results not in parallel nanowires but vertical silicon pillars of diameter ~19 nm and height of ~53 nm and with excellent fidelity. We believe the increased aspect ratio of the features reflects the increased thickness of the structure (30 nm) compared to a cylinder width since the vertical orientation extends through the thickness of the film (> 30 nm).

3.5. Conclusions

One of the problems with the use of cylindrical structure forming PS-*b*-PDMS systems for the creation of nanowire type patterns is that the 'on-substrate' etch mask that is produced by oxidative etching is essentially a topographical silica pattern formed from the PDMS cylinders and the PDMS wetting layer-PDMS brush combination. Since the oxidized PDMS cylinder thickness is the same order of magnitude as the wetting layer thickness, there is considerable challenge in developing an etch process for pattern transfer to silicon since the first etch is a simple height reducing silica etch until bare silicon is revealed between the cylinders. Pattern transfer can then be achieved by a selective silicon etch. A surface functionalization which avoids the use of a PDMS brush would thus offer considerable advantage. HMDS may offer an option for developing surface functionalization of this kind. Since the number of silicon atoms is relatively low (compared to a PDMS brush), it should add negligible thickness. The PDMS-OH

brush contributes significantly to the thickness of the passive wetting layer formed at the BCP-substrate interface compared to HMDS because of it's inherent thickness developed at the time of functionalization (**Table 3.2**). Further, formation of a methylated silicon layer, may ensure a PS favouring surface is formed which would prevent formation of a PDMS wetting layer. Absolute determination of the formation of a wetting layer by direct imaging was not possible here since the thickness is around or less than the expected passive oxide layer thickness. The lack of a PDMS wetting layer can be inferred from the SEM images presented in **Figures 3.4 and 3.5**. Here, the mean width of the channels for the HMDS functionalized substrates was around 247 and 496 nm (+/- 4 nm measured over 5 μm length for two channels). However, for the PDMS functionalized substrates the apparent values were measurably less at 231 and 481 nm. We suggest that in the case of the brush coated substrates that the reduction comes from a PDMS wetting layer formed at the sidewall. These wetting layers cannot be readily observed because they have essentially the same contrast as the substrate. We thus suggest that the use of HMDS for surface chemical engineering offers some advantage compared to brush. Its performance in terms of pattern formation and DSA seems to be at least the equivalent of the brush system and it has clearly been shown to be consistent with achieving good pattern transfer.

One of the more interesting observations is that on the HMDS covered surfaces, there is a measurable increase in cylinder correlation length compared to both bare and PDMS-OH brush surfaces. On the bare silicon surface, the mean correlation length was measured at around 200 nm but was reduced at the brush to less than 75 nm. On the HMDS functionalized surface this increases to at least 500 nm except for the shortest exposures where mixed morphologies exist. This is a key advantage because this may lead to lower defect concentrations for use in manufacturing. The decreased correlation length for brush coated surface may be due to strong PDMS-PDMS interactions (i.e. the PDMS wetting layer) and polymer chain entanglement. Strong chemical interactions limit chain mobility to achieve the highest degree of order possible. On the bare surfaces, the chain entanglement is negligible and, thus, correlation lengths increased. However, the substrate-BCP interactions remain high because of the surface hydroxyls and their interaction

through and possible bonding to siloxane groups (e.g. Si-OH---OSi). This may also explain the much greater correlation length in the HMDS surface since it is most probable that the methyl groups interact only weakly *via* van der Waals type forces with the polystyrene block. As with the flat surface, there are no polymer chain entanglements to cause significant mass transport limitations.

The other advantage that appears to be demonstrated is the use of HMDS coverage to control cylinder orientation. At low HMDS exposures, it is clear that well-ordered vertical cylinder arrangements can be achieved. The simplest explanation is that partial coverage allows the PDMS cylinders to interact with surface hydroxyls (as above) and this arrangement is more favourable than complete PS or PDMS wetting. It is important to note that surface wetting in this case is not simply related to hydrophobicity and concepts such as solvent parameters. Instead, it is important to account for how the substrate and a polymer block might chemically interact.

Briefly, we have demonstrated a facile, rapid and simple method of functionalising silicon substrates with HMDS as an alternative to standard PDMS-OH polymer brush for PS-*b*-PDMS BCP self-assembly to generate nanostructures. The effectiveness of the approach is demonstrated by transferring the PDMS patterns to underlying silicon by a complex etching processes developed in our group for generating nanoscale silicon substrate patterns. We suggest that the method showed promise in guiding self-assembly and subsequent pattern transfer for nanofabrication industry.

3.6. References

[1] Black, C. T., *ACS Nano* **2007**, 1, 147.

[2] Thurn-Albrecht, T.; Schotter, J.; Kastle, G. A.; Emley, N.; Shibauchi, T.; Krusin Elbaum, L.; Guarini, K.; Black, C. T.; Tuominen, M. T.; Russell, T. P.; *Science* **2000**, 290, 2126.

[3] Thurn-Albrecht, T.; Steiner, R.; DeRouchey, J.; Stafford, C. M.; Huang, E.; Bal, M.; Tuominen, M.; Hawker, C. J.; Russell, T. P.; *Adv. Mater.* **2000**, 12, 787.

[4] Yang, S. Y.; Ryu, I.; Kim, H. Y.; Kim, J. K.; Jang, S. K.; Russell, T. P.; *Adv. Mater.* **2006**, 18, 709.

[5] Hamley, I. W.; *The Physics of Block Copolymers*, Oxford University Press, New York, **1998**.

[6] Holden, G.; Legge, N. R.; Schroeder, H. E.; Quirk, R. P.; *Thermoplastic Elastomers*, Hanser, New York, **1987**.

[7] Hobbs, R. G.; Farrell, R. A.; Bolger, C. T.; Kelly, R. A.; Morris, M. A.; Petkov, N.; Holmes, J. D.; *ACS Appl. Mater. Interfaces* **2012**, 4, 4637.

[8] Chang, J. B.; Son, J. G.; Hannon, A. F.; Alexander-Katz, A.; Ross, C. A.; Berggren, K. K.; *ACS Nano* **2012**, 6, 2071.

[9] Son, J. G.; Chang, J. -B.; Berggren, K. K.; Ross, C. A.; *Nano Lett.* **2011**, 11, 5079.

[10] Voet, V. S. D.; Pick, T. E.; Park, S. -M.; Moritz, M.; Hammack, A. T.; Urban, J. J.; Ogletree, D. F.; Olynick, D. L.; Helms, B. A.; *J. Am. Chem. Soc.* **2011**, 133, 2812.

[11] Jung, Y. S.; Chang, J. B.; Verploegen, E.; Berggren, K. K.; Ross, C. A.; *Nano Lett.* **2010**, 10, 1000.

[12] Jung, Y. S.; Ross, C. A.; *Adv. Mater.* **2009**, 21, 2540.

[13] Jung, Y. S.; Ross, C. A.; *Nano Lett.* **2007**, 7, 2046.

[14] Jung, Y. S.; Lee, J. H.; Lee, J. Y.; Ross, C. A.; *Nano Lett.* **2010**, 10, 3722.

[15] Bita, I.; Wang, J. K. W.; Jung, Y. S.; Ross, C. A.; Thomas, E. L.; Berggren, K. K.; *Science* **2008**, 321, 939.

[16] Jung, Y. S.; Jung, W.; Ross, C. A.; *Nano Lett.* **2008**, 8, 2975.

[17] Ross, C. A.; Jung, Y. S.; Chuang, V. P.; Llievski, F.; Yang, J. K. W.; Bita, I.; Thomas, E. L.; Smith, H. I.; Berggren, K. K.; Vancso, G. J.; Cheng, J. Y.; *J. Vac. Sci. Technol. B* **2008**, 26, 2489.

[18] Brinkmann, M.; Chan, V. Z. H.; Thomas, E. L.; Lee, V. L.; Miller, R. D.; Hadjichristids, N.; Avgeropoulos, A.; *Chem. Mater.* **2001**, 13, 967.

[19] Nose, T.; *Polymer* **1995**, 36, 2243.

[20] Peters, R. D.; Yang, X. M.; Kim, T. K.; Nealey, P. F.; *Langmuir* **2000**, 16, 9620.

[21] Suh, H. S.; Kang, H.; Liu, C. -C.; Nealey, P. F.; Char, K.; *Macromolecules* **2010**, 43, 461.

[22] Ramanathan, M.; Kilbey, II, S. M.; Ji, Q.; Hill, J. P.; Ariga, K.; *J. Mater. Chem.* **2012**, 22, 10389.

[23] Borah, D.; Shaw, M. T.; Rasappa, S.; Farrell, R. A.; O'Mahony, C; Faulkner, C. M.; Bosea, M.; Gleeson, P; Holmes, J. D; Morris, M. A.; *J. Phys. D: Appl. Phys.* **2011**, 44, 174012.

[24] Tasaltin, N.; Sanli, D.; Jonas, A.; Kiraz, A.; Erkey, C.; *Nanoscale Res. Lett.* **2011**, 6, 487.

[25] Sindorf, D. W.; Maciel, G. E.; *J. Phys. Chem.* **1982**, 86, 5208.

[26] Snyder, L. R.; Ward, J. W.; *J. Phys. Chem.* **1966**, 70, 3941.

4.1. Abstract

Microphase separation of block copolymer (BCPs) thin films has high potential as a surface patterning technique. However, the process times (during thermal or solvent anneal) can be inordinately long and for it to be introduced into manufacturing there is a need to reduce these times from the usual hours to minutes. We report here BCP self-assembly on two different systems, polystyrene-*block*-polymethylmethacrylate (PS-*b*-PMMA) (lamellar- and cylinder-forming) and polystyrene-*block*-polydimethylsiloxane (PS-*b*-PDMS) (cylinder-forming) by microwave irradiation to achieve ordering in short times. Unlike previous reports of microwave assisted microphase segregation, the microwave annealing method reported here was undertaken without addition of solvents. Factors such as the anneal time and temperature, BCP film thickness, substrate surface type, *etc*. were investigated for their effect of the ordering behavior. The microwave technique was found to be compatible with graphoepitaxy and in the case of the PS-*b*-PDMS system long range translational alignment of the BCP domains was observed within the topographic patterns. In order to demonstrate the usefulness of the method, the BCP nanopatterns were turned into an 'on-chip' resist by an initial plasma etch and these were used to transfer the pattern into the substrate.

4.2. Introduction

The semiconductor industry is moving towards ever smaller critical device dimensions **[1]**, however, conventional lithography based "top-down" process is approaching technical and cost limits **[2-4]**. The self-assembly of block copolymers (BCPs) might form the basis for a new lithography offering the promise for the fabrication of nanopatterns of sub-20 nm scale features without the need for expensive light sources **[5]**. BCP nanolithographic methods find industrial applications in the fabrication of nanowires **[6]**, magnetic storage devices **[7]**, nanoporous membranes **[8]**, *etc*. Excellent control over pattern dimension and structure can be achieved in BCP systems through variation of the molecular weight (M_n), relative volume fraction (ϕ) and the segmental interaction parameter (χ) and a number of different morphological structures *viz*., lamellar, cylindrical, spherical, gyroid, *etc.* **[9, 10]** can all be formed.

Despite the promise of BCP techniques and very significant research efforts, a number of challenges exist **[11-22]**. One of these is the processing time to achieve microphase separation as the ordering of BCP domains are generally achieved by thermal or solvent swelling approaches that can be time consuming **[17, 18]**. Herein, is reported a possible alternative to these methodologies that promises very short processing times based around developing a non-conventional microwave assisted BCP microphase separation process. Two different BCP systems, polystyrene-*b*-polymethylmethacrylate (PS-*b*-PMMA) (lamellar- and cylinder- forming) and polystyrene-*b*-polydimethylsiloxane (PS-*b*-PDMS) (cylinder- forming) were considered in the present investigation. These are two of the most heavily investigated systems and microphase separated thin film nanopattern structures are formed by extended vacuum annealing (of the order of 6 to 48 h **[23-30]**) and solvent annealing (of the order of 2 to 24 h **[31-41]**). It is demonstrated here that microphase segregation of BCPs compatible with that achieved by standard annealing methods can be achieved by microwave treatment **[42, 43]**. Compared to previous reports on the use of microwave heating **[42, 43]**, no solvent is used and good microphase separation can be achieved at planar and topographically patterned substrates. To demonstrate the effectiveness of the method and the regularity of the pattern with film depth, the patterns were transferred to the substrate.

4.3. Materials and methods

4.3.1. Materials

The block copolymers (BCPs) and hydroxyl-terminated homopolymer and copolymer used in the present investigation were purchased from Polymer Source, Inc., Canada and detailed characteristics are summarized in **Table 4.1**. The substrates used were silicon <100> of *p*-type with a native oxide (SiO_2) layer of ~ 2 nm thick (resistivity, ρ= 50-60 Ω cm), a silicon<100> substrate of *p*-type with 120 nm thick SiO_2 layer (resistivity, ρ= 10^{12}-10^{14} Ω cm) and a fused silica substrate. The oxide layers were deposited by a low-pressure chemical vapour deposition (LPCVD) method. We also used a *p*-doped silicon-on-insulator (SOI) (resistivity, ρ= 25-30 Ω cm) with a 20 nm device silicon layer separated through a 120 nm thick buried oxide (SiO_2) layer from the bulk silicon developed by separation by an oxygen

implantation. The topographically patterned substrates used were a *p*-type silicon <100> wafers with a LPCVD deposited silicon nitride (Si_3N_4) layer coated with a SiO_2 layer of ~ 7 nm thick (resistivity, $\rho = 10^{14}$-10^{16} Ω cm). These wafers were topographically patterned with channels of pitch 250 nm and 500 nm and depth of 50 nm (fabricated *via* 193 nm UV- lithography). It should be noted that all substrates gave similar results (since the surface chemistry is essentially due to silica) but were used to probe any substrate effects within the microwave process. Sulphuric acid, hydrogen peroxide, ethanol, acetone, iso-propanol (IPA) and toluene were purchased from Sigma-Aldrich and used as received. Deionized (DI) water was used wherever necessary.

Table 4.1. Characteristics of hydroxyl-terminated homopolymer (PDMS-OH), random copolymer (HO-PS-*r*-PMMA) brushes and block copolymers (PS-*b*-PMMA and PS-*b*-PDMS) used for present study.

M_n/ g mol^{-1}	**Polymer**	**Designation**	**Polydispersity index, M_w/M_n**	**PS mole fraction**
12,400	HO-PS-*r*-PMMA	RPB	1.25	0.58
5,000	PDMS-OH	PDM	1.07	-
36,000	PS-*b*-PMMA	BC36	1.07	0.46
74,000	PS-*b*-PMMA	BC74	1.07	0.49
104,000	PS-*b*-PMMA	BC104	1.09	0.49
67,100	PS-*b*-PMMA	BC67	1.09	0.68
45,500	PS-*b*-PDMS	BC45	1.15	0.60

4.3.2. Substrate coating with polymer brushes and BCP film preparation

Substrates were diced into 0.5 cm^2 pieces and then degreased by ultrasonication in acetone and IPA solutions for 5 min each, dried in flowing N_2 gas and baked for 2 min at 393 K in an ambient atmosphere to remove any residual IPA. This was followed by cleaning in a piranha solution (*1:3* v/v 30% H_2O_2:H_2SO_4) (***CAUTION! May cause explosion in contact with organic material!***) at 363 K for 60 min, rinsed with DI water, acetone, ethanol and dried under N_2 flow. Hydroxyl-terminated polymer brush solutions of 1.0 wt. % in toluene were spin-coated (P6700 Series Spin-coater, Speciality Coating Systems, Inc., USA) onto substrates at 3000

rpm for 30 s. Samples were annealed in a vacuum oven (Townson & Mercer EV018) at 443 K under vacuum (-*100 kPa*). This procedure provides chemically anchored brushes by condensation reactions between -OH groups at the substrate surface and on the brush. Unbound polymers were removed by ultrasonication (Cole-Palmer 8891 sonicator) and rinsing in toluene, and dried for 30 min at 333 K in an ambient atmosphere to remove any residual toluene. A random HO-PS-*r*-PMMA brush has to be used to define orientation of the lamellae structure as perpendicular to the surface plane **[11-13]**. A PDMS brush orientates the PDMS cylinder structure parallel to the surface plane and allows good surface wetting **[31, 41]**. BCPs (PS-*b*-PMMA and PS-*b*-PDMS) were dissolved in toluene to yield solutions of 0.7-3.0 wt. % and then spin-coated onto the brush anchored surfaces at 3200 rpm for 30 s and immediately used for microwave irradiation.

4.3.3. Non-conventional microwave anneal of BCP films

The microwave annealed experiments were performed in a microwave synthesizer, CEM Discover LabMate (CEM Microwave Technology Ltd., UK) with the IntelliVent™ Pressure Control System and CEM's Synergy™ software. The system has an *in-built* feature of focusing the microwaves with maximum efficiency into the sample cavity. CEM's Windows®-based Synergy software was used to control the microwave parameters (power, temperature, time and pressure) as well as data handling. BCP coated substrates were accommodated inside the reaction tube which was sealed, placed inside the reaction chamber, and irradiated with microwave energy. The desired temperature was achieved through microwave feedback control which required 20-100 s depending upon the target temperature. The preset anneal time started once the target temperature was achieved. It should be noted that sufficient microwave power was applied to achieve and hold the chosen temperature in reaction vessel. The anneal time considered was in the range of 30-360 s. It should be noted that the reaction vessel requires around 30-100 s to cool to ambient conditions following use. During this period some organization and assembly is expected. The essential parameters, input power, temperature and pressure were recorded during the process. Dewetting of the BCP film was not observed in any of the experiments.

4.3.4. Conventional thermal anneal of BCP films

BCP films were thermal annealed in the temperature range of (323-453) K under vacuum (*-100 kPa*) for (60-1800) s, to induce phase separation and evaporate any remaining solvent. Thin films were removed from the oven immediately after annealing and allowed to cool naturally in ambient.

4.3.5. Plasma etching of BCP films

The microwave annealed PS-*b*-PMMA films were subjected to selective removal of PMMA block by inductively coupled plasma (ICP) etches in an OIPT Plasmalab System 100 ICP180 etcher. The process was accomplished with an Ar/O_2 etch recipe of Ar (5 sccm) and O_2 (15 sccm) at 1.3 Pa and 100 W for 6 s to generate PS mask structures. Full details are given elsewhere **[11-13]**. It should be noted that for process stability, the PS microdomains of the BCP film must interact the substrate sufficiently to retain the structural integrity of the film. It is accepted that the brush layer provides good film stability because the brush layer penetrates into the BCP thin films, thus anchoring it to the surface **[11-13, 65, 66]**. As can be seen below, it appears that the films retain this robustness *via* similar mechanism and suggests that the microwave anneal also allows interpenetration of brush layer and BCP domains.

PS-*b*-PDMS BCP films do not readily show the microphase separated structure because of the presence of a surface wetting layer of PDMS which must be removed to reveal the domain structure **[31, 41]**. Films were first treated with a CF_4 (15 sccm) plasma for 5 s with an ICP and reactive ion etching (RIE) powers of 400 W and 30 W, respectively, at 2.0 Pa with a helium backside cooling pressure of 1333.2 Pa to remove any surface PDMS layer. This was followed by an O_2 (30 sccm) plasma for 10 s with an ICP and RIE powers of 1200 W and 30 W, respectively, at 2.0 Pa with helium backside cooling pressure of 666.6 Pa. These steps follow similar methodology developed by Ross *et al* **[41].** The process removes the PS component and forms an oxidized form of PDMS on the substrate. This etch step is referred as ETCH1.

4.3.6. Silicon etch for nanostructure pattern formation

For the PS-*b*-PMMA BCP, an SF_6/CHF_3 ICP etch was carried out on the samples using the PS structure as an etch masks. The etch used was carried out at 2.0

Pa and 500 W with SF_6 (15 sccm) and CHF_3 (80 sccm) for 9 s to transfer the template structure to underlying substrate. Remaining PS was removed using an O_2 (30 sccm) ash recipe at 2.0 Pa and 2000 W for 10 s.

The oxidized PDMS cylinders formed by the sequential CF_4 and O_2 etches were used as an etch mask for pattern transfer in PS-*b*-PDMS BCP by an etch process designated as ETCH2. The pattern transfer step involved an initial CHF_3 (80 sccm) and Ar (30 sccm) plasma etch for 5 s with an ICP and RIE powers of 400 W and 30 W, respectively, at 1.6 Pa to remove any residual PDMS wetting layer at the substrate surface. This milder etch treatment was critical and needed careful optimisation. It was used to remove passive silica and any PDMS components at the silicon substrate surface without removing the 'etch mask' formed by the oxidised PDMS cylinders. This process was followed by a selective silicon etch using CHF_3 (80 sccm) and SF_6 (15 sccm) gases for 15 s with an ICP and RIE powers of 1200 W and 30 W, respectively, at 2.0 Pa with helium backside cooling pressure of 1333.2 Pa to transfer the patterns into the underlying substrate. The polymers remained after pattern transfer was removed by ETCH3. The residual oxidized PDMS cylinders were removed by a 10 s silica (SiO_2) etch based on CHF_3 (80 sccm) and Ar (15 sccm) gases with an ICP and RIE powers of 1200 W and 40 W, respectively, at 2.0 Pa with a helium backside cooling pressure of 1333.2 Pa. This is followed by 5 s O_2 (30 sccm) etch to remove the residual PS matrix and polymer brush underneath with an ICP and RIE powers of 2000 W and 100 W, respectively, at 1.3 Pa with a helium backside cooling pressure of 666.6 Pa. The etching processes were accomplished in an OIPT Plasmalab System100 ICP180 etch tool.

4.3.7. Characterization of materials

4.3.7.1. Contact angle measurement

Advancing contact angles (θ_a) of deionized water on the substrates was measured using a Data Physics Contact Angle (model: OCA15) goniometer. Contact angles were measured on the opposite edges of at least five drops and averaged. The values were reproducible to within 1.5^o.

4.3.7.2. Film thickness measurements

BCP film thicknesses were measured with a spectroscopic ellipsometer "Plasmos SD2000 Ellipsometer" at a fixed angle of incidence of 70^o, on at least five

different places on the sample. A two layer model (SiO_2 + polymer brush) for polymer brushes and a three layer model (SiO_2 + polymer brush + BCP) for total BCP films were used to simulate experimental data.

4.3.7.3. Temperature measurements by infrared thermometer

The actual temperature of the substrates in the (BCP + substrate) systems were measured by an Infrared Thermometer (SMART SENSOR, AR330 (-305 K-603 K)) immediately after the microwave experiment.

4.3.7.4. Fourier Transform Infra-Red (FTIR) measurements

An IR 610, Varian infrared spectrometer was used to record the FTIR spectra. The measurements were performed in the spectral range of 400-500 cm^{-1}, with a resolution of 4 cm^{-1} and data averaged over 32 scans.

4.3.7.5. Atomic force Microscopy (AFM)

An Atomic Force Microscope (DME 2452 DualScope Scanner DS AFM) was operated in AC (tapping) mode under ambient conditions using silicon microcantilever probe tips with a force constant of 60,000 N m^{-1} and a scanning force of 0.11 nN. Topographic and phase images were recorded simultaneously. Fast Fourier Transforms (FFT) of the topographic images was used to measure the degree of alignment and the presence of defects/non-regular patterns.

4.3.7.6. Scanning Electron Microscopy (SEM)

Scanning electron microscope (SEM) images were obtained by a high resolution (< 1 nm) Field Emission Zeiss Ultra Plus-SEM with a Gemini® column operating at an accelerating voltage of 5 kV.

4.4. Results and discussion

A schematic depicting the microwave anneal of BCPs is presented in **Scheme 4.1(a)**. It should be noted that all the microwave irradiated experiments were performed without the aid of solvent unlike the work reported by Buriak *et al* **[43]**. As can be seen in **Scheme 4.1(a)**, the substrate coated with BCP was placed in a reaction tube specially designed for microwave experiments, sealed and then irradiated with microwave energy. The detailed self-assembly steps starting with hydroxyl-terminated polymer brush grafting, resultant structure formation and plasma etching steps are schematically shown in **Scheme 4.1(b)**. A number of

parameters were investigated to demonstrate the diversity of the microwave anneal process which includes: microwave irradiation time and temperature, BCP morphology and molecular weight, substrate resistivity, and directed self-assembly by graphoepitaxy.

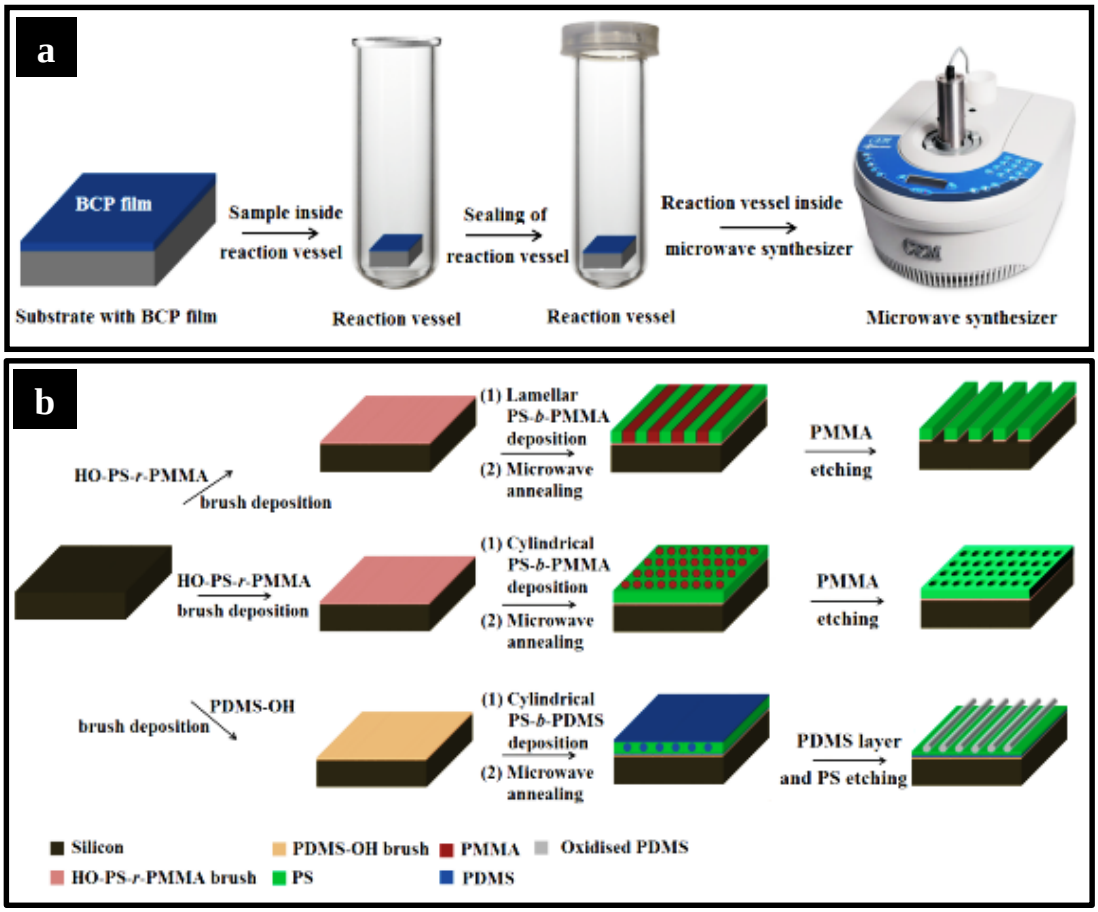

Scheme 4.1. (a) Scheme depicting the process of microwave annealing of BCP films in the absence of solvent: BCP film onto substrate, putting the sample into the reaction vessel and sealing off, and finally microwave annealing in the synthesizer to achieve BCP ordering. **(b)** Schematic representation of the process flow showing BCP self-assembly on silicon substrate pre-coated with hydroxyl-terminated polymer brushes and subsequent plasma etching. See text for details.

4.4.1. Microwave assisted self-assembly of BCPs

The PS-*b*-PMMA BCPs were spin-casted from toluene solutions onto the polymer brush coated substrates prior to irradiation with microwave energy. The thickness of the as-cast BCP films were determined by ellipsometry and the data are

compiled in **Table 4.2**. It can be seen in **Table 4.2** that the average film thickness is ~40 nm for 1.0 wt. % coating solutions irrespective of the PS-*b*-PMMA molecular

Table 4.2. Water contact angle and film thickness (ellipsometery) of polymer brush layers and BCP films on substrate surfaces.

Material	**Deposition Condition**	**Contact angle /º**	**Thickness /nm**	**Pitch from AFM, SEM/nm**
RPB/ Si substrate	annealed/cleaned	83±1.5	5.1	-
PDM/ Si substrate	annealed/cleaned	112±1.5	4.3	-
BC36/ Si substrate	RPB + BC36 (0.7 wt. %)	-	30.3	26
BC36/ Si substrate	RPB + BC36 (1.0 wt. %)	-	35.4	26
BC36/ Si substrate	RPB + BC36 (1.5 wt. %)	-	38.7	26
BC74/ Si substrate	RPB + BC74 (1.0 wt. %)	-	39.2	42
BC104/ Si substrate	RPB + BC104 (1.0 wt. %)	-	40.6	54
BC67/ Si substrate	RPB + BC67 (1.0 wt. %)	-	33.1	36
BC67/ Si substrate	RPB + BC67 (2.0 wt. %)	-	48.7	36
BC67/ Si substrate	RPB + BC67 (3.0 wt. %)	-	56.3	36
BC45/ Si substrate	PDM + BC45 (1.0 wt. %)	-	36.6	35

weight but this thickness increases with the concentration of the polymer solution as expected. Symmetric PS-*b*-PMMA thin films prepared the brush layer; exhibit a lamellar morphology consisting of vertically orientated lamellae of PS and PMMA.

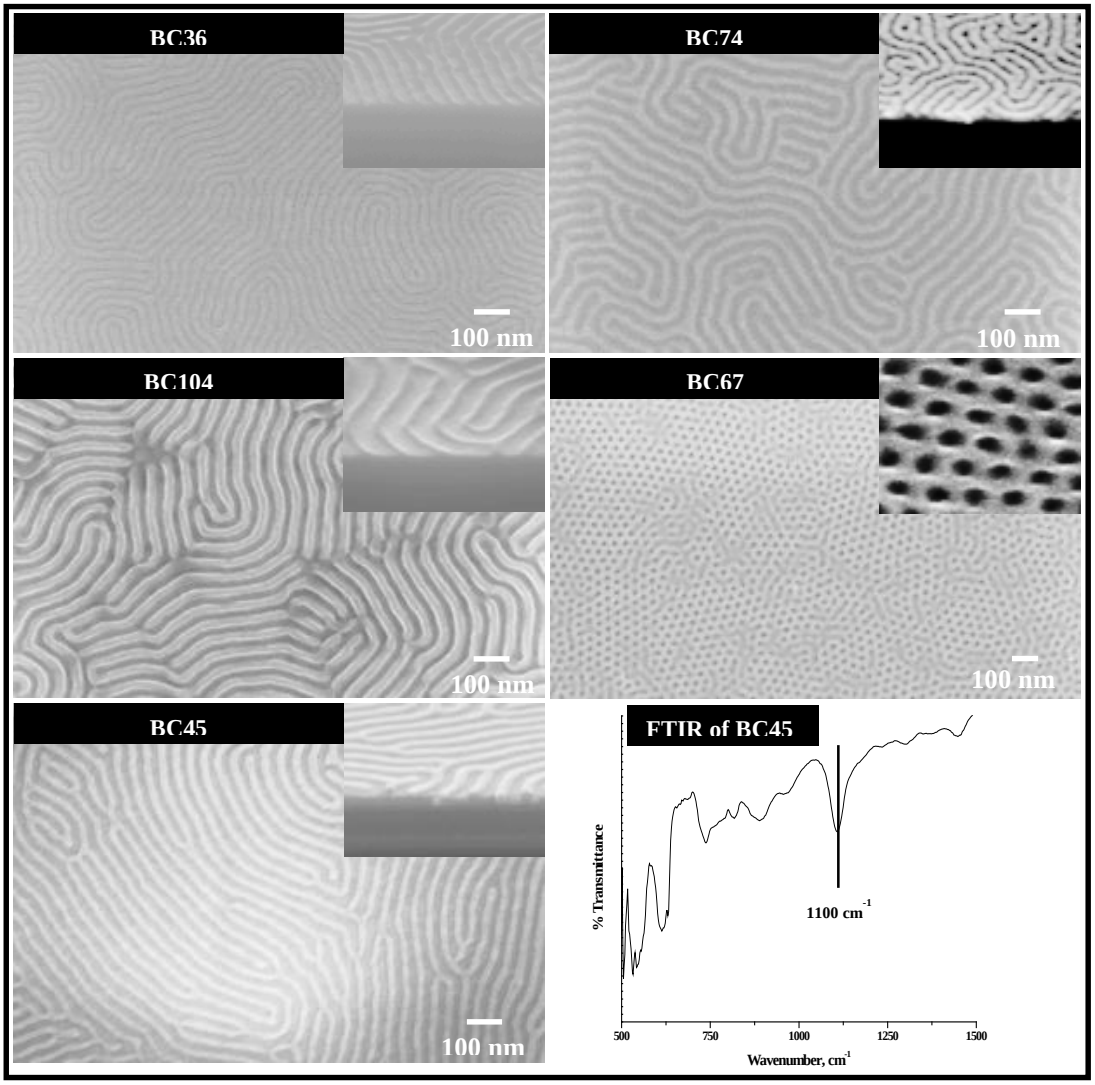

Figure 4.1. Top-down and off-axis (inset) cross-section SEM images of PS-*b*-PMMA and PS-*b*-PDMS BCP films after selective plasma removal of the PMMA component, and the top PDMS wetting layer and partial PS matrix for PS-*b*-PMMA and PS-*b*-PDMS, respectively, (light grey lines/matrix are PS/PDMS and darker lines/holes are voids created following PMMA/PS removal) on silicon substrates as labelled in the images. BCP films were microwave annealed at 323 K for 60 s. FTIR spectrum of the oxidized PDMS cylinders formed from the PS-*b*-PDMS (BC45) using CF_4 and O_2 etches.

Figure 4.1(a, b, c) shows the top-down SEM images of PMMA etched lamellar PS-*b*-PMMA BCP of three different molecular weights on silicon substrates

pre-coated with HO-PS-*r*-PMMA brush (ellipsometry thickness ~5.1 nm, (**Figure AI.1**)) (Note that PMMA removal was used to develop image contrast). The BCP films were microwave irradiated at 323 K for 60 s and sufficient microwave power (~100 W) used to maintain this temperature. It is apparent that the process produced ordering of the BCP irrespective of the molecular weight. Interestingly, the optimum pattern ordering is observed with the lowest molecular weight PS-*b*-PMMA, BC36. This can be explained by the lower molecular weight favouring greater molecular motion allowing the minimum energy conformation to be achieved during annealing. The SEM cross-section images presented in insets to **Figure 4.1** demonstrate PMMA removal and the formation of PS line structures. The lamellar repeat distances are compiled in **Table 4.2** and it is clear that PS pitch and feature size are directly determined by the molecular weight of the BCP. The dimensions are close to those we have previously measured using thermal anneal processes and suggests that no polymer rearrangements, *etc*. are caused by the microwave technique.

The results for the cylinder- forming PS-*b*-PMMA, BC67 on substrate pre-coated with HO-PS-*r*-PMMA brush and microwave annealed at 323 K for 60 s is presented in **Figure 4.1(d)**. The BCP film was cast from a 2.0 wt. % of the polymer solution in toluene yielding a film thickness of ~49 nm **(Table 4.2)**. The top-down SEM images of the etched film confirm a vertical alignment of cylinders and suggest removal of the PMMA domains. It was observed that there is minor enlargement of the pore diameter (pores result from PMMA cylinder removal) during the selective etch process. Comparison of SEM and AFM images suggests that the pore size is 16.2 nm compared to a cylinder size of 18.7 nm measured from equivalent AFM images. However, the center-to-center distance between pores was not modified during the PMMA removal process and the mean value obtained was 35.1 nm in agreement with AFM data (**Table 4.2**). The increased pore diameter is probably due to isotropic etching of the polymer and/or possibly plasma induced strong cross linking of the PS matrix **[44]**.

Figure 4.1(e) shows the results of the oxidised PDMS cylinders after a sequential CF_4 and O_2 etches obtained from the microphase separated PS-*b*-PDMS film on PDMS-OH brush (ellipsometery thickness ~4.3 nm) microwave annealed at 323 K for 60 s. The SEM image shows a single monolayer of PDMS cylinders and

clearly demonstrates the efficacy of etch chemistry to reveal the cylindrical patterns. It is evident from the data in **Figure 4.1(e)** that well-ordered phase separation is seen over macroscopic distances. The mean PDMS cylinder spacing, L_0, and line width, <d>, were found to be 36.4 nm and16.2 nm, respectively. It can also be seen from the image that the oxidized PDMS domains have become rounded during the etch process indicating that it is partially isotropic. The oxidation of the PDMS cylinders during this pre-etch step is confirmed by FTIR with the detection of a Si-O-Si signal at 1100 cm^{-1} **[45]** as displayed in **Figure 4.1(f)**. Dewetting is a major issue with high χ BCP systems such as PS-*b*-PDMS leading to multilayer pattern formation in some locations on the substrate upon solvent annealing. However, the dewetting was not there in microwave annealed PS-*b*-PDMS films which is advantageous in getting uniform monolayer of *in-plane* PDMS cylinders for subsequent pattern transfer to underlying silicon substrate. Absence of dewetting could be due to transient irradiation time as compared to a longer solvent anneal time usually followed.

4.4.2. Effect of BCP film thickness on microwave assisted self-assembly

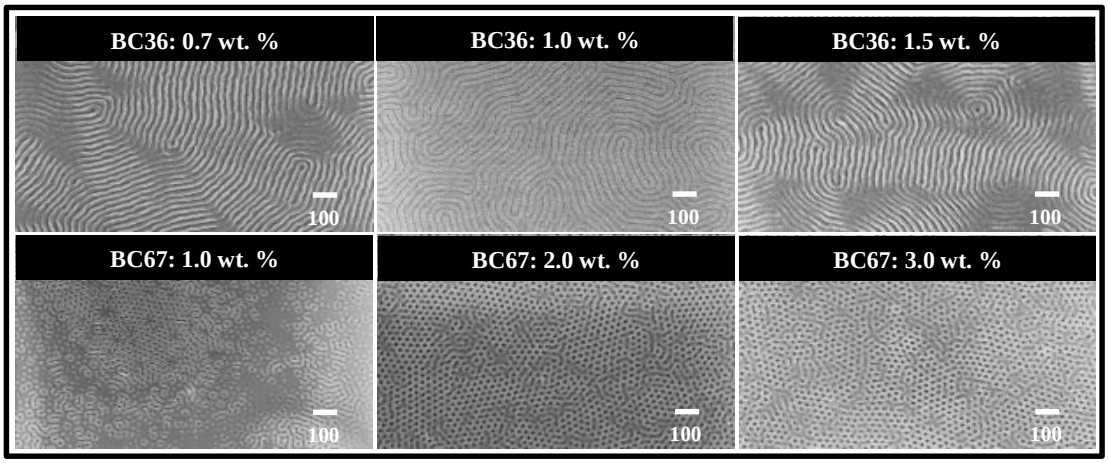

Figure 4.2. Top-down SEM images of the PS-*b*-PMMA BCP (BC36 and BC67) films after selective plasma removal of the PMMA component (light grey lines are PS and darker lines are voids created following PMMA removal). The BCP film thicknesses were varied as labelled in the images and were microwave annealed at 323 K for 60 s.

Microphase separation derived BCP thin film nanopatterns can display orientations strongly dependent on film thickness **[46-48]**. In order to verify such effects in microwave processed films, a systematic study of the film thickness effect

on self-assembly on BC36 and BC67 was performed. Results are presented in **Figure 4.2**. The anneal temperature and time were fixed at 323 K and 60 s, respectively. SEM images were taken at different locations on the substrate and show that the orientation is homogeneous over the entire surface. It is evident that 1.0 wt. % of BC36 on HO-PS-*r*-PMMA brush gives the best results with a high

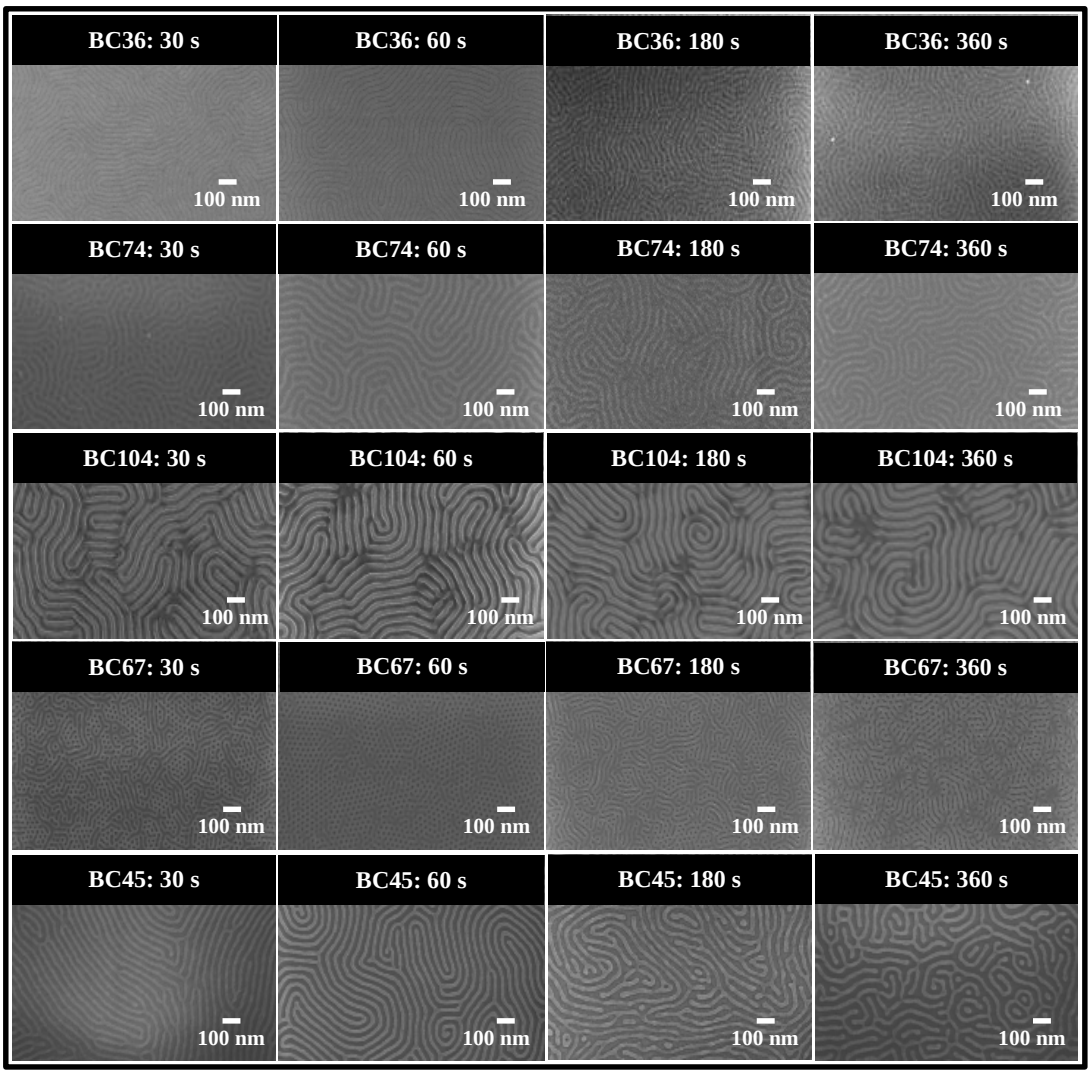

Figure 4.3. Top-down SEM images of the PS-*b*-PMMA and PS-*b*-PDMS BCPs films after selective plasma removal of the PMMA component, and the top PDMS wetting layer and partial PS matrix for PS-*b*-PMMA and PS-*b*-PDMS, respectively, (light grey lines/matrix are PS/PDMS and darker lines/holes are voids created following PMMA/PS removal). The BCP films were microwave annealed at a target temperature of 323 K for different time periods as labelled in the images.

degree of ordering and uniform film thickness. However, at the other concentrations, the films became rough on microwave irradiation and significant areas that were

featureless can be identified in the SEM images. This is consistent with thicknesses that are not commensurate with the domain spacing and parallel alignment or absence of pattern in some areas.

It can be seen that microwave annealing of BC67 on HO-PS-*r*-PMMA brush can result in vertical, parallel or mixed orientation of the PMMA cylinders dependent on film thickness as seen in thermal or solvent annealed processing **[46-49]**. For a 1.0 wt. % BCP casting solution (~33 nm thickness) vertical and parallel cylinder orientation can be observed as well as featureless regions (**Figure 4.2**). We suggest this film thickness is below that need to produce a coherent film thickness with featureless regions representing polymer-free areas and changes in orientation reflecting changing thickness within BCP islands. However, hexagonally ordered cylindrical PMMA microdomains in a PS matrix oriented perpendicular to the substrate are observed with BCP concentrations of 2.0 and 3.0 wt. %. This suggests the film thickness allows regular coating and that the brush preferentially favours this orientation. This hexagonal phase BCP exhibits a hexagonal arrangement of phase of PMMA cylinders in a PS matrix with a centre-to-centre spacing of about 35 nm.

4.4.3. Effect of microwave anneal time on self-assembly

Previous studies of conventional thermal annealing shows that BCP morphology and ordering depends upon the anneal time **[13]** and, therefore, a series of time dependent experiments were undertaken here. Films were microwave irradiated for various lengths of time (30-360 s) at a constant temperature of 323 K with sufficient microwave power (~100 W) to maintain the temperature and the results are presented in **Figure 4.3**. The results for lamellar PS-*b*-PMMA BCPs show microphase separation across the surface irrespective of anneal time and molecular weight. However, the patterns became more disordered and increase in the number of defect sites with the increase of anneal time particularly with lower molecular weight PS-*b*-PMMA (BC36). This might suggest that extended annealing periods cause such extensive molecular motion in the small, more mobile system that the effective order-disorder phase boundary is crossed and disorder is ‘frozen-in’ on cooling, *etc*.

The results of BC67 system reveal an interesting trend as can be seen in **Figure 4.3**. At short and long anneal times much higher concentrations of pattern orientation and structural defects are observed whilst a 60 s anneal appears to be optimum for generating patterns of good structural order. As above, it would appear that longer anneal periods lead to structural disorder due to high chain mobility. It might be suggested that a 30 s anneal is not long enough to reach structural order. It would thus appear that the microwave anneal method as used here is somewhat complex and the structures observed are kinetically 'trapped' rather than a progression towards the thermodynamically stable state as seen in conventional methods.

The time dependence of microwave annealing on the microphase separation of PS-*b*-PDMS BCP thin films is presented in **Figure 4.3**. As seen for PS-*b*-PMMA, the patterns became more disordered and defects density increases with anneal time. The mean PDMS cylinder spacing, L_0, and line width, <d>, were found to be 36.2 nm and 15.9 nm, respectively.

4.4.4. Effect of microwave anneal temperature on self-assembly

The process mechanism described above suggests that the temperature used in the microwave assisted assembly process might be important and data are presented in **Figure 4.4**. For PS-*b*-PMMA BCPs, the anneal temperature was chosen in the range of 323-453 K (60 s anneal period), below and above the glass transition temperatures (Tg) of PS and PMMA blocks. Generally, the anneal temperature has a lesser effect than might be first considered. From **Figure 4.4**, it is evident for all the systems studied that BCP film ordering deteriorates as the temperature is increased (most notably for lower Molecular weight BCPs) and that optimum structural order is attained well below Tg. The lack of very dramatic effects suggests that thermal motion of the polymer chains is not very important and ordering arises from chain motions caused by microwave excitement and that the 'effective' temperature of the film is significantly higher than the process temperature as measured in the instrument. **Figure 4.4** shows the temperature evolution of PS-*b*-PDMS BCP ordering in the temperature range of 323-453 K. A shorter anneal time of 30 s was considered optimum based on the results of time evolution described above. **Figure 4.4** reveals asimilar temperature dependence as that seen for the PS-*b*-PMMA system

with less structurally well-defined patterns observed at higher temperatures. Also observed was a small increase in the mean PDMS and at the highest temperature the

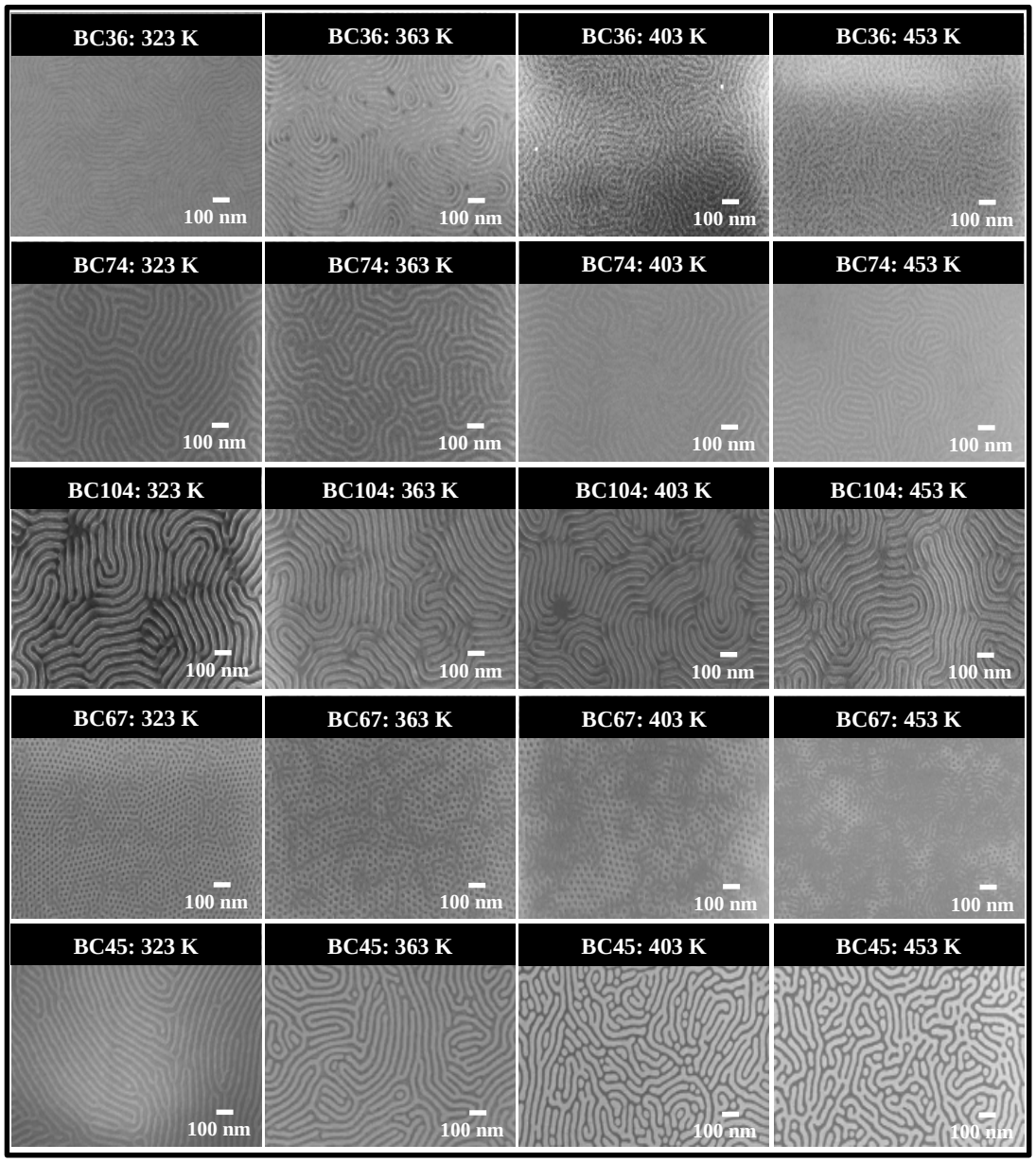

Figure 4.4. Top-down SEM images of the PS-*b*-PMMA and PS-*b*-PDMS BCPs films after selective plasma removal of the PMMA component, and the top PDMS wetting layer and partial PS matrix for PS-*b*-PMMA and PS-*b*-PDMS, respectively, (light grey lines/matrix are PS/PDMS and darker lines/holes are voids created following PMMA/PS removal). The BCP films were microwave annealed at a target temperature as labled in the images for 60 s for PS-*b*-PMMA and 30 s for PS-*b*-PDMS BCPs.

cylinder spacing and line width were found to be 38.3 nm and 17.7 nm, respectively compared to corresponding values of 36.2 nm and 15.9 nm seen at the lowest

temperature. This is consistent with some 'freezing-in' of free volume caused by microwave excited motion of both blocks.

4.4.5. Effect of substrate surface type on microwave assisted self-assembly

A wide range of substrates *e.g.*, silicon, silicon dioxide, silicon-on-insulator, silicon nitride, *etc.*, were investigated here and only limited dependence was observed. Note that the resistivity of the substrates used varied in the following way: bulk Si, SiO_2/bulk Si, Si/SiO_2/bulk Si and Si_3N_4/bulk Si substrates had resistivities of ρ= 50-60 Ω cm, 10^{12}-10^{14} Ω cm, 25-30 Ω cm and 10^{14}-10^{16} Ω cm, respectively. The BCP films formed on these were microwave annealed at 323 K for 60 s for PS-*b*-PMMA and for 30 s for PS-*b*-PDMS BCPs. All films exhibited pattern formation. **Figure 4.5** shows the results of the lamellar- forming PS-*b*-PMMA (BC36) on various substrates. Water contact angle measured on these surfaces after the brush

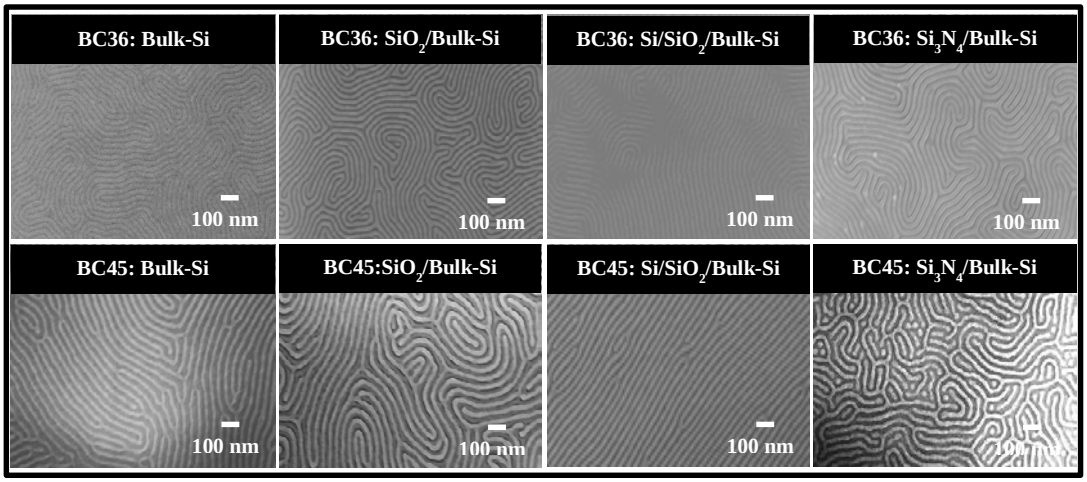

Figure 4.5. Top-down SEM images of PS-*b*-PMMA (BC36) and PS-*b*-PDMS (BC45) BCP films after selective plasma removal of the PMMA component, and the top PDMS wetting layer and partial PS matrix for PS-*b*-PMMA and PS-*b*-PDMS, respectively, (light grey lines/matrix are PS/PDMS and darker lines/holes are voids created following PMMA/PS removal) on various substrates as labelled in the images. BCP films were microwave annealed at 323 K for 60 s for PS-*b*-PMMA and 30 s for PS-*b*-PDMS BCPs.

Grafting shows small variations in the hydrophobicity/hydrophilicity of the substrates as might be expected because of the use of the same polymer brush. The results presented in **Figure 4.5** show a little correlation between the BCP ordering and the substrate resistivity. The results are inconsistent with the work of Buriak *et al.* **[43]** which suggested that the oscillating electric field of the microwave

irradiation excites positive carriers in doped silicon thereby converting microwave energy into thermal energy within the silicon substrate. However, our experiments are quite different in that temperature is strictly controlled and no solvent is used. In this way, the efficiency of substrate heating is less important because the microwave power is adjusted automatically. The results of PS-*b*-PDMS (BC45) on the same substrates are presented in **Figure 4.5** show similar behaviour.

4.4.6. Microwave assisted directed self-assembly

The seminal work of Buriak *et al.* **[43]** demonstrated the compatibility of microwave anneal with graphoepitaxy for cylinder- forming PS-*b*-PMMA in the presence of solvent. The microwave assisted directed self-assembly demonstrated here for both lamellar- and cylinder- forming PS-*b*-PMMA in the absence of solvent. The patterned substrates with 250 nm and 500 nm pitches were grafted with HO-PS-*r*-PMMA brush prior to BCP deposition and microwave annealed at 323 K for 60 s and related data are presented in **Figure 4.6**. It can be seen that the confinement topography induces excellent microphase segregation within the trenches irrespective of the channel width with lamella domains orientating perpendicular to the substrate surface, however, it lacks long-range alignment in both BC36 and BC74. It is evident from **Figure 4.6** that there is no preferential wetting of the sidewalls to either of the two blocks, PS and PMMA. The substrates were coated with HO-PS-*r*-PMMA before BCP deposition and the sidewalls being neutral wets the two blocks equally resulting in fingerprint type of patterns. The graphoepitaxy approach was also tried with the cylinder- forming BC67 under the same microwave anneal conditions. It can be seen from the results presented in **Figure 4.6** that perpendicular PMMA domain orientation with good confinement was achieved within the trenches even with 1.0 wt. % of the BCP solution unlike to planer substrate. However, the polymer overflows the trenches with 2.0 wt. % resulting in BCP patterns on the mesas.

The high χ factor enables PS-*b*-PDMS BCP to self-assemble with greater correlation length and as such the patterned substrates were pre-coated with PDMS-OH brush prior to BC45 deposition to direct self-assembly. Samples were microwave annealed at 323 K for 30 s based on the results demonstrated in **Figures**

4.3 and 4.4. The results of the PS-*b*-PDMS pattern after sequential CF_4 and O_2 etches is shown **Figure 4.6**. It can be seen from the images that the brush induced

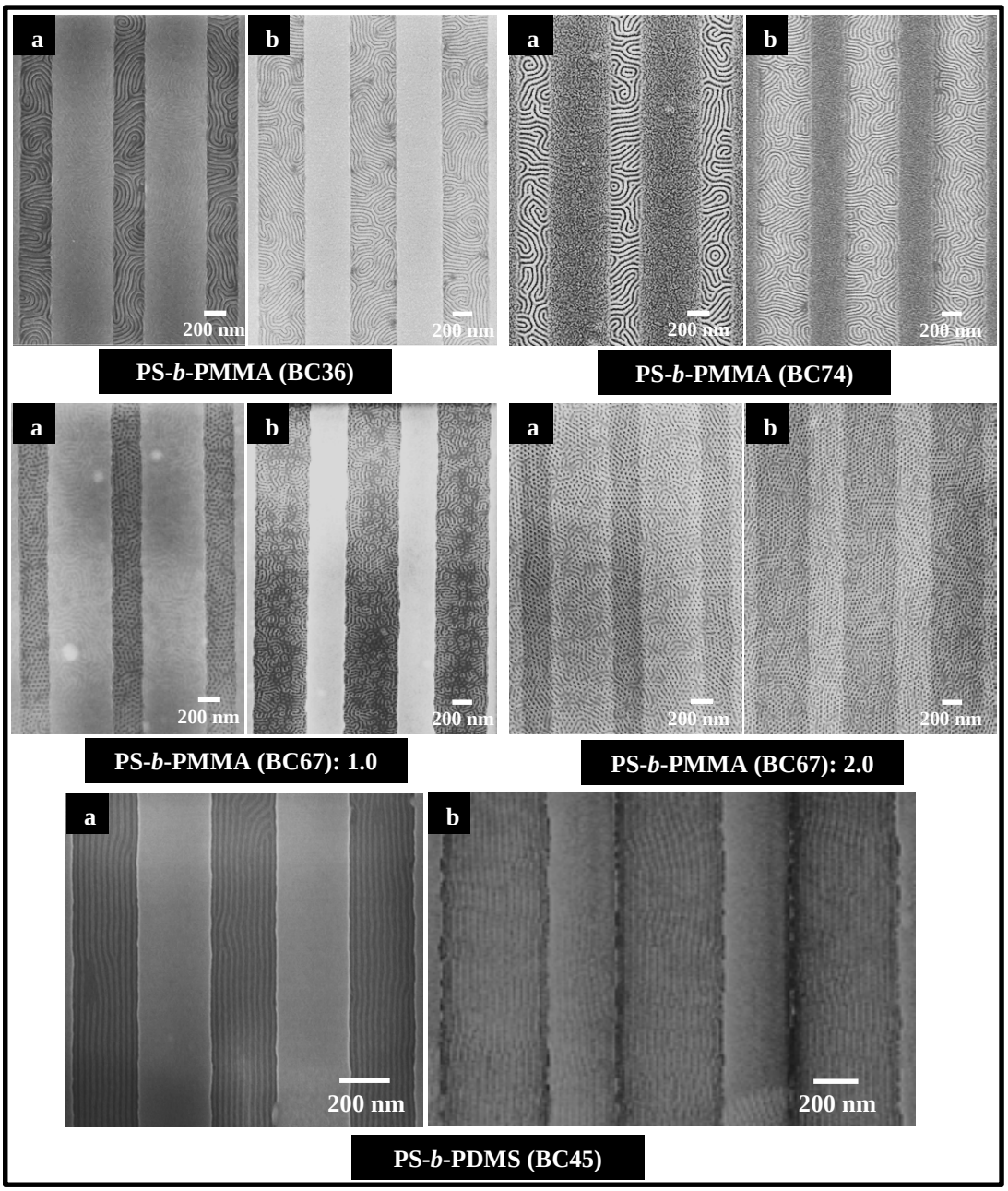

Figure 4.6. Top-down SEM images of PS-*b*-PMMA and PS-*b*-PDMS BCPs films after selective plasma removal of the PMMA component, and the top PDMS wetting layer and partial PS matrix for PS-*b*-PMMA and PS-*b*-PDMS, respectively, (light grey lines/matrix are PS/PDMS and darker lines/holes are voids created following PMMA/PS removal) on patterned silicon substrates with channel pitches of **(a)** 250 nm and **(b)** 500 nm. BCP films were microwave annealed at 323 K for 60 s for PS-*b*-PMMA and 30 s for PS-*b*-PDMS BCPs.

microphase segregation with graphoepitaxial alignment compatible with the pitches of the topographic patterns. Generally, for the hexagonal structure, preferred alignment should be achieved when the sidewalls preferentially interact with the majority block compared to the minor component. If the sidewalls are neutral and interact equally with both blocks (thus favouring the presence of both blocks at the sidewall), a disordered structure is formed. A good number of defects could be observed in the BCP patterns. However, this is not easy to quantify because a lot of defects observed arise from defects in the sidewall which cause local variations in the channel width. The results show that domain numbers can be controlled by carefully tuning the pitch period of the patterns.

4.4.7. Pattern transfer to form silicon nanostructures

Attempts were made to pattern transfer the nanopatterns formed to the substrate surface. This is important not only to demonstrate the usefulness of the methodology for application in microelectronic fabrication but also showing that the patterns observed are not simply surface features, but that the patterns observed are present through the depth of the film. Indicative results of successful pattern transfer are shown here for the PS-*b*-PMMA (BC36) and the PS-*b*-PDMS (BC45) systems. The SEM images shown in **Figure 4.7** of pattern transferred BC36 on both planar and patterned silicon substrates (note the microwave anneal is consistent with good filling of the channels as can be seen here) is following a silicon etch for 9 s that generates the best quality features based on previous studies **[11-13]**. The silicon substrate now consists of topographically patterned lines corresponding to the parent PS mask. The cross-section image in the inset of **Figure 4.7** provides a better view of the silicon features. The average silicon feature size and height measured from the SEM images is about 8.3 nm and 27 nm, respectively. This is because the etch process is not ideal in such narrow structures forming proportionally larger gaps between structures and more obviously non-rectangular feature cross-sections (aspect ratio).

The complex morphology PS-*b*-PDMS self-assembled patterns with a top and a bottom wetting PDMS layer makes pattern transfer to underlying silicon challenging as compared to the well-established polymer systems *e.g.*, PS-*b*-PMMA **[11-13]** and PS-*b*-PEO **[50]**. It should be noted that for an effective pattern transfer

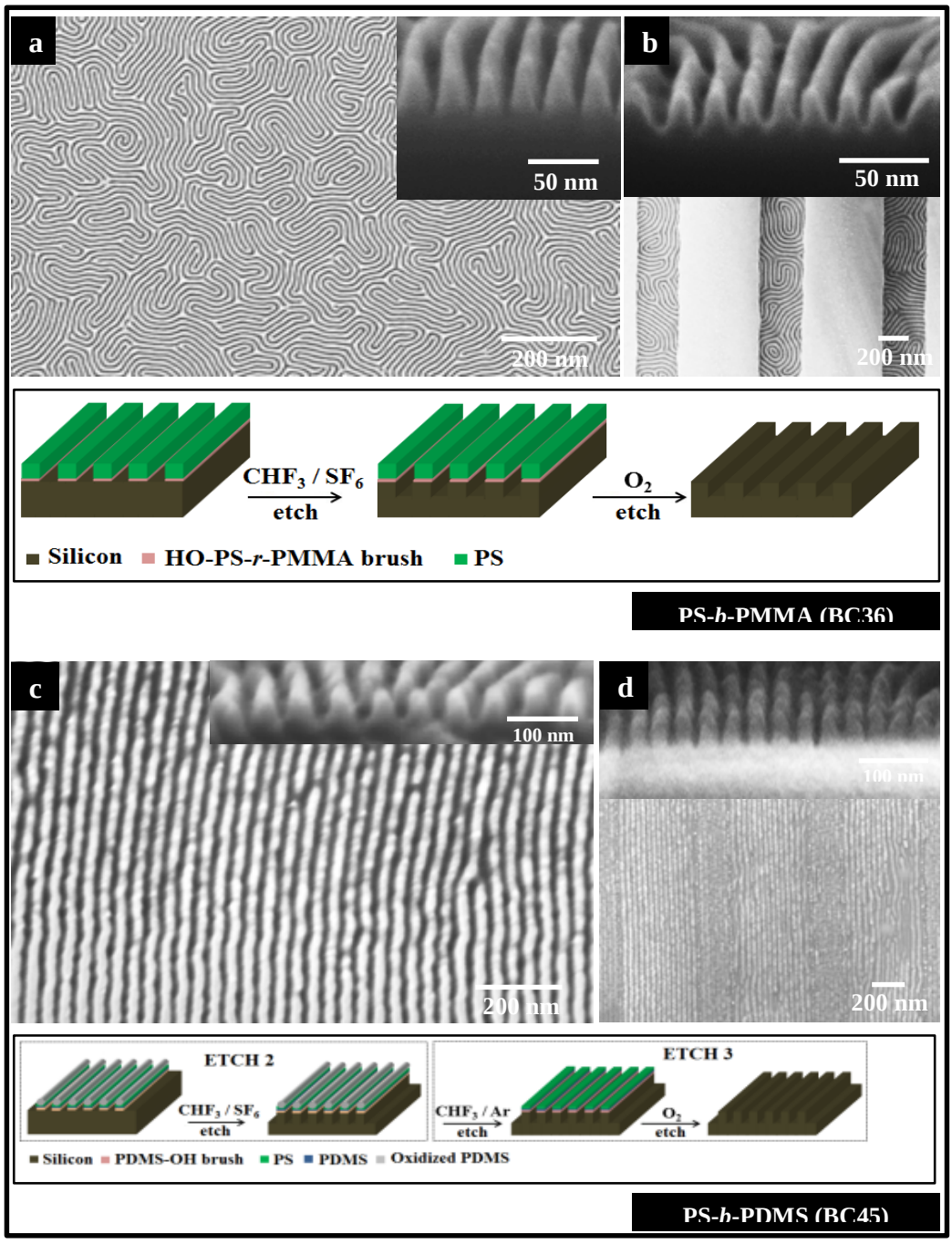

Figure 4.7. Top-down SEM images of PS soft mask template (fabricated from PS-*b*-PMMA (BC36)) patterns transferred to underlying **(a)** planer and **(b)** patterned silicon substrates (insets, **(a) and (b)** cross-section SEM images). SEM images of PDMS cylindrical patterns (fabricated from PS-*b*-PDMS (BC45)) transferred to underlying **(c)** planer and **(d)** patterned silicon substrates (insets, **(c) and (d)** cross-section SEM images). The schematics show the etching steps followed in the pattern transfer. See experimental section for details of pattern transfer in the two BCP systems.

process that the O_2 etch used in the initial etch has to be carefully optimized so that the cylinder structure is not undercut. However, if this is achieved, the oxidized, silica like cylinders can act as a hard mask for pattern transfer- an advantage with the BCP. The hard mask is unlikely to be affected by the etch recipe used to transfer the pattern into underlying silicon. **Figure 4.7** shows the top-down and cross-section SEM images of the silicon nanowires on planer and patterned silicon substrates obtained after the etches were used to remove the silica-like materials at the substrate surface and then to selectively remove silicon. The cross-section SEM image shows the nanowire line width of ~14.8 nm with a pattern depth of ~42 nm. The cross-section SEM images shown in **Figure 4.7** provide a more detailed image of the silicon nanowires fabricated in this way. Minor damage of the silicon features is apparent from **Figure 4.7**. The silicon features on the substrate are slightly narrower than the width of the initial oxidized PDMS cylinders due to partly isotropic etching. A reasonable aspect ratio of ~1.25 was obtained. A comparison of pattern transfer of BC36 and BC45 reveals the superior fidelity of the silicon features with PDMS hard mask. The results demonstrated here shows the compatibility of microwave anneal process for nanofabrication and holds promise to commercialization.

4.5. Conclusions

In this work, direct (*i.e.*, in the absence of a solvent) microwave assisted annealing has been shown to be effective in inducing controllable microphase separation in BCP thin films. The results are somewhat surprising since it is normally accepted that polymers are largely 'inert' to microwave radiation and will not increase significantly in temperature in conventional systems. Silicon substrates can be microwave heated but this is not a facile process and it is generally accepted that it is the intrinsic carriers not the dopant carriers that are responsible for heating **[51]**. Indeed, reports suggest that wafers with lower dopant levels heat more efficiently **[52]**. However, despite the range of substrates used, little dependence of the microphase separation was observed with substrate type; a result inconsistent with previous findings **[43]**.

In an effort to understand the data, the results of the non-conventional microwave annealing methodology reported in the present investigation are

compared with complimentary non-microwave, thermal annealing experiments under similar conditions of process temperature/time used in the microwave annealing experiments. The results are documented in the ***Appendix I*** (**Figures AI.3-AI6**) for clarity of presentation. The results from thermal annealing of the PS-*b*-PMMA BCPs under the low temperature/times used in a typical microwave process show little sign of regular microphase separation particularly with higher molecular weight systems. This is because the thermal experiments were performed well below the glass transition temperature of the PS-*b*-PMMA BCP. The PS-*b*-PDMS BCP system shows indications of microphase separation at higher anneal temperature and longer anneal time but with poor correlation length of the PDMS domains and with severe dewetting (**Figures AI.4-AI.6**) but compare very unfavourably to the data from microwave annealing of similar samples. These data suggest that microwave heating can bring about microphase separation at temperatures well below the glass transition temperature. However, indirect heating *via* the substrate might occur allowing the film temperature to be significantly greater than the instrument's set temperature. However, this seems less likely because of the range of substrates used. To confirm the passive role of the substrate, totally microwave inert substrates were investigated and it was seen that microphase separation could be achieved at fused silica substrates in similar microwave process conditions (similar experiments were also carried out on glass and quartz). Indicative data are presented in **Figure AI.7** and it is clear that the microphase separation behaviour of the two BCP systems are similar to the results obtained on bulk Si, SiO_2/bulk Si, Si/SiO_2/bulk Si and Si_3N_4/bulk Si substrates.

To understand the effect of substrate temperature during microwave anneal processes, temperature profiles from an independent sensor in the microwave chamber (**Scheme AI.1**) were recorded and representative examples are shown in **Figure AI.8**. The data presented in **Figure AI.8** show that the actual temperature remains very close to the set temperature in an annealing experiment suggesting that local heating effects at the surface were not important. To confirm this suggestion, we further measured the actual temperature of the substrates in the (BCP + substrate) system using an infrared thermometer. The measured substrate temperatures were only 3-5 degrees lower (within experimental error) than the set temperature in the

microwave experiment. These data clearly demonstrate that the substrate is in equilibrium with the set temperature of the microwave experiment. Thus it is evident that it's the microwave irradiation solely responsible for driving the self-organization in the BCP film.

This is a surprising result but it can be noted that microwave heating is a commonly used method in the synthesis of organic compounds **[53-55]**, application in inorganic chemistry **[56-59]** and is also used polymer chemistry particularly in polymer curing **[60]**. Microwave irradiation is a dielectric heating process where molecular rotation occurs in materials containing polar molecules having an electrical dipole moment, with the consequence that they will align themselves in an electromagnetic field. In an oscillating field such as in an electromagnetic wave, these molecules rotate continuously aligning with it a process known as dipole rotation, or dipolar polarization where the molecules reverse direction as the field alternates. Under the influence of electrical forces the rotating molecules impulse, twitch, and collide with other molecules, distributing the energy to adjacent molecules and atoms in the material and that energy appears as heat **[60-62]**. We suggest that although polystyrene is microwave transparent, the other blocks in the BCPs *viz*., polymethylmethacrylate and polydimethylsiloxane are polar **[63, 64]** and these polar molecules interact with the oscillating field resulting in dipole rotation and this rotation drives microphase separation. This may be through direct heating or *via* chain movements excited by the irradiating radiation.

In the set-up used here, it appears from the time dependence of the pattern (which degrades on extended heating time) that the BCP film effectively moves from initial disorder to ordered microphase separation through to a more disordered structure at the longest anneal periods. These observations suggest that the polymer molecules are becoming progressively more 'excited' initially allowing chain movement to form the ordered phase and then becoming so mobile that any order is lost.

In this way, the viability of the method for manufacture has been demonstrated. It has a number of advantages, notably in terms of process speed but it is also solventless and the use of large volume solvent annealing chambers is as yet unproven. The use of microwave annealing in silicon technology has been

established on large wafer sizes **[52]**. Solvent annealing on large wafers offers problems because solvent condensation can induce large area defects, etc **[31]**. Further, the possibility of impurity incorporation is reduced by avoidance of the solvent. The use in semiconductor manufacture has been demonstrated by exploring the use of topographically patterned substrates and the ability of the technique to be used in pattern transfer to the substrate. In this way, the technique represents significant promise for future development.

4.6. References

[1]. *International Technology Roadmap for Semiconductors*, 2007 edition (Emerging Research Materials); Semiconductor Industry Association: San Jose, CA, **2007**.

[2]. Harriott, L. Limits of Lithography. *Proc. IEEE* **2001**, *89*, 366-374.

[3]. Ito, T.; Okazaki, S. Pushing the Limits of Lithography. *Nature* **2000**, *406*, 1027-1031.

[4]. Broers, A. N. Resolution Limits for Electron-Beam Lithography. *IBM J. Res. Dev.* **1988**, *32*, 502-513.

[5]. Black, C. T. Polymer Self-assembly as a Novel Extension to Optical Lithography. *ACS Nano* **2007**, *1*, 147-150.

[6]. Thurn-Albrecht, T.; Schotter, J.; Kastle, G. A.; Emley, N.; Shibauchi, T.; Krusin Elbaum, L.; Guarini, K.; Black, C. T.; Tuominen, M. T.; Russell, T. P. Ultrahigh-Density Nanowire Arrays Grown in Self-assembled Diblock Copolymer Templates. *Science* **2000**, *290*, 2126-2129.

[7]. Thurn-Albrecht, T.; Steiner, R.; DeRouchey, J.; Stafford, C. M.; Huang, E.; Bal, M.; Tuominen, M.; Hawker, C. J.; Russell, T. P. Nanoscopic Templates from Oriented Block Copolymer Films. *Adv. Mater.* **2000**, *12*, 787.

[8]. Yang, S. Y.; Ryu, I.; Kim, H. Y.; Kim, J. K.; Jang, S. K.; Russell, T. P. Nanoporous Membranes with Ultrahigh Selectivity and Flux for the Filtration of Viruses. *Adv. Mater.* **2006**, *18*, 709.

[9]. Holden, G.; Legge, N. R.; Schroeder, H. E.; Quirk, R. P. *Thermoplastic Elastomers*, Hanser, New York, **1987**.

[10]. Hamley, I. W. *The Physics of Block Copolymers*, Oxford University Press, New York, **1998**.

[11]. Rasappa, S.; Borah, D.; Senthamaraikannan, R.; Faulkner, C. M.; Shaw, M. T.; Gleeson, P.; Holmes, J. D.; Morris, M. A. Block Copolymer Lithography: Feature Size Control and Extension by an Over-Etch Technique. *Thin Solid Films* **2012**, *522*, 318.

[12]. Farrell, R. A.; Kinahan, N. T.; Hansel, S.; Stuen, K. O.; Petkov, N.; Shaw, M. T.; West, L. E.; Djara, V.; Dunne, R. J.; Varona, O. G.; *et al*. Large-Scale Parallel Arrays of Silicon Nanowires *via* Block Copolymer Directed Self-assembly. *Nanoscale* **2012**, *4*, 3228.

[13]. Borah, D.; Shaw, M. T.; Rasappa, S.; Farrell, R. A.; O'Mahony, C.; Faulkner, C. M.; Bosea, M.; Gleeson, P.; Holmes, J. D.; Morris, M. A. Plasma Etch Technologies for the Development of Ultra-Small Feature Size Transistor Devices. *J. Phys. D: Appl. Phys*. **2011**, *44*, 174012.

[14]. Park, S. M.; Liang, X.; Harteneck, B. D.; Pick, T. E.; Hiroshiba, N.; Wu, Y.; Helms, B. A.; Olynick, D. L. Sub-10 nm Nanofabrication *via* Nanoimprint Directed Self-assembly of Block Copolymers. *ACS Nano* **2011**, *5*, 8523.

[15]. Jeong, S. J.; Kim, J. E.; Moon, H. S.; Kim, B. H.; Kim, S. M.; Kim, J. B.; Kim, S. O. Soft Graphoepitaxy of Block Copolymer Assembly with Disposable Photoresist Confinement. *Nano Lett.* **2009**, *9*, 2300.

[16]. Farrell, R. A.; Fitzgerald, T. G.; Borah, D.; Holmes, J. D.; Morris, M. A. Chemical Interactions and Their Role in the Microphase Separation of Block Copolymer Thin Films. *Int. J. Mol. Sci.* **2009**, *10*, 3671.

[17]. Bang, J.; Jeong, U.; Ryu, D. Y.; Russell, T. P.; Hawker, C. J. Block Copolymer Nanolithography: Translation of Molecular Level Control to Nanoscale Patterns. *Adv. Mater.* **2009**, *21*, 4769.

[18]. Chai, J.; Wang, D.; Fan, X.; Buriak, J. M. Assembly of Aligned Linear Metallic Patterns on Silicon. *Nat. Nanotechnol.* **2007**, *2*, 500.

[19]. Park, S. M.; Stoykovich, M. P.; Ruiz, R.; Zhang, Y.; Black, C. T.; Nealey, P. F. Directed Assembly of Lamellae- Forming Block Copolymers by Using Chemically and Topographically Patterned Substrates. *Adv. Mater.* **2007**, *19*, 607.

[20]. Ruiz, R.; Ruiz, N.; Zhang, Y.; Sandstrom, R. L.; Black, C. T. Local Defectivity Control of 2D Self-Assembled Block Copolymer Patterns. *Adv. Mater.* **2007**, *19*, 2157.

[21]. Xiao, S.; Yang, X. M.; Edwards, E. W.; La, Y. -H.; Nealey, P. F. Graphoepitaxy of Cylinder-Forming Block Copolymers for Use as Templates to Pattern Magnetic Metal Dot Arrays. *Nanotechnology* **2005**, *16*, S324.

[22]. Segalman, R. A.; Yokoyama, H.; Kramer, E. J. Graphoepitaxy of Spherical Domain Block Copolymer Films. *Adv. Mater.* **2001**, *13*, 1152.

[23]. Han, E.; Kang, H.; Liu, C. -C.; Nealey, P. F.; Gopalan, P. Graphoepitaxial Assembly of Symmetric Block Copolymers on Weakly Preferential Substrates. *Adv. Mater.* **2010**, *22*, 4325.

[24]. Ji, S.; Liu, C. -C.; Son, J. G.; Gotrik, K.; Gordon, S. W. C.; Gopalan, P.; Himpsel, F. J.; Char, K.; Nealey, P. F. Generalization of the Use of Random Copolymers to Control the Wetting Behavior of Block Copolymer Films. *Macromolecules* **2008**, *41*, 9098.

[25]. Han, E.; In, I.; Park, S. M.; La, Y. H.; Wang, Y.; Nealey, P. F.; Gopalan, P. Photopatternable Imaging Layers for Controlling Block Copolymer Microdomain Orientation. *Adv. Mater.* **2007**, *19*, 4448.

[26]. Ryu, D. Y.; Wang, J. Y.; Lavery, K. A.; Drockenmuller, E.; Satija, S. K.; Hawker, C. J.; Russell, T. P. Surface Modification with Cross-Linked Random Copolymers: Minimum Effective Thickness. *Macromolecules* **2007**, *40*, 4296.

[27]. In, I.; La, Y. H.; Park, S. M.; Nealey, P. F.; Gopalan, P. Side-Chain Grafted Random Copolymer Brushes as Neutral Surfaces for Controlling the Orientation of Block Copolymer Microdomains in Thin Films. *Langmuir* **2006**, *22*, 7855.

[28]. Ryu, D. Y.; Shin, K.; Drockenmuller, E.; Hawker, C. J.; Russell, T. P. A Generalized Approach to the Modification of Solid Surfaces. *Science* **2005**, *308*, 236.

[29]. Ludwigs, S.; Schmidt, K.; Stafford, C. M.; Amis, E. J.; Fasolka, M. J.; Karim, A.; Magerle, R.; Krausch, G. Combinatorial Mapping of the Phase Behavior of ABC Triblock Terpolymers in Thin Films: Experiments. *Macromolecules* **2005**, *38*, 1850.

[30]. Huang, E.; Russell, T. P.; Harrison, C.; Chaikin, P. M.; Register, R. A.; Hawker, C. J.; Mays, J. Using Surface Active Random Copolymers to Control the Domain Orientation in Diblock Copolymer Thin Films. *Macromolecules* **1998**, *31*, 7641.

[31]. Hobbs, R. G.; Farrell, R. A.; Bolger, C. T.; Kelly, R. A.; Morris, M. A.; Petkov, N.; Holmes, J. D. Selective Sidewall Wetting of Polymer Blocks in Hydrogen Silsesquioxane Directed Self-Assembly of PS-*b*-PDMS. *ACS Appl. Mater. Interfaces* **2012**, *4*, 4637.

[32]. Chang, J. -B.; Son, J. G.; Hannon, A. F.; Alexander-Katz, A.; Ross, C. A.; Berggren, K. K. Aligned Sub-10-nm Block Copolymer Patterns Templated by Post Arrays. *ACS Nano* **2012**, *6*, 2071.

[33]. Son, J. G.; Chang, J. -B.; Berggren, K. K.; Ross, C. A. Assembly of Sub-10-nm Block Copolymer Patterns with Mixed Morphology and Period Using Electron Irradiation and Solvent Annealing. *Nano Lett.* **2011**, *11*, 5079.

[34]. Voet, V. S. D.; Pick, T. E.; Park, S. -M.; Moritz, M.; Hammack, A. T.; Urban, J. J.; Ogletree, D. F.; Olynick, D. L.; Helms, B. A. Interface Segregating Fluoralkyl-Modified Polymers for High-Fidelity Block Copolymer Nanoimprint Lithography. *J. Am. Chem. Soc.* **2011**, *133*, 2812.

[35]. Jung, Y. S.; Chang, J. B.; Verploegen, E.; Berggren, K. K.; Ross, C. A. A Path to Ultranarrow Patterns Using Self-Assembled Lithography. *Nano Lett.* **2010**, *10*, 1000.

[36]. Jung, Y. S.; Lee, J. H.; Lee, J. Y.; Ross, C. A. Fabrication of Diverse Metallic Nanowire Arrays Based on Block Copolymer Self-Assembly. *Nano Lett.* **2010**, *10*, 3722.

[37]. Jung, Y. S.; Ross, C. A. Solvent-Vapor-Induced Tunability of Self-Assembled Block Copolymer Patterns. *Adv. Mater.* **2009**, *21*, 2540.

[38]. Bita, I.; Wang, J. K. W.; Jung, Y. S.; Ross, C. A.; Thomas, E. L.; Berggren, K. K. Graphoepitaxy of Self-Assembled Block Copolymers on Two-Dimensional Periodic Patterned Templates. *Science* **2008**, *321*, 939.

[39]. Jung, Y. S.; Jung, W.; Ross, C. A. Nanofabricated Concentric Ring Structures by Templated Self-Assembly of a Diblock Copolymer. *Nano Lett.* **2008**, *8*, 2975.

[40]. Ross, C. A.; Jung, Y. S.; Chuang, V. P.; Llievski, F.; Yang, J. K. W.; Bita, I.; Thomas, E. L.; Smith, H. I.; Berggren, K. K.; Vancso, G. J.; *et al*. Si-Containing Block Copolymers for Self-Assembled Nanolithography. *J. Vac. Sci. Technol. B* **2008**, *26*, 2489.

[41]. Jung, Y. S.; Ross, C. A. Orientation-Controlled Self-Assembled Nanolithography Using a Polystyrene-Polydimethylsiloxane Block Copolymer. *Nano Lett.* **2007**, *7*, 2046.

[42]. Zhang, X.; Murphy, J. N.; Wu, N. L. Y.; Harris, K. D.; Buriak, J. M. Rapid Assembly of Nanolines with Precisely Controlled Spacing from Binary Blends of Block Copolymers. *Macromolecules* **2011**, *44*, 9752.

[43]. Zhang, X.; Harris, K. D.; Wu, N. L. Y.; Murphy, J. N.; Buriak, J. M. Fast Assembly of Ordered Block Copolymer Nanostructures Through Microwave Annealing. *ACS Nano* **2010**, *4*, 7021.

[44]. Jeong, U.; Ryu, D. Y.; Kim, K. J.; Kim, D. H.; Russell, T. P.; Hawker, C. J. Volume Contractions Induced by Crosslinking: A Novel Route to Nanoporous Polymer Films. *Adv. Mater.* **2003**, *15*, 1247.

[45]. Kirk, C. T. Quantitative Analysis of the Effect of Disorder-Induced Mode Coupling on Infrared Absorption in Silica. *Physical Review B.* **1998**, *38*, 1255.

[46]. Zhang, X.; Douglas, J. F.; Jones, R. L. Influence of Film Casting Method on Block Copolymer Ordering in Thin Films. *Soft Matter* **2012**, *8*, 4980.

[47]. Ryu, D. Y.; Ham, S.; Kim, E.; Jeong, U.;Hawker, C. J.; Russell, T. P. Cylindrical Microdomain Orientation of PS-*b*-PMMA on the Balanced Interfacial Interactions: Composition Effect of Block Copolymers. *Macromolecules* **2009**, *42*, 4902.

[48]. Zhang, X.; Berry, B. C.; Yager, K. G.; Kim, S.; Jones, R. L.; Satija, S.; Pickel, D. L.; Douglas. J. F.; Karim, A. Surface Morphology Diagram for Cylinder-Forming Block Copolymer Thin Films. *ACS Nano* **2008**, *2*, 2331.

[49]. Xuan, Y.; Peng, J.; Cui, L.; Wang, H.; Li, B.; Han, Y. Morphology Development of Ultrathin Symmetric Diblock Copolymer Film *via* Solvent Vapor Treatment. *Macromolecules* **2004**, *37*, 7301.

[50]. Ghoshal, T.; Maity, T.; Godsell, J. F.; Roy, S.; Morris, M. A. Large Scale Monodisperse Hexagonal Arrays of Super Paramagnetic Iron Oxides Nanodots: A Facile Block Copolymer Inclusion Method. *Adv. Mater.* **2012**, *24*, 2390.

[51]. Kwong, D. -L. *Rapid Thermal and Other Short-Time Processing Technologies II: Proceedings of the International Symposium*, The Electrochemical Society, **2001**.

[52]. Zohm, H.; Kasper, E.; Mehringer, P.; Muller, G. A. Thermal Processing of Silicon Wafers with Microwave Co-Heating. *Microelectron. Eng.* **2000**, *54*, 247.

[53]. Larhed, M.; Olofsson, K. Microwave Methods in Organic Synthesis. Springer, Berlin, Germany, **2006**.

[54]. Kappe, C. O.; Stadler, A. Microwaves in Organic and Medicinal Chemistry. Wiley-VCH, Weinheim, Germany, **2005**.

[55]. Lidstrom, P.; Tierney, J. P. (Eds.). Microwave-Assisted Organic Synthesis. Blackwell Publishing, Oxford, UK, **2005**.

[56]. Chou, Y. -H.; Morgan, A. J.; Hondow, N. S.; Brydson, R.; Douthwaite, R. E. Microwave-Induced Plasma Heating and Synthesis: *In-situ* Temperature Measurement of Metal Oxides and Reactions to form Ternary Oxides. *Dalton Trans.* **2010**, *39*, 6062.

[57]. Douthwaite, R. E. Microwave-Induced Plasma-Promoted Materials Synthesis. *Dalton Trans.* **2007**, 1002.

[58]. Whittaker, A. G. Diffusion in Microwave-Heated Ceramics. *Chem. Mater.* **2005**, *17*, 3426.

[59]. Rao, K. J.; Vaidhyanathan, B.; Ganguli, M.; Ramakrishnan, P. A. Synthesis of Inorganic Solids Using Microwaves. *Chem. Mater*. **1999**, *11*, 882.

[60]. Galema, S. A. Microwave Chemistry. *Chem. Soc. Rev.* **1997**, *26*, 233.

[61]. Gabriel, C.; Gabriel, S.; Grant, E. H.; Halstead, B. S. J.; Mingos, D. M. P. Dielectric Parameters Relevant to Microwave Dielectric Heating. *Chem. Soc. Rev.* **1998**, *27*, 213.

[62]. Mingos, D. M. P.; Baghurst, D. R. Applications of Microwave Dielectric Heating Effects to Synthetic Problems in Chemistry. *Chem. Soc. Rev.* **1991**, *20*, 1.

[63]. Ando, H.; Yoshizaki, T.; Aoki, A.; Yamakawa, H. Mean-Square Electric Dipole Moment of Oligo- and Poly(methylmethacrylate)s in Dilute Solution. *Macromolecules* **1997**, *30*, 6199.

[64]. Konishi, T.; Yoshizaki, T.; Yamakawa, H. On the "Universal Constants" ρ and ϕ of Flexible Polymers. *Macromolecules* **1991**, *24*, 5614.

[65]. Mansky, P.; Liu, Y.; Huang, E.; Russell, T. P.; Hawker, C. Controlling Polymer-Surface Interactions with Random Copolymer Brushes. *Science* **1997**, *275*, 1458.

[66]. Mansky, P.; Russell, T. P.; Hawker, C. J.; Mays, J.; Cook, D. C.; Satija, S. K. Interfacial Segregation in Disordered Block Copolymers: Effect of Tunable Surface Potentials. *Phys. Rev. Lett.* **1997**, *79*, 237.

5.1 Abstract

A novel, simple and *in-situ* hard mask technology that can be used to develop high aspect ratio silicon (Si) nanopillars and nanowire features on a substrate surface is demonstrated. The technique combines a block copolymer inclusion method that generates nanodot arrays on substrate and an inductively coupled plasma (ICP) etch processing step to fabricate Si nanopillar and nanowire arrays. Iron oxide was found to be an excellent resistant mask over Si under the selected etching conditions. Features of very high aspect ratio can be created by this method. The nanopillars have uniform diameter and smooth sidewalls throughout their entire length. The diameter (15-27 nm) and length of the nanopillars can be tuned easily. Different spectroscopic and microscopic techniques were used to examine the morphology and size, surface composition and crystallinity of the resultant patterns. The methodology developed may have important technological applications and provide an inexpensive manufacturing route to nanodimensioned topographical patterns. The high aspect ratio of the features may have importance in the area of photonics and the photoluminescence properties are found to be similar to those of surface-oxidized Si nanocrystals and porous Si.

5.2. Introduction

Silicon (Si) and its one-dimensional (1-D) nanostructures has become essential for potential applications in integrated optoelectronic nanodevices **[1-3]**. Thus, the fabrication of vertically aligned iso-axial Si nanostructured arrays is becoming very important. However, accurate control over the axial crystallographic orientation of these nanostructures is necessary as it significantly influences their electronic structure (energy gap) as well as their physical properties (electronic transport) **[4, 5]**. This strict control of crystallography is required for the realization of advanced device technologies including electronic field emission, chemical sensing, field effect transistors, solar cells as well as biosensing **[6-9]**. Of particular relevance is the possibility of visible photoluminescence (PL) from porous Si because of applications as light sources as well as potential for development of novel flash memory **[10, 11]**. Of course, for many applications, it is not only crystallographic

control that is necessary but also the diameter, spacing and shape of the vertical nanostructures which need to be fabricated precisely over large areas with high throughput and low cost. Fabrication normally requires a UV-lithographic approach using a mask and etch process to fabricate the crystallographically aligned and dimension controlled Si nanostructures. E-beam lithography is usually used to realise the smallest feature size structures but is of prohibitive cost and low throughput **[12]**. As an alternative approach, self-assembly might have importance. The microphase separation of block copolymer (BCP) thin films can provide uniform densely spaced nanometer-scale features over wafer scale areas and is simple and cost-effective. The BCP nanopatterns can be integrated into a lithographic method by selective removal of one block and then using the remaining polymer as an etch mask for pattern transfer into the substrate **[13-16]**. However, the technique is limited for optical device application because the features generated tend to have low aspect ratio since the films generally have thicknesses around that of the BCP domain spacing and this results in poor etch selectivity and shape control **[17]**. The quality of the etch and the features formed greatly reduce the quality factor of the device **[18]**. To overcome this barrier, a 'hard mask' photoresist material with extremely high selectivity could be used. Dielectric materials (SiO_2, Al_2O_3 and Si_3N_4 etc.), various metal oxides and metals have been used as a etch masks **[19-22]**. Dielectric materials have much higher selectivity than conventional photoresists but require multi-step pattern transfer processes from the pre-fabricated pattern **[19]**. Metals (Cr, Ni), with high selectivity, are usually patterned by a lift-off technique but this can result significant distortion of the patterns and metal etching can present challenges **[20, 23]**. It is also highly undesirable for the hard masks to be a permanent part of a device structure. Hence to enable BCP lithographic methods for realisation of high aspect ratio features there is a strong requirement to develop a methodology where a hard mask approach can be integrated into the BCP process and provide a facile, inexpensive patterning process.

In this chapter we demonstrate a method to generate a patterned inorganic oxide hard mask material (iron oxide) *via* a simple and cost-effective diblock copolymer inclusion technique. The hard mask enables extremely high pattern

transfer fidelity into Si with a capability to produce structures orders of magnitude thicker than the original mask thickness. Using ICP dry etch techniques, the fabrication of the densely packed, size uniform, high aspect ratio Si nanopillar and nanowire arrays with good sidewall profiles can be shown. ICP etch methods are an advanced and sophisticated processes to provide highly anisotropic profiles with excellent control over selectivity to mask materials using low pressure plasmas which generates high density ion fluxes. Further, by independently controlling both the plasma density and the momentum imparted to the ions, significant improvements in control of the structures can be attained. We also show that the hard mask used can be easily removed with any significant pattern damage.

5.3. Materials and methods

5.3.1. Materials

Single crystal B doped P- type Si <100> wafers (thickness 650 μm, resistivity 6-14 ohm-cm) with a native oxide layer were used as a substrate. No attempt was taken to remove the native oxide layer. Polystyrene-*block*-poly(ethylene oxide) (PS-*b*-PEO) diblock copolymer was purchased from Polymer Source, Inc., Canada, and used without further purification (M_n, PS = 42.0 kg mol^{-1}, M_n, PEO = 11.5 kg mol^{-1}, M_w/M_n = 1.07, $\mathbf{M_n}$: number-average molecular weight, $\boldsymbol{M_w}$: weight-average molecular weight). Ethanol (99.5%, anhydrous), toluene (99.8%, anhydrous), oxalic acid dihydrate ($C_2H_2O_4$, $2H_2O$), iron (III) nitrate nonahydrate ($Fe(NO_3)_3$, $9H_2O$) were purchased from Sigma-Aldrich and used without further purification unless otherwise stated. De-ionized water was used wherever necessary.

5.3.2. BCP film preparation and solvent annealing

The wafers were cleaned by ultrasonication in acetone and toluene for 30 min each and dried under a nitrogen stream. PS-*b*-PEO was dissolved in toluene to yield 0.9 wt. % polymer solution at room temperature. The PS-*b*-PEO thin film was formed by spin coating the polymer solution (3000 rpm for 30 s). The film was exposed to toluene/water (50:50, v/v) mixed vapour placed at the bottom of a closed vessel kept at 323 K for 1 h under static vacuum oven (Townson and Mercer EV018).

5.3.3. Reconstruction of BCP film and hard mask fabrication

Following, the film was immersed in ethanol at 313 K for 15 h to obtain the activated film. Different concentrations of iron (III) nitrate nonahydrate ($Fe(NO_3)_3,9H_2O$) was dissolved in ethanol and spin-coated (3000 rpm for 30 s) onto the activated film. **[24, 25]**. UV/Ozone treatment was used to oxidize the precursor and remove polymer. The nanodots were further annealed at 1073 K for 1 h. These iron oxide nanodot arrays were used as a hard mask for pattern transfer onto the substrate.

5.3.4. Pattern transfer by plasma etching using hard mask

Pattern transfer was accomplished using an STS, Advanced Oxide Etch (AOE) ICP etcher. The system has two different RF generators, one, to generate and control the plasma density by direct connection to the antenna coil, while the other one was used to adjust and control the energy of ions by connecting it to the substrate holder. A double etching process was used to, firstly, etch the native silica layer and, secondly, the Si substrate. During etching, the sample is thermally bonded to a cooled chuck (283 K) with a pressure 9.5 Torr. For the oxide layer etch, the process parameters were optimised to a C_4F_8/H_2 gas mixture (21 sccm/30 sccm) using an ICP coil power of 800 W and a Reactive Ion Etching (RIE) power of 80 W. The silica etch time was kept constant (10 s) for all the samples. For Si pillar fabrication, the process used a controlled gas mixture of C_4F_8/SF_6 at flow rates of 90 sccm/30 sccm respectively and the ICP and RIE power were set to 600 W and 15 W respectively at a chamber pressure of 15 mTorr. The height of the Si pillars was varied by simply varying the Si etch time. For the removal of iron oxide nanodots, the substrate was immersed into 10.0 wt. % aqueous solution of oxalic acid dihydrate ($C_2H_2O_4$, $2H_2O$) for 2 h at room temperature, washed with water several times and dried.

5.3.5. Characterization of materials

5.3.5.1. Fourier Transform Infra-Red (FTIR) measurements

An IR 660, Varian infrared spectrometer was used to record the FTIR spectra. The measurements were performed in the spectral range of 4000-500 cm^{-1}, with a resolution of 4 cm^{-1} and data averaged over 32 scans.

5.3.5.2. X-ray Photoelectron Spectroscopy (XPS)

X-Ray photoelectron spectroscopy (XPS) experiments were conducted on a Thermo K-alpha machine with Al K_α X-ray source operating at 72 W.

5.3.5.3. Scanning Electron Microscopy (SEM)

Top-down and cross-sectional scanning electron microscope (SEM) images were obtained by a high resolution (< 1 nm) Field Emission Zeiss Ultra Plus-SEM with a Gemini® column, FEI Company and FEG Quanta 6700 at an accelerating voltage of 5 kV.

5.3.5.4. Focused Ion Beam (FIB)

An FEI Strata 235-Focused Ion Beam (FIB) tool was used to generate FIB lamellae cross-sections. E-beam produced platinum was deposited at the substrate followed by the ion-beam deposited platinum. Milling and polishing of the samples were carried out at the lower aperture size and the specimen was imaged under the higher resolution Zeiss Ultra Plus-SEM.

5.3.5.5. Transmission Electron Microscopy (TEM)

Samples were prepared for TEM cross sectional imaging with Zeiss Auriga - Focused Ion Beam (FIB) dual beam system were further imaged by transmission electron microscopy (TEM, FEI Titan) operating at an accelerating voltage of 130 keV.

5.3.5.6. Photo Luminescence (PL) spectroscopy

The photoluminescence measurements were carried out at room temperature with a fluorescence spectrophotometer (Perkin-Elmer LS 50 B).

5.3.5.7. Raman spectroscopy

Raman spectra were recorded using a SPEX 1403 monochromator equipped with a dc detection device. The 488 nm laser line of an Ar ion laser was used for excitation with an output power of 20 mW.

5.4. Results and discussion

5.4.1. Fabrication of silicon nanopillar arrays

The methodology of preparing ordered arrays of iron oxide nanodots was based on formation of a microphase separated PS-*b*-PEO thin films by solvent annealing **[26]**. This provides a nanopattern consisting of hexagonally arranged, vertically oriented (to the surface plane) of PEO cylinders in PS matrix. The marked chemical difference between PS and PEO allows the selective inclusion of metal ions into the PEO block and avoids any component removal. Prior to the inclusion of the inorganic component, the PEO blocks were 'activated' by ethanol which accelerates the inclusion of metal cations or colloidal entities into the cylinders probably via either intra- or intermolecular coordination through electron donation from the PEO block oxygen atoms. UV/ozone treatment was used to convert the polymer-inorganic component combination into a rigid oxide pattern and is effective because of its' ability in converting non-volatile inorganic compounds into oxides whilst removing organic components. The as prepared iron oxide (Fe_3O_4) nanodots have uniform size and shape and their placement mimics the original self-assembled block copolymer pattern. The nanodots have good thermal stability and strong adherence to the substrate surface but the annealing at 1073 K causes the transformation of the phase to Fe_2O_3.

Scheme 5.1 illustrates the process flow diagram of the fabrication of ordered aligned Si nanopillars by pattern transfer into Si substrate using iron oxide nanodots as a hard mask. **Scheme 5.1(A)** shows the formation of a hexagonal array of iron oxide nanodots on the substrate prepared by block copolymer inclusion technique

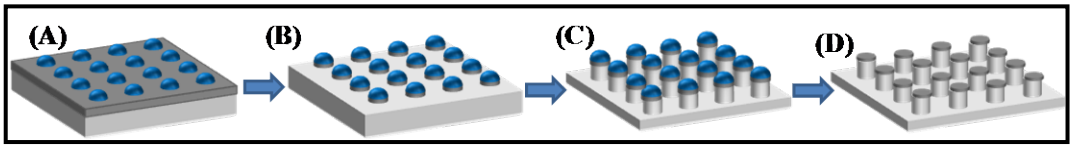

Scheme 5.1. Schematic diagram of the fabrication of Si nanopillar arrays: **(A)** hexagonal ordered iron oxide nanodots on Si substrate with a native oxide layer, **(B)** nanodots after SiO_2 etch, **(C)** nanopillars formed after Si etch and **(D)** Si nanopillars with a native oxide at top after removal of iron oxide.

as described above. A rapid silica etch process is followed to remove the exposed native silica layer on top of the substrate whereas the oxide layer underneath iron

oxide nanodots (mask) remained unaffected (**Scheme 5.1(B)**). The pattern transfer process is pursued by the Si etch process during which the substrate area directly below the mask is protected from the etch gases and only the exposed Si is removed. This process results in the formation of the Si nanopillars with a layer of native oxide and iron oxide at their uppermost surface as illustrated in **Scheme 5.1(C)**. The Si nanopillars with same structural arrangement and lateral dimension are obtained after removal of iron oxide nanodots (**Scheme 5.1(D)**).

Figure 5.1(a) shows dense (4.2 x 10^{10} cm^{-2}) hexagonally ordered iron oxide (Fe_2O_3) nanodots on the substrate prepared by the BCP inclusion technique. The nanodots are well adhered to the substrate after annealing at 1073 K for 1 h, with a diameter 21 nm, height 7 nm and the centre to centre nanodot spacing 42 nm. Pattern transfer via silica and Si etches created Si nanopillar arrays with Fe_2O_3 nanodots at top of the pillars. The top-down SEM image (**Figure 5.1(b)**) demonstrates a densely

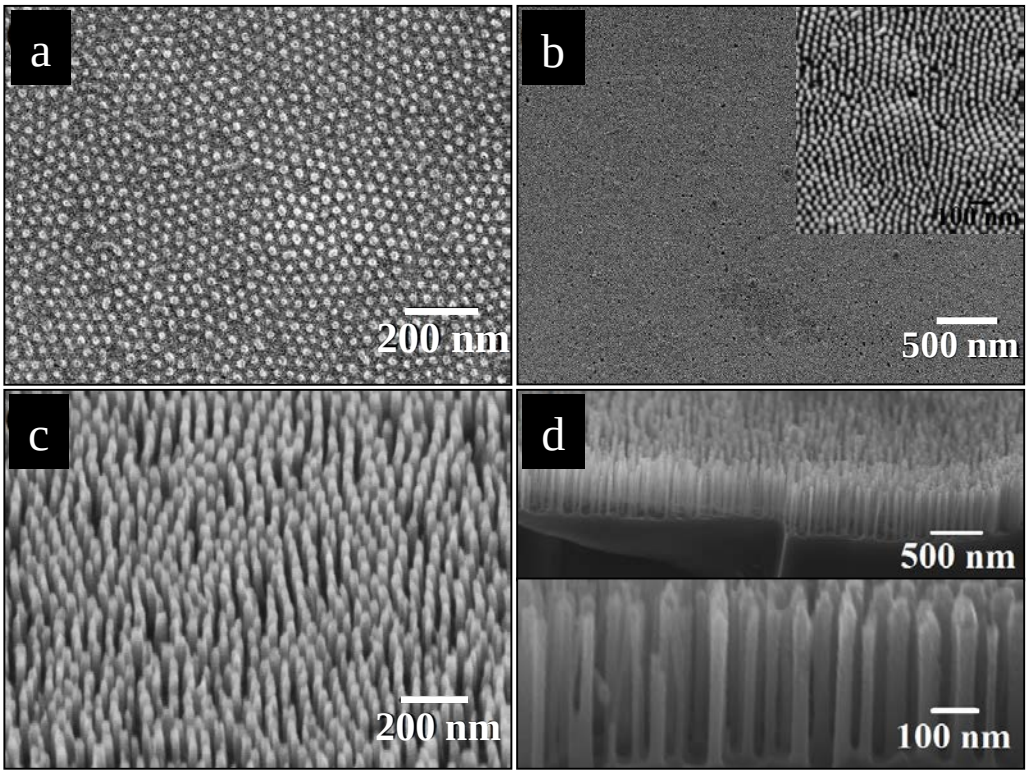

Figure 5.1. SEM images of **(a)** hexagonal ordered iron oxide nanodots on Si substrate, **(b)** nanopillar arrays with iron oxide nanodots at top formed after pattern transfer onto Si, **(c)** Si nanopillars after removal of mask and **(d)** cross-sectional

image of 500 nm long Si nanopillars. Insets of **(b)** and **(d)** shows corresponding higher magnification SEM images revealing the hexagonal arrangement.

packed, uniform, ordered arrangement over large areas after the pattern transfer. The significant contrast enhancement (compared to **Figure 5.1(a)**) suggests pattern transfer has occurred. The high resolution SEM image in the inset of **Figure 5.1(b**) also reveals the hexagonal ordered pillars have an average diameter of 21 nm at a spacing of 42 nm. This implies that the etching does not damage the original pattern to any extent. A mild oxalic acid aqueous solution was used to remove the undesired Fe_2O_3 mask from the top of Si nanopillar arrays. **Figure 5.1(c)** shows the structures are unaltered by the oxide removal and show only Si structures with a native silica layer at their upper surface. The average height of the Si nanopillars is around 500 nm (measured from the cross-sectional SEM image shown in **Figure 5.1(d)**) for a 10 min Si etch time. The higher magnification image in **Figure 5.1(d)** (bottom) shows the pillars of uniform diameter along their length and no shadowing effect of mask is observed. Further, smooth sidewalls are observed.

5.4.2. FTIR characterization of hard mask materials

Figure 5.2(a) shows FTIR absorption spectra of the etched sample before (I) and after (II) iron oxide removal to reveal the composition of the Si nanopillars on Si substrate. Two major features centred at 678 cm^{-1} and 1070 cm^{-1} are detected for both the samples. The band centred at 678 cm^{-1} can be assigned to neutral charged oxygen vacancies possibly non-bridging oxygen hole centers (NBOHCs) or similar compounds in β-cristobalite, a silica polymorph **[27]**. It has also been reported that the peaks between 660─690 cm^{-1} are an indicative of high density Si-Si bonds **[28]**. Since the peak is present for both the samples and silica is a minor component in these samples, the second assignment is much more likely and suggests that the major component is Si for both the samples and that the pillars are largely Si in nature as will be confirmed below. The feature at 1070 cm^{-1} is associated with stretching vibration modes of the Si-O-Si bonds in SiO_2 **[29]**. For clarity, the insets shows corresponding magnified spectra in the range between 1000-1300 cm^{-1}. As these peaks do not undergo any important changes, it can be argued that no

restructuration occurs during iron oxide removal process. An additional strong peak at 540 cm^{-1} is observed for the etched sample (**Figure 5.2(a(I))**) and corresponds to the most intense peak for hematite **[30]**. This peak disappeared after oxalic acid treatment (**Figure 5.2(a(II))**) and so confirms removal of the iron oxide nanodot component. The spectra also showed bands centred at 1170 cm^{-1} and 1235 cm^{-1} are assigned to C-F stretching vibrations **[31]**. The band at 1235 cm^{-1} corresponds to a C-F stretching vibration where covalent bonding predominates **[32]**. These peaks are typical of substrates etched with fluorine containing gases **[33]**.

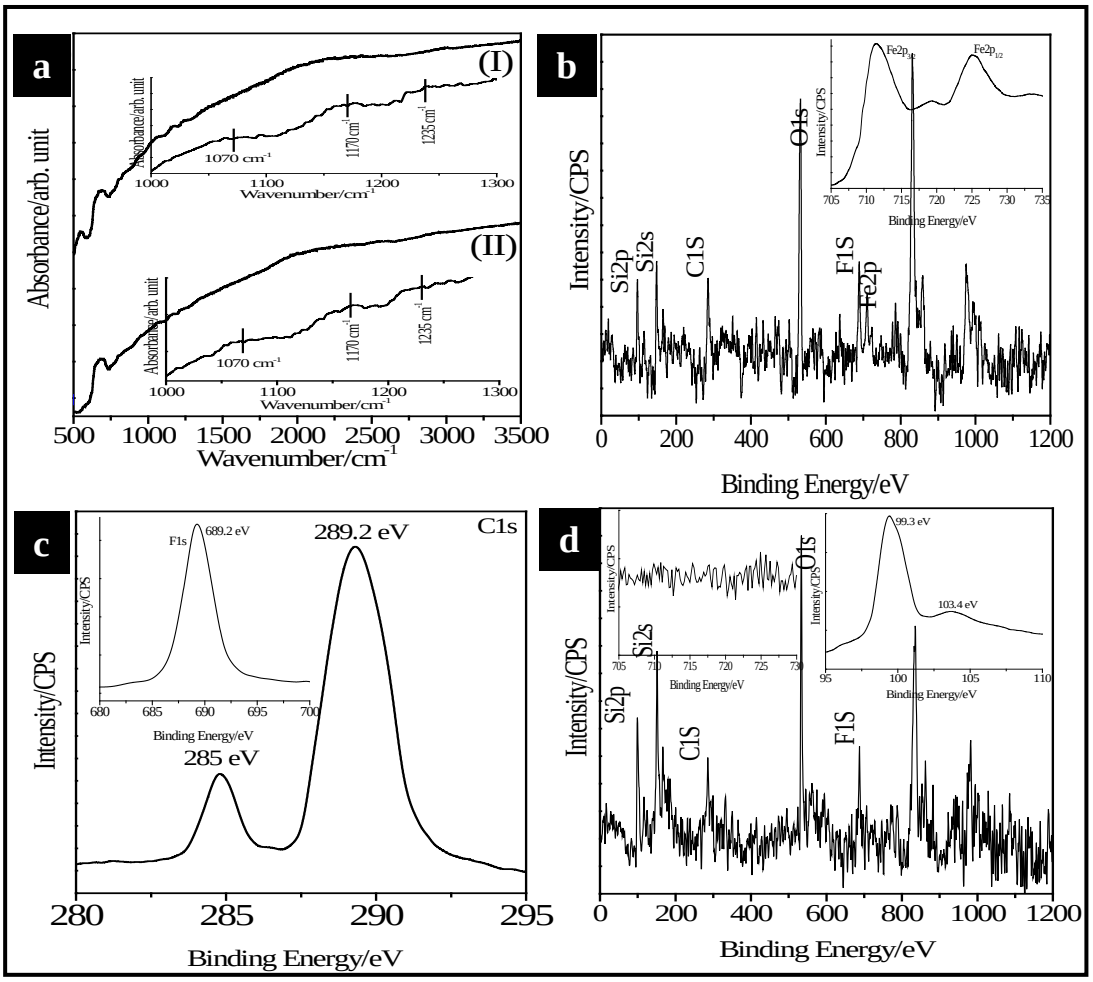

Figure 5.2. (a) FTIR absorption spectra of the etched sample before **(I)** and after **(II)** iron oxide removal. Insets shows corresponding spectra in 100-1300 cm^{-1} range. XPS survey spectra of the nanopillars on Si substrate **(b)** before and **(d)** after removal of iron oxide. Insets of **(b)** and **(d)** shows corresponding high resolution Fe2p spectra. **(c)** and inset shows high resolution C1s and F1s spectra. Inset of **(d) (right)** illustrates Si 2p spectrum.

5.4.3. XPS characterization of hard mask materials

In order to quantify the surface composition, XPS analyses were performed on the etched samples before and after iron oxide removal process. **Figure 5.2(b)** shows typical XPS survey spectrum of the sample after 3 min Si etch and confirms the presence of Si, C, O, F and Fe. The Si, O and Fe features originate from the Si nanopillars, the native oxide layer and iron oxide nanodots at the top of the pillars respectively. However, the intensity of C1s feature is significantly greater than might be expected from adventitious contamination during sample preparation etc. It is likely that the F1s peak is formed during the etch process (as there was no sign of fluorine before etching). To investigate further, additional high resolution C1s, F1s and Fe2p spectra were recorded. Fe 2p core level spectrum (inset of **Figure 5.2(b)**) consists of two sharp peaks associated with Fe $2p_{3/2}$ and Fe $2p_{1/2}$ at 711.3 and 725.1 eV accompanied by high binding energy satellite structures (+8 eV shift). The absence of a feature at 714.5 eV implies that metal fluoride (FeF_3) is not produced during the etch process **[34]**. These data are consistent with the existence of Fe^{+3} (Fe_2O_3) ions only **[35]**. The C1s spectrum shown in **Figure 5.2(c)** exhibits two major components at 285 eV and 289.2 eV. The peak at 285 eV is assigned to adventitious carbon and the other peak is attributed to the carbon atoms covalently bonded to the fluorine atoms (C-F bond) **[36]**. The F1s XPS spectrum (inset of **Figure 5.2(c)**) exhibits a sharp peak at 689.3 eV corresponds to fluorinated carbon atoms (C-F) **[36]**. The absence of a metal fluoride peak (around 685 eV) again confirms only the Fe_2O_3 phase is present in the sample **[34]**. These results suggest the generation of perfluorinated C-F (CF_2 or CF_3) during the etch process. **Figure 5.2(d)** shows the survey spectrum of the etched sample after iron oxide removal clearly implies effective removal of iron oxide. All other peaks remain unaffected and suggest that the oxalic acid solution has little or no effect on the structure. The intensity of the Si features increases as the iron is removed as might be expected. The high resolution Si 2p spectrum (inset of **Figure 5.2(d)**) provides information

about nature of the Si and its compounds. The spectrum consists of one strong peak at 99.3 eV corresponding to zero-valent Si and another weak peak at 103.4 eV assigned to the Si oxide phase close to silica. Hence, the XPS results confirm the presence of Si nanopillars on the substrate with a native oxide layer at top.

5.4.4. Cross-section SEM characterization of nanopillars

The diameters and heights of the resultant patterns can be varied by changing the diameter of the oxide mask and the Si etch time respectively without altering

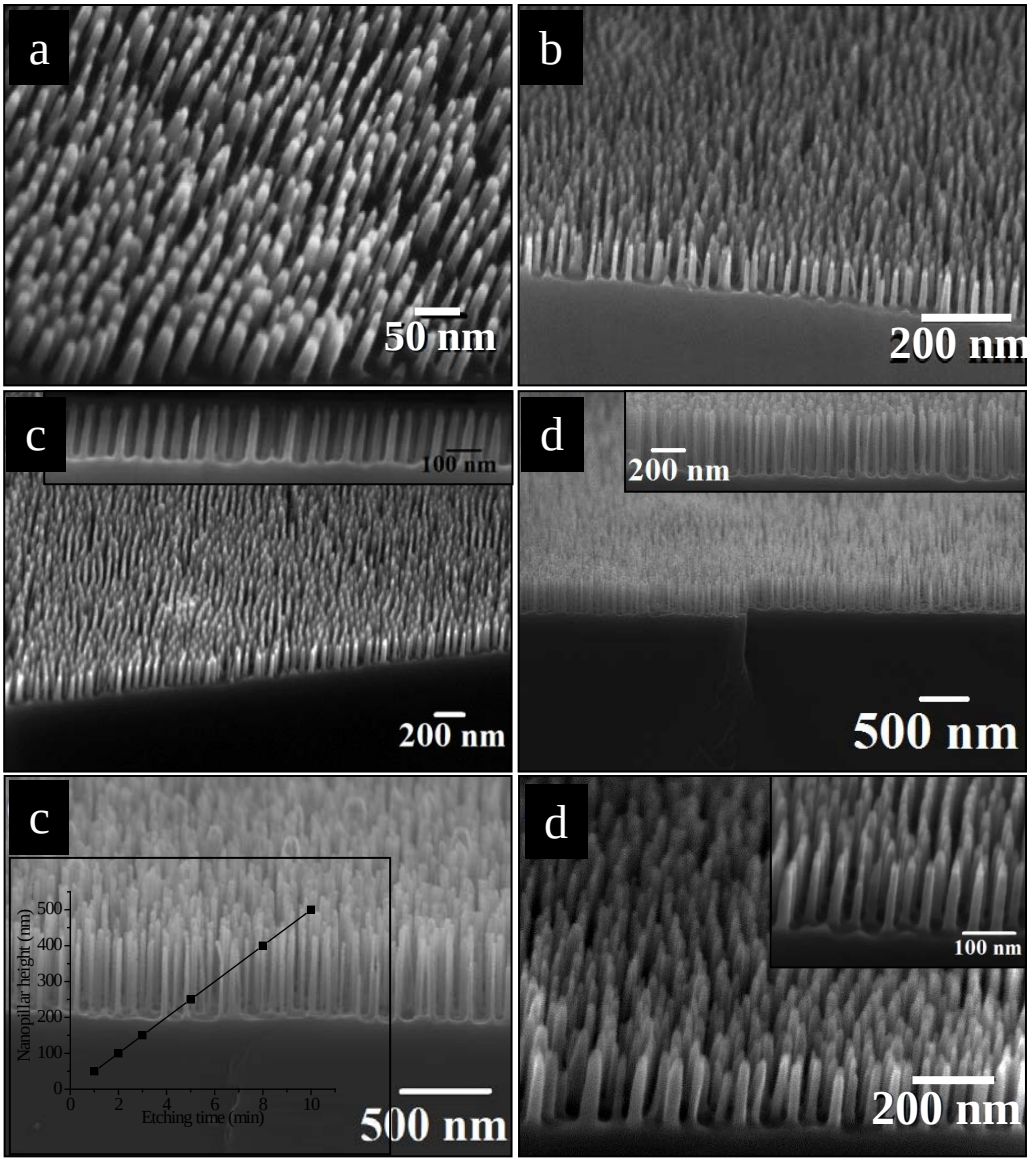

Figure 5.3. Cross sectional SEM images of Si nanopillars with different diameter and height **(a)** 21 nm, 50 nm, **(b)** 21 nm, 100 nm, **(c)** 21 nm, 150 nm, **(d)** 21nm, 400 nm, **(e)** 21 nm, 500 nm, **(f)** 27 nm, 150 nm and **(f, inset)** 15 nm, 150 nm respectively.

Inset of **(c, d)** shows oriented Si nanopillars with 42 nm spacing between them. Inset of **(e)** shows the variation of nanopillar height with etching time.

other processing conditions. At the longer etch times, well defined nanowire arrays can be formed. **Figures 5.3(a) to 5.3(e)** shows the cross-sectional SEM images of the hexagonal patterned uniform Si nanopillars (or nanowires) with vertical smooth sidewalls of average heights about 50 nm, 100 nm, 150 nm, 400 nm and 500 nm for 1 min, 2 min, 3 min, 8 min and 10 min Si etch periods respectively. All the images demonstrate good coverage of the nanopillar/nanowire arrays over a large area. The diameters of the nanopillars are almost equal throughout its entire length, no narrowing or broadening effects are observed. The images reveal quite narrow distribution of the aspect ratio of the pillars. The higher magnification images shown in the inset of **Figure 5.3(c)** and **5.3(d)** exhibits vertical rows of Si pillars of height 150 nm and 400 nm for 3 min and 8 min Si etch times. The variation of average nanopillar height with the Si etch time is shown in the inset of **Figure 5.3(e)**. The nanopillars height increases linearly with etch time at a constant rate 50 nm min^{-1}. Different iron oxide nanodot diameters (by changing the concentrations of the iron precursor **[24]**) are employed produce Si nanopillars with different diameters. A large area SEM image (**Figure 5.3(f)**) shows the ordered arrangement of the pillars of average diameter 27 nm and height 150 nm. Hexagonal featured aligned Si pillars of average diameter 15 nm can be accomplished with 3 min etch time (inset of **Figure 5.3(f)**). From the SEM images, a very narrow distribution of the iron oxide nanodot diameters was observed and this, in turn, produces nanopillars of uniform diameter over the entire sample area. The diameters of the nanodots can only be varied over a narrow size range of 15-27 nm for the particular PS-*b*-PEO BCP used here, but it should be noted that the diameters as well as the spacing between the nanodots can be altered by use of BCPs of different molecular weight. It is noted that different concentrations of the iron precursor solution altered the nanodot diameter as well as the thickness of the resultant nanodots (which is clearly an important parameter in the pattern transfer process). As the precursor solution prepared typically consists of a large volume fraction of ethanol, the free volume of the PEO activated cylinders is predominantly filled by ethanol, thus, the quantity of the

inorganic component within the PEO cylinders depends on the concentration of the precursor used. In this way, the diameter and thickness of the nanodots are directly proportional to the precursor concentration to a certain extent. Thus, different aspects ratio nanopillars can be realized either by changing the diameter of the mask or by varying the etch time. No surface roughening or pattern damage is seen with decreasing the diameter or increasing the height of the pillars.

5.4.5. TEM characterization of silicon nanopillars

Figure 5.4(a) and **Figure 5.4(b)** shows the cross sectional TEM images of the array of etched (60 s) nanopillars fabricated on (100) Si substrates, before and after iron oxide removal respectively. The images reveals ordered arrays of Si nanopillars of about 50 nm long with the expected 42 nm centre-to-centre spacing between them. **Figure 5.4(a)** clearly shows the iron oxide nanodots with distinct contrast difference

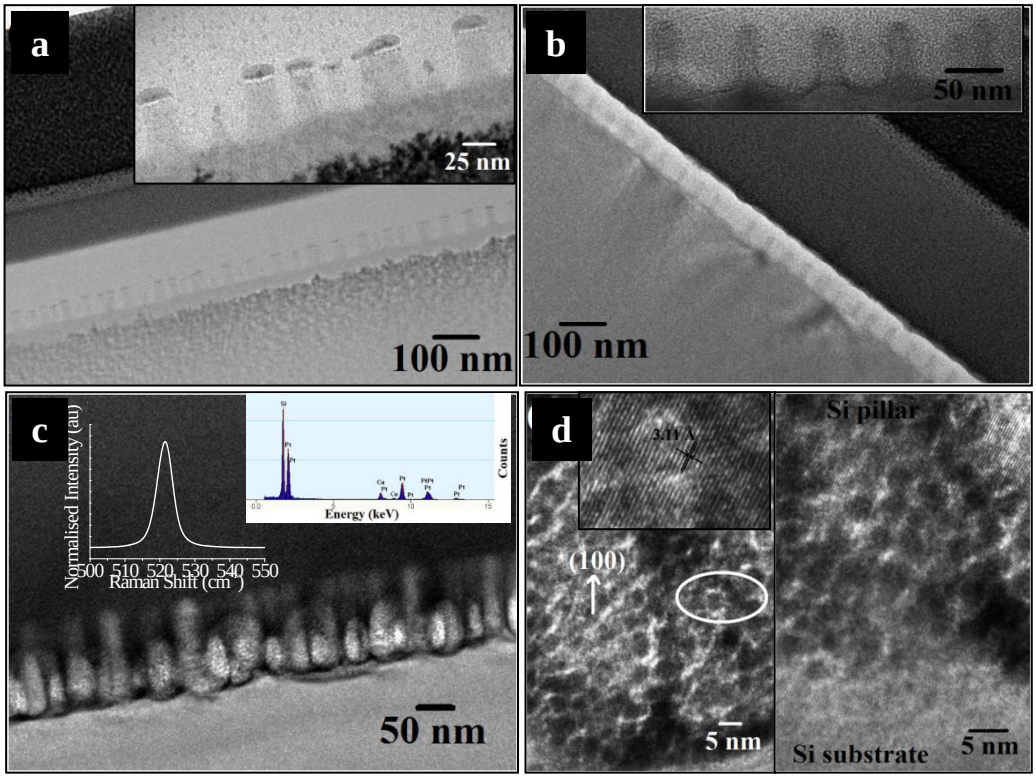

Figure 5.4. Large area view of FIB thinned TEM cross sectional image of nanopillars on Si substrate **(a)** before and **(b)** after iron oxide removal process. Corresponding insets shows higher magnification TEM image, clearly depicts the presence and absence of iron oxide nanodots respectively. **(c)** TEM images of 150 nm long Si nanopillars arrays. Inset of **(c) (right)** EDAX spectrum along the length of a nanopillar. **(d)** HRTEM image shows continuous fringes across the junction of the nanopillar and Si substrate, Pt nanoparticles also noticeable deposited during

preparation of FIB thinned sample. Inset of **(c) (left)** shows the Raman spectrum of Si nanopillar arrays on Si substrate.

at the top of the pillars. These features are completely removed after the acid removal process (**Figure 5.4(b)**). The higher magnification TEM image shown in the inset of **Figure 5.4(a)** reveals the layered arrangement of Si, silicon oxide, iron oxide at the top of the nanopillars. All the pillars were found to maintain a rectangular profile with smooth sidewalls and there is almost no diameter variation along the length. Note that the nanopillars are not damaged during the oxide removal process and their original profiles and arrangement are unchanged (**Figure 5.4(b)**). Direct high resolution TEM imaging of the pillars following FIB thinning was not possible because of silica deposition during the FIB treatment. In order to reveal the crystalline structure of the Si nanopillars after the oxide removal process, Pt was directly deposited onto the nanopillars and samples FIB thinned. **Figure 5.4(c)** shows identical ordered arrays (front and back rows) of Si nanopillars after iron oxide removal. The EDAX spectrum obtained along the length of the nanopillars reveals the presence of Si, Cu and Pt (inset of **Figure 5.4(c)**). The absence of Fe again proves the effective removal of the iron oxide. In the HRTEM image, ordered atomic planes i.e single crystalline structure can be observed on two of the nanopillars shown in **Figure 5.4(d) (left)**. The higher resolution image of the marked area shows the lattice fringes with a spacing 3.12 Å across the pillars agrees reasonably well with cubic fcc structure of Si (111) lattices planes **[37]**. The nanopillars were axially oriented at angle 54^{o} with the (111) lattice planes and is consistent with a (100) growth direction i.e. identical to the orientation of the initial Si wafer. Thus, highly dense uniform 1-D Si nanopillar arrays with controlled crystallographic orientation could be created through selective etching of the Si wafers of chosen orientations. TEM also reveals a very thin amorphous layer at the surfaces of the nanopillars and this might be either a native oxide or residual C-F polymer formed by etching. **Figure 5.4(d) (right)** shows the continuous clear lattice fringes across the junction between Si wafer and the nanopillar indicates the absence of defects or stacking faults formed during etching.

The crystalline property of the Si nanopillars on Si substrate was further examined by Raman spectroscopy. The Raman spectrum obtained is nearly Lorentzian in shape and an intense peak is observed at 520 cm^{-1} and can be readily assigned to the first order transverse optical phonon mode of crystalline Si (inset of **Figure 5.4(c)**). This peak observed is in the centre of the Brillouin zone which is due to the conservation of quasi-momentum in crystals. The absence of other peak in Raman spectra confirms that the nanopillars retain the crystallinity of bulk Si wafer.

5.4.6. Photoluminescence measurements

Photoluminescence (PL) measurements were performed on the ordered arrays of Si nanopillars on the Si substrate aged for 10 days in ambient air. For the measurement, all the samples were immersed in oxalic acid solution (to remove the hard mask iron oxide nanodots), dried and placed at ambient air. The PL spectra of all the samples are almost similar, no apparent band shift or intensity difference was observed. **Figure 5.5** shows the PL spectrum of the Si nanopillars created after 3 min Si etch on Si wafer at room temperature. The PL band is intense with a

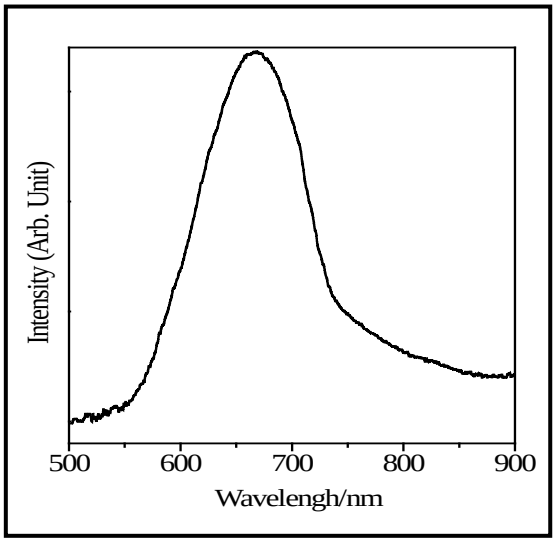

Figure 5.5. PL spectrum of Si nanopillar arrays on Si substrate.

Gaussian-like characteristics centred at 666 nm (~1.86 eV) under a 325 nm excitation wavelength. The same PL spectral region has been reported in literature

for different Si/SiO_2 based structures **[38-41]**. This band position is typical for NBOHC in bulk silica **[42]**. Note that the NBOHC model of light emitters has also been suggested to explain visible PL from porous Si **[43]** and Qin et al **[44, 45]**. explained the visible emission from native oxide on Si wafers which originates from luminescent centres exist in the silica skins of nano-Si particles. As the pillars fabricated here are exposed to ambient air, there is always a native oxide that layer exists on top as well as sidewalls of the Si nanopillars. It is, therefore, suggested that the PL band from the Si nanopillar arrays is associated with the native oxide exist at the top/sidewall of the pillars. Further, it is suggested that the luminescent centres originate from the oxygen deficient defects in the $Si\text{-}SiO_2$ interface region. It is noted that the PL intensity will be dependent on the aging time (i.e. oxide thickness) and also with the increase of height of the Si nanopillars.

5.4.7. Etch chemistry

The methodology used here was centered around a pattern transfer technique using an '*insitu*' iron oxide hard mask process combined with a carefully tuned plasma etc. It is worthwhile discussing the etch chemistry in some detail. In order to provide the structural control of features needed, ICP power and DC bias were set to low-to-moderate levels to avoid heating of the samples, while gas flow rates were chosen to provide short gas residence times and hence an ample supply of etch species. The thin layer of silicon dioxide was etched using a combination of C_4F_8/H_2 gases. C_4F_8 exhibited highest silica etch rate among a series of fluorocarbon gases used but pure C_4F_8 gas flows showed poor etch selectivity presumably because of high concentrations of F atoms/radicals formed in the plasma **[46]**. The addition of hydrogen reduces the silica etch rate due to reduction of reactive species by simple dilution and also by the formation of HF. This also helps in the formation of CF_x ($x \leq 2$) radicals which increases the etch selectivity conformity through the formation of carbon-fluoro polymers at the sidewall **[33]**. Fluorine gas chemistry was used to etch the Si substrate. To avoid sidewall corrugation or scalloping, a sequential etch/deposition process was used. The chopping Bosch Si etch technique **[47]** is utilized which can be realized by sulphur hexafluoride, SF_6, as the etching gas and octafluorocyclobutane, C_4F_8, as the passivation gas. During the etching step, SF_6

was injected into the chamber from which atomic fluorine can be generated by different collision processes in the plasma. These ions are driven down to the substrate by the electric field derived from the potential between the plasma and the substrate. Atomic fluorine is an aggressive radical that reacts with unmasked Si through the reaction:

$$Si + 4F \rightarrow SiF_4$$

where SiF_4, tetrafluorosilane is a volatile etch product and was removed by pumping. After few seconds of etch step, SF_6 is terminated instantly and C_4F_8 gas is injected into the chamber to begin the passivation phase. During this phase, CF_2 is formed from C_4F_8, which adsorbs on the etched surfaces and forms a teflon-like polymer passivation layer.

$$n\ CF_2 + * \rightarrow (CF_2)_n$$

The process is then again switched to the etch step where CF_2 molecules are removed by combination of physical ion sputtering and chemical reactions. Due to directional ion bombardment of the substrate, polymer removal rate is greater for the horizontal surfaces, thus the sidewalls remains protected during the etch phase. A well balanced gas flow rates, etch times, and deposition steps were key to attaining high aspect ratio patterns with vertical sidewalls. Also, as the substrate temperature is 10 ^{0}C, the polymer passivation layer was far from both the melting and freezing regimes, and this was also necessary for the production of smooth and vertical sidewalls. Though the process is terminated with an etch phase and a well balanced phases are timed, still there are issues of incomplete polymer removal as revealed by XPS studies. A very thin amorphous polymer layer might exist on the sidewalls of the pillars as observed in HRTEM (**Figure 5.4(d)**) otherwise they will be correlated with the broadening of the base. However, the Teflon-like polymer can be useful as an anti-stiction film **[48]**.

The selection of mask material is an important factor to control over aspect ratio of the features, sidewall profile and etch roughness. A higher selectivity of the mask over silica and Si is required to achieve the desired features because the mask interacts with the etching process parameters. No narrowing of the base of the pillars was observed indicates the robust nature of the mask. It is believed that there is no

measurable degradation of iron oxide nanodots during the etch processes as their dimensions remains unchanged and the unaltered chemical composition of the oxide phase can be observed. The oxygen gas was strictly excluded from the chamber as it erodes the mask and retards the Si etch rate. It is reported by Nakayama et al. that a thin iron oxide layer can perform as an excellent resistant mask to iron fluoride formation in the absence of oxygen **[49]**. Similarly, the erosion of the Ni mask was seen to decrease with the oxygen content as it forms a thin oxide layer on the surface **[23]**. The methodology described here offers the advantage of high mask resolution on small feature sizes (~ 15 nm) without mask-induced roughness or undesired sloping of the sidewalls. To date, there are some reports on the use of metal and oxide masks (Ga, SiO_2, alumina etc.) with good selectivity but either they are grown or deposited as uniform layers followed by pattern transfer (from another material or resist) to that mask and this increases the number of processing steps or suffers from challenges with mask removal without pattern damage **[19, 50, 51]**. Here, we have demonstrated iron oxide as an easy removable highly selective mask material over Si. The relatively simple mask fabrication procedure with the standard existing etch recipes could significantly improve the manufacturing yield and reduce fabrication costs.

5.5. Conclusion

In summary, we have demonstrated the iron oxide nanodots prepared by a simple and cost effective block copolymer inclusion technique are an excellent resistant mask for Si under the etch conditions that were developed. Large area ordered periodic rectangular cross section Si nanopillar or nanowire arrays are fabricated with a smooth vertical sidewall profiles. The diameter and length of the nanopillars was precisely controlled by changing the diameter of the nanodots and increasing the etching time respectively without altering their shape. The effect of the etching parameters on the mask and the substrate is demonstrated in terms of the mask stability and interactions between them. The hard mask could be easily removed without significant pattern damage. The nanopillars observed were crystalline with desirable uni-axial crystallographic orientation. NBOHC was

suggested as the source of light emission from the Si nanopillar arrays similar to that seen for porous Si. The large area controlled periodic Si nanopillar arrays with desirable crystallographic orientation that are fabricated here demonstrate that BCP lithography can be an important component in the manufacturing of future nanoscale devices that employ Si.

5.6. References

[1] Ma, D. D. D.; Lee, C. S.; Au, F. C. K.; Tong S. Y.; Lee, S. T.; *Science* **2003**, 299, 1874.

[2] Cui, Y.; Lieber, C. M.; *Science* **2001**, 291, 851.

[3] Zhao, X. Y.; Wei, C. M.; Yang, L.; Chou, M. Y.; *Phys. Rev. Lett.* **2004**, 92**,** 236805-1.

[4] Delerue, C.; Allan, G.; Lannoo, M.; *Physical Review B* **1993**, 48, 11024.

[5] Yorikawa, H.; Uchida H.; Muramatsu, S.; *J. Appl. Phys.* **1996**, 79, 3619.

[6] Rakhshandehroo, M. R.; Pang, S. W.; *J. Vac. Sci. Technol. B* **1996**, 14, 612.

[7] Talin, A. A.; Hunter, L. L.; Leonard, F.; Rokad, B.; *Appl. Phys. Lett.* **2006**, 89, 153102.

[8] Zhu, J.; Hsu, C. M.; Yu, Z. F.; Fan, S. H.; Cui, Y.; *Nano Lett.* **2010**, 10, 1979.

[9] Wanekaya, A. K.; Chen, W.; Myung, N. V.; Mulchandani, A.; *Electroanalysis* **2006**, 18, 533.

[10] Wolkin, M. V.; Jorne, J.; Fauchet, P. M.; Allan, G.; Delerue, C.; *Phys. Rev. Lett.* **1999**, 82, 197.

[11] Tiwari, S.; Rana, F.; Hanafi, H.; Hartstein, A.; Crabbe, E. F.; Chan, K.; *Appl. Phys. Lett.* **1996**, 68, 1377.

[12] Wallraff, G. M.; Hinsberg, W. D.; *Chem. Rev.* **1999**, 99, 1801.

[13] Liu, C. C.; Nealey, P. F.; Ting, Y. H.; Wendt, A. E.; *J. Vac. Sci. Technol. B* **2007**, 25, 1963.

[14] Park, M.; Harrison, C.; Chaikin, P. M.; Register, R. A.; Adamson, D. H.; *Science* **1997**, 276, 1401.

[15] Farrell, R. A.; Fitzgerald, T. G.; Borah, D.; Holmes, J. D.; Morris, M. A.; *Int. J. Mol. Sci.* **2009**, 10, 3671.

[16] Farrell, R. A.; Petkov, N.; Shaw, M. T.; Djara, V.; Holmes, J. D.; Morris, M. A.; *Macromolecules* **2010**, 43, 8651.

[17] Borah, D.; Shaw, M. T.; Rasappa, S.; Farrell, R. A.; O'Mahony, C.; Faulkner, C. M.; Bosea, M.; Gleeson, P.; Holmes, J. D.; Morris, M. A.; *J. Phys. D-Appl. Phys.* **2011**, 44, 174012.

[18] Barth, M.; Kouba, J.; Stingl, J.; Lochel, B.; Bensona, O.; *Opt. Express* **2007**, 15, 17231.

[19] Fang, Q. L.; Li, X. D.; Tuan, A. P.; Perumal, J., Kim, D. P.; *J. Mater. Chem.* **2011**, 21, 4657.

[20] Lim, K. M.; Gupta, S.; Ropp, C.; Waks, E.; *Microelectron. Eng.* **2011**, 88, 994.

[21] Rangelow, I. W.; *Vacuum* **2001**, 62, 279.

[22] Krishnamoorthy, S.; Manipaddy, K. K.; Yap, F. L.; *Adv. Funct. Mater.* **2011**, 21, 1102.

[23] Hsieh, H. Y.; Huang, S. H.; Liao, K. F.; Su, S. K.; Lai, C. H.; Chen, L. J.; *Nanotechnology* **2007**, 18, 505305.

[24] Ghoshal, T.; Maity, T.; Godsell, J. F.; Roy, S.; Morris, M. A.; *Adv. Mater.* **2012**, 24, 2390.

[25] Ghoshal, T.; Shaw, M. T.; Bolger, C. T.; Holmes, J. D.; Morris, M. A.; *J. Mater. Chem.* **2012**, 22, 12083.

[26] Mokarian-Tabari, P.; Collins, T. W.; Holmes, J. D.; Morris, M. A.; *ACS Nano* **2011**, 5, 4617.

[27] Morioka, T.; Kimura, S.; Tsuda, N.; Kaito, C.; Saito, Y.; Koike, C.; *Mon. Not. Roy. Astron. Soc.* **1998**, 299, 78.

[28] Inokuma, T.; Kurata, Y.; Hasegawa, S.; *J. Lumines.* **1998**, 80, 247.

[29] Pai, P. G.; Chao, S. S.; Takagi, Y.; Lucovsky, G.; *J. Vac. Sci. Technol. A-Vac. Surf. Films* **1986**, 4, 689.

[30] Namduri, H.; Nasrazadani, S.; *Corrosion Sci.* **2008**, 50, 2493.

[31] Zhang, W.; Dubois, M.; Guerin, K.; Bonnet, P.; Kharbache, H.; Masin, F.; Kharitonov, A. P.; Hamwi, A.; *Phys. Chem. Chem. Phys.* **2010**, 12, 1388.

[32] Gu, Z.; Peng, H.; Hauge, R. H.; Smalley, R. E.; Margrave, J. L.; *Nano Lett.* **2002**, 2, 1009.

[33] Standaert, T.; Schaepkens, M.; Rueger, N. R.; Sebel, P. G. M.; Oehrlein, G. S.; Cook, J. M.; *J. Vac. Sci. Technol. A-Vac. Surf. Films* **1998**, 16, 239.

[34] Yang, J. Q.; Liu, Y.; Ye, Z. Y.; Yang, D. Z.; He, S. Y.; *Tribol. Lett.* **2010**, 40, 139.

[35] Fujii, T.; de Groot, F. M. F.; Sawatzky, G. A.; Voogt, F. C.; Hibma, T.; Okada, K.; *Physical Review B* **1999**, 59, 3195.

[36] Maiti, J.; Kakati, N.; Lee, S. H.; Yoon, Y. S.; *J. Fluor. Chem.* **2012**, 135, 362.

[37] Peng, K. Q.; Wu, Y.; Fang, H.; Zhong, X. Y.; Xu, Y.; Zhu, J.; *Angew. Chem.-Int. Edit.* **2005**, 44, 2737.

[38] Wilson, W. L.; Szajowski, P. F.; Brus, L. E.; *Science* **1993**, 262, 1242.

[39] Zou, B. S.; Wang, J. P.; Liu, C.; Zhang, J. Z.; El-Sayad, M. A.; *Physical Review B* **2000**, 62, 16595.

[40] Yuan, J.; Haneman, D.; *J. Appl. Phys.* **1999**, 86, 2358.

[41] Li, A. P.; Bai, G. F.; Chen, K. M.; Ma, Z. C.; Zong, W. H.; Zhang, Y. X.; Qin, G. G.; *Thin Solid Films* **1998**, 325, 137.

[42] Skuja, L.; *J. Non-Cryst. Solids* **1994**, 179, 51.

[43] Prokes, S. M.; *Appl. Phys. Lett.* **1993**, 62, 3244.

[44] Qin, G. G.; Huang, Y. M.; Lin, J.; Zhang, L. Z.; Zong, B. Q.; Zhang, B. R.; *Solid State Commun.* **1995**, 94, 607.

[45] Qin, G.; Qin, G. G.; *J. Appl. Phys.* **1997**, 82, 2572.

[46] An, K. J.; Kim, H. S.; Yoo, J. B.; Yeom, G. Y.; *Thin Solid Films* **1999**, 341, 176.

[47] Boulousis, G.; Constantoudis, V.; Kokkoris, G.; Gogolides, E.; *Nanotechnology* **2008**, 19, 255301.

[48] Nilsson, D.; Jensen, S.; Menon, A.; *J. Micromech. Microeng.* **2003**, 13, S57.

[49] Nakayama, K.; Kobayashi, T.; *Wear* **1996**, 198, 52.

[50] Chekurov, N.; Grigoras, K.; Peltonen, A.; Franssila, S.; Tittonen, I.; *Nanotechnology* **2009**, 20, 65307.

[51] Sainiemi, L.; Keskinen, H.; Aromaa, M.; Luosujarvi, L.; Grigoras, K.; Kotiaho, T.; Makela, J. M.; Franssila, S.; *Nanotechnology* **2007**, 18, 505303.

6.1. Abstract

We report a simple technique to fabricate horizontal, uniform silicon (Si) nanowire arrays with controlled orientation and density at spatially well-defined locations on a substrate based on *insitu* hard mask pattern formation approach by microphase separated polystyrene-*b*-poly(ethylene oxide) (PS-*b*-PEO) block copolymer (BCP) thin films. The methodology may be applicable to large scale production. Ordered microphase separated patterns of the BCP were defined by solvent annealing and the orientation was controlled by film thickness and annealing time. Films of PEO cylinders with parallel orientation (to the surface plane) were applied to create 'templates' for the generation of inorganic oxide nanowire arrays. These PEO cylinders were subject to selective metal ion inclusion and subsequent processing was used to create iron oxide nanowire arrays. The oxide nanowires were isolated, of uniform diameter and their structure a mimic of the original BCP nanopatterns. The phase purity, crystallinity and thermal stability of the nanowires coupled to the ease of large scale production may make them useful in technological applications. Here, we demonstrate that the oxide nanowire arrays could be used as a resist mask to fabricate densely packed, identical ordered, good fidelity silicon nanowire arrays on the substrate. The techniques may have significant application in the manufacture of transistor circuitry.

6.2. Introduction

The computer processor industry is facing a number of challenges in defining one-dimensional (1-D) (nanowire) structures at substrate surfaces **[1]**. These challenges are related to lithographic and etch limitations and, in particular, the need to use double or triple patterning to create ultra-small 1-D features for use in logic or interconnect circuitry. Advances in extreme UV lithography have been slow and costs are spiralling. Directed self-assembly (DSA) where arrays of nanowires can be created by a combination of spontaneous arrangement of materials and 'directing' forces which force the patterns into alignment with a surface feature/direction **[1]**. The most promising technique appears to be the DSA of block copolymers (BCPs) which has been shown to form a number of highly regular nanostructure arrangements due to the thermodynamic incompatibility of the blocks by a process

known as microphase separation where the interfacial energies of the solid substrate and the air interface contribute appreciably to the equilibrium free energy **[2-5]**. Many strategies have been investigated to manipulate interfacial interactions, to obtain a specific orientation and/or lateral ordering of the microdomains including external fields (magnetic, electrical), sample temperature gradient, mechanical effects such as rubbing and substrate topographical and chemical patterns **[6-9]**. Spin coating and solvent annealing is an efficient approach where ordering can be achieved in short time periods under solvent atmospheres since the solvent swells the polymer, creating free volume and providing the necessary chain mobility to the polymer blocks to facilitate self-assembly **[10, 11]**. In particular, control over microdomain orientation is dictated by a complex interplay of surface energies, polymer-solvent interactions, and the commensurability between the film thickness **[12]**. The delivery of BCP lithography would not only afford means of extending logic device feature size reduction but might also promise cost-effective means of generating applications such as flexible electronic devices and sensors.

However, whilst BCP lithography has been demonstrated for the definition of horizontally (to the surface plane) orientated and aligned nanowire structures **[13-15],** a number of challenges exist. Amongst these are: the ultimate feature size attainable, definition of the pre-patterns, defect density etc. Lamellar forming diblock BCPs (DBCPs) are favoured because of the ease of pattern transfer but are challenging because this phase is particularly sensitive to the interfacial energies of the substrate surface and the air interface **[16-18]**. Further, lamellar forming, small feature size DBCPs appear to be few in number. The cylindrical phase appears to be more easily controlled since interfacial energy control is less demanding, however, the pattern transfer of this structure is extremely challenging because of the distribution of one block in a matrix of the other and the small diameter of the cylinders **[19-21]**. For vertically orientated cylindrical phase systems, we have demonstrated in the previous chapter that thin films of DBCP can be used to create vertical nanowire structures by a method of oxide inclusion to allow formation of a hard mask **[22, 23]**. These structures are amenable to material modification because both blocks are present at the surface. Less clear is how horizontally aligned cylinders may be modified by techniques such as nanoparticle decoration or CVD.

In this chapter we report the first application of an inclusion technique that allows selective infill of a cylindrical structure such that continuous wires can be formed across a substrate surface. We have further showed that this can be used to generate oxide hard mask arrays to transfer to the substrate and form silicon nanowires. A number of difficulties have been met and dealt with including: creation of single cylinder structures over large area, fine tuning of the inclusion methodology to yield high quality nanowire structures and proper characterization of the ultra-small features formed. The work clearly demonstrates that cylindrical structures may be used to form high quality horizontal 1-D silicon nanopatterns for logic/interconnect applications. This also asserts that it will enable the application of nanowire based technologies in many other areas.

6.3. Materials and methods

6.3.1. Materials

Single crystal B doped P- type Si <100> wafers (thickness 650 μm, resistivity 6-14 ohm-cm) with a native oxide layer were used as substrates. No attempt was made to remove the native oxide layer. Polystyrene-*block*-poly(ethylene oxide) (PS-*b*-PEO) diblock copolymer was purchased from Polymer Source, Inc., Canada, and used without further purification (M_n, PS = 42.0 kg mol^{-1}, M_n, PEO = 11.5 kg mol^{-1}, M_w/M_n = 1.07, $\mathbf{M_n}$: number-average molecular weight, $\boldsymbol{M_w}$: weight-average molecular weight). Ethanol (99.5%, anhydrous), toluene (99.8%, anhydrous), oxalic acid dihydrate ($C_2H_2O_4$, $2H_2O$), Iron (III) nitrate nonahydrate ($Fe(NO_3)_3$, $9H_2O$) were purchased from Sigma-Aldrich and used without further purification unless otherwise stated. De-ionized water was used wherever necessary.

6.3.2. Preparation of iron oxide nanowire arrays

Substrates were cleaned by ultrasonication in acetone and toluene for 30 minutes in each solvent and dried under nitrogen stream. PS-*b*-PEO was dissolved in toluene to yield 1.0 wt. %, 2.0 wt % and 3.0 wt. % polymer solution and aged for 12 h at room temperature. The PS-*b*-PEO thin film was formed by spin coating the polymer solution (3000 rpm for 30 s). To control the structure of the film and properly define parallel orientated cylindrical structures, careful control of the annealing solvent and film thickness were required. The ellipsometry measured film

thicknesses were 40 nm, 72 nm and 108 nm for 1.0 wt. %, 2.0 wt. %, and 3.0 wt. % polymer solution concentrations respectively. The films were exposed to toluene vapour placed at the bottom of a closed vessel kept at 333 K for different time period to induce necessary chain mobility and allow microphase separation to occur. Partial etching and domain modification of PEO was carried out by ultrasonication of the films for 20 min or immersing the film at 313 K for 21 h in anhydrous alcohol. The ultrasonication treatment was carried out in Cole-Parmer ultrasonic cleaner 8891 which transform low-frequency AC current into 42 kHz high-frequency sound waves via a piezoelectric transducer. During ultrasonication, the solvent annealed films were placed at the bottom of a glass bottle filled with anhydrous alcohol at room temperature. After the desired time, the films were taken out from alcohol and dried immediately. For the fabrication of iron oxide nanowires, Iron (III) nitrate nonahydrate ($Fe(NO_3)_3,9H_2O$) was dissolved in ethanol and spin-coated onto the activated film. UV/Ozone treatment was used to oxidize the precursor and remove polymer. The thermal stability of the nanowire arrays was verified by annealing them at 1073 K for 1 h.

6.3.3. Pattern transfer using ICP etch

These iron oxide nanowire arrays were used as a hard mask for pattern transfer to the substrate using an STS, Advanced Oxide Etch (AOE) ICP etcher as previously reported with the nanodot arrays **[23]**. The system has two different RF generators, one, to generate and control the plasma density by direct connection to the antenna coil, while the other one was used to adjust and control the energy of the ions by connecting it to the substrate holder. A double etching process was used to, firstly, etch the native silica layer and, secondly, the silicon substrate. During etching, the sample is thermally bonded to a cooled chuck (283 K) with a pressure 9.5 Torr. For the oxide layer etch, the process parameters were optimised to a C_4F_8/H_2 gas mixture (21 sccm/30 sccm) using an ICP coil power of 800 W and a Reactive Ion Etching (RIE) power of 80 W. The silica etch time was kept constant (5 s) for all the samples. For silicon pillar fabrication, the process used a controlled gas mixture of C_4F_8/SF_6 at flow rates of 90 sccm/30 sccm respectively and the ICP and RIE power were set to 600 W and 15 W respectively at a chamber pressure of 15 mTorr.

A schematic detailing the fabrication of the Si nanowires is shown in **Scheme 6.1**. Solvent annealing of the spin coated film (**Scheme 6.1(A)**) in toluene produces hexagonally arranged PEO cylinders parallel to the substrate in PS matrix (**Scheme 6.1(B)**). Modification of PEO cylinders creates nanoporous template for the metal ion inclusion (**Scheme 6.1(C)**). Iron oxide nanowires were prepared by spin coating

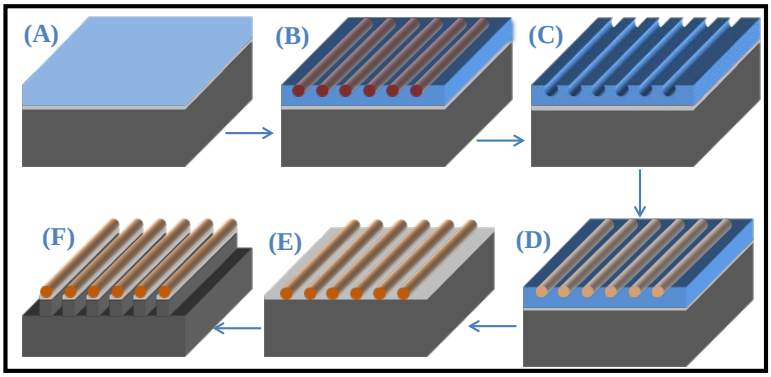

Scheme 6.1. Schematic illustration of the fabrication of horizontal ordered Si nanowires on substrate. **(A)** PS-*b*-PEO thin film after spin coating **(B)** PEO cylinders parallel to the substrate in the PS matrix after solvent annealing **(C)** Modification of PEO cylinders creates nanoporous template **(D)** Iron precursor solution spin coated on the template **(E)** Iron oxide nanowires formed after UV/ozone treatment **(F)** Si nanowires fabricated by consecutive silica and silicon ICP etch processes.

metal ion precursor solution (**Scheme 6.1(D)**) followed by UV/ozone treatment to oxidize the precursor and remove the polymer (**Scheme 6.1(E)**). Si nanowires were fabricated by consecutive silica and silicon ICP etch processes (**Scheme 6.1(F)**).

6.3.4. Characterizations of materials

6.3.4.1. Scanning Electron Microscopy (SEM)

Top-down and cross-sectional scanning electron microscope (SEM) images were obtained by a high resolution (< 1 nm) Field Emission Zeiss Ultra Plus-SEM with a Gemini® column, FEI Company and FEG Quanta 6700 at an accelerating voltage of 5 kV.

6.3.4.2. Atomic Force Microscopy (AFM)

Atomic Force Microscope (DME 2452 DualScope Scanner DS AFM) was operated in AC (tapping) mode under ambient conditions using silicon microcantilever probe tips with a force constant of 60,000 N m^{-1} and a scanning force of 0.11 nN. Topographic and phase images were recorded simultaneously.

6.3.4.3. Film thickness measurements

BCP thin film thicknesses were determined by ellipsometry (Plasmos SD2000 Ellipsometer). An average of three readings collected from different locations on a sample surface was used as the film thickness result.

6.3.4.4. Focused Ion Beam (FIB)

An FEI Strata 235-Focused Ion Beam (FIB) tool was used to generate FIB lamellae cross-sections. E-beam produced platinum was deposited at the substrate followed by the ion-beam deposited platinum. Milling and polishing of the samples were carried out at the lower aperture size and the specimen was imaged under the higher resolution Zeiss Ultra Plus-SEM.

6.3.4.5. Transmission Electron Microscopy (TEM)

Samples were prepared for TEM cross sectional imaging with Zeiss Auriga - Focused Ion Beam (FIB) dual beam system were further imaged by transmission electron microscopy (TEM, FEI Titan) operating at an accelerating voltage of 130 keV.

6.3.4.6. X-ray Photoelectron Spectroscopy (XPS)

X-Ray photoelectron spectroscopy (XPS) experiments were conducted on a Thermo K-alpha machine with Al K_α X-ray source operating at 72 W.

6.4. Results and discussion

6.4.1. Self-assembly of PS-b-PEO

Figure 6.1 summarizes the microdomain structure formation as a function of the solvent anneal time for each different film thicknesses. A hexagonally ordered structure is indicated in all of the AFM images. After 30 min solvent annealing, the PEO cylinders oriented normal to the substrate irrespective of film thicknesses (**Figures 6.1(a, d, g)**). The repeat period calculated from the Fast-Fourier Transform (FFT) of the AFM images is 42 nm and this value (+/- 2%) was observed for all films irrespective of orientation. When the anneal period is increased to 1 h, a hybrid morphology consisting of cylinders oriented both parallel and perpendicular to the surface plane is observed but note that the fraction of parallel cylinders increases with increasing film thickness as shown in the inset of **Figures 6.1(a, d, g)**. For the thickest film (3.0 wt. %), nanosized triangular islands of different thickness can be

seen (inset of **Figure 6.1(g)**). For the thin film (1.0 wt. %), parallel orientation is predominant after 1 h 30 min (not shown) but perpendicular domains were still present. Complete parallel orientation of the thinnest film was only observed at solvent exposure times of 2 h (**Figure 6.1(b)**) and 2 h 30 min (**Figure 6.1(c)**) and this is stable to 4 h. For thicker films, parallel and perpendicular cylinders coexist with parallel orientation as a major assembly for longer annealing times (**Figures 6.1(e, f, h i)**). Compared to the thin films, large scale surface roughness or thickness

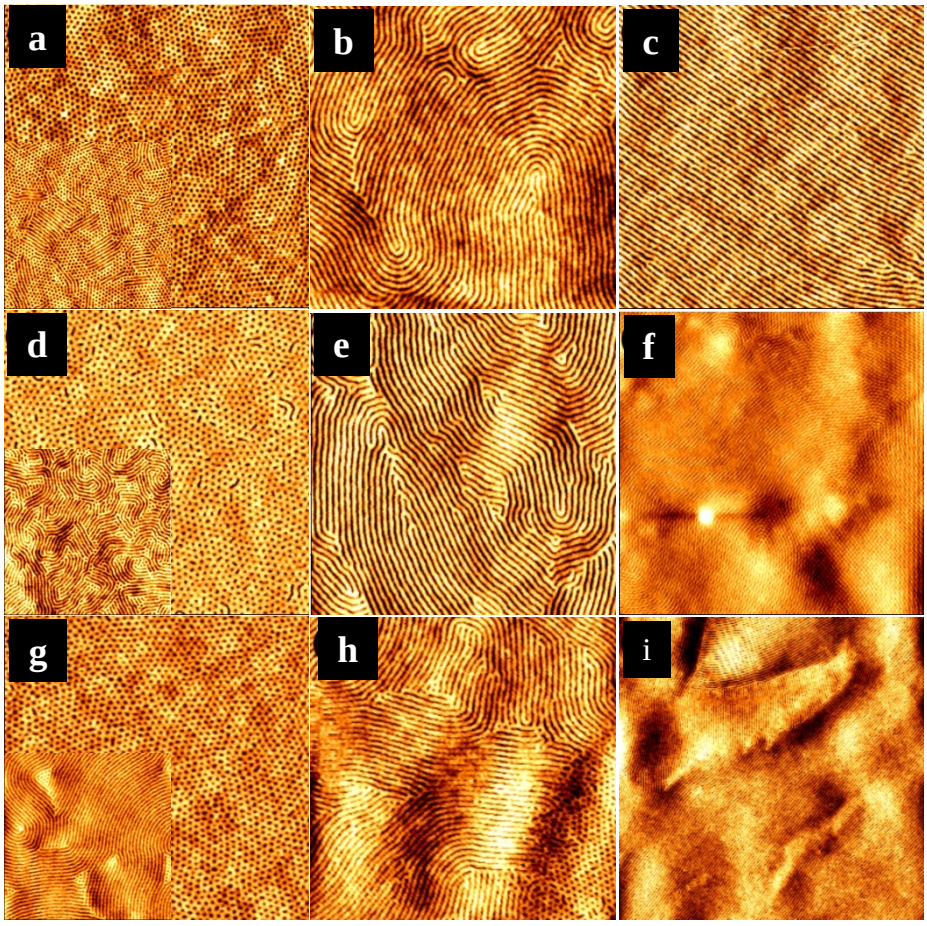

Figure 6.1. Tapping mode AFM images of the solvent annealed film with **(a, a-inset, b, c)** 1.0 wt. %, **(d, d-inset, e, f)** 2.0 wt. % and **(g, g-inset, h, i)** 3.0 wt. % polymeric solution for 30 min, 1 h, 2 h and 2 h 30 min respectively. All the images are 2 x 2 μm. **(f)** 5 x 5 μm. **(i)** 4 x 4 μm.

undulation is noticed with longer solvent exposure (2 h 30 min) as shown in **Figures 6.1(f)** (5 x 5 μm) and **Figure 6.1(i)** (4 x 4 μm). The thickness dissimilarity and wavy nature of the surface is evident from the combination and differences in the colours of the film surfaces by the microscopic images for the films annealed for 2 h 30 min

(**Figure AII.1**). Hence, thinner films exhibit lower defect densities and smoother surface compared to the thicker films at similar temperature.

It should be noted that the PS-*b*-PEO system is complex as the blocks exhibit asymmetric affinities for the solid substrate and the air interface. Previous work suggest that the hydrophilic PEO will preferentially wet the substrate surface (favourable PEO-substrate interactions) whilst PS will segregate to the air interface to form a PS-rich layer (PS has a lower surface energy, γ_{PS} = 33 mNm^{-1}; γ_{PEO} = 43 mNm^{-1}) **[24]**. Although PEO dissolves in toluene, the toluene is a selective solvent for PS since the solubility parameter difference with PS is much smaller ($\delta_{Tol} - \delta_{PS}$ = 18.3-18 =0.3 $MPa^{1/2}$) than PEO does ($\delta_{Tol} - \delta_{PEO}$ = 18.3-20.2 =1.9 $MPa^{1/2}$). In order to ensure complete diffusivity of toluene through the PS matrix **[11],** the solvent anneal temperature used was optimized at 333 K, which is just above the melting temperature of the PEO block (328 K) for this particular molecular weight system. Thus, PEO is in a semi-molten state during annealing and this probably explains some of the ease with which the system re-orientates and changes morphology during annealing, simultaneously lower diffusivity and high viscosity of the domains facilitate the same translational order.

This information may be used to explain the observations here. Short-period solvent annealing gives a vertical orientation because this represents the least entropically hindered route to microphase separation, since the PEO cylinder length is limited to the thickness of the films. However, at extended periods this phase can relatively easily re-orientate into a parallel orientation which although entropically less favoured allows PS to form the majority surface block and minimize the free energy of the system. The parallel orientation is favoured at the correct monolayer (relative to cylinder repeat distance). Clearly, the thinnest film shows the greatest tendency to produce a stable parallel arrangement whilst thicker films show increased likelihood of forming mixed orientations. For relatively thicker films, the internal morphology is unknown and the surface patterns may not essentially be propagated through the entire film thickness. Because the substrate oriented interfacial layer should be separated from the region far above where ordering should be dominated by the polymer-air interface where the mixed morphologies may coexist in the interfacial layer. **Scheme 6.2** demonstrates the equilibrium surface

patterns, thicknesses and internal morphology for different concentrations of polymers for longer annealing time (2 h). A simple explanation of this observation is that thermodynamics become less favourable to the parallel orientation as thickness increases **[25]**. Instead, the increased roughness (a direct result of having non-ideal thickness) will favour parallel arrangements in regions where film thickness is ideal and vertical orientation in non-ideal circumstances.

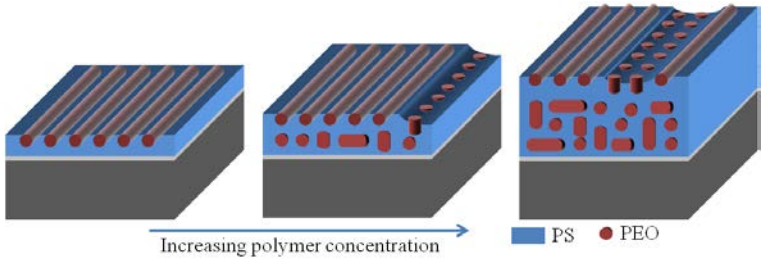

Scheme 6.2. Schematic illustration of equilibrium surface patterns, thicknesses and internal morphology for different concentrations of polymers for longer annealing time (2 h).

It is noted that the larger free energy for a monolayer film compared to a multilayer film **[25]** can cause frequent structural transition in order to release the extra tension. Residual solvent may also be of importance here to explain stable surface pattern morphology for thinner films for longer annealing times. The trapping of solvent (toluene) in the solvent annealed films due to the vitrification of the film during solvent removal can have significant effects **[26]**. The trapped solvent may cause defects in the surface morphology and also modify the polymer-substrate, polymer-air and polymer-polymer interactions. The increased order and the uniformity of pattern orientation for the thinnest films could be due to significantly less residual solvent and lack of a well-defined solvent front. For thicker films, longer time is required to evaporate the solvent due to combined effects of sufficiently large film thickness and attractive interaction of the solvent with the substrate **[27]**. The presence of significant solvent in thicker films may also help to form the island type structure observed (e.g. in the inset of **Figure 7.1(g)** small triangular islands of area ~ 40-80 nm^2 and average height about 2-3 nm are readily formed) due to solvent enhancing the large mass transport required. On

extended solvent annealing, larger islands form presumably following two dimensional Ostwald ripening type mechanisms (**Figure 6.1(h)**).

6.4.2. Nanoporous template fabrication using ethanol treatment

As previously shown in chapter 6 for vertically orientated hexagonally arranged cylinder structures of this BCP systems in order to include inorganic materials it is necessary to activate the PEO, a process that leads to removal and densification of the PEO domains to produce nanopores **[22, 24]**. Chemical degradation and/or modification of the PEO blocks were achieved through ultrasonication or simply immersing the film at a certain temperature in anhydrous ethanol. Both the processes are efficient but the immersion process is time-consuming. Since ethanol is a non-selective solvent for PS, this suggests that in the horizontally aligned films developed here that at least parts of the PEO cylinders are exposed at the film surface. **Figure 6.2** shows the AFM and SEM images of the PS-*b*-PEO systems of different thicknesses BCP films after ultrasonic ethanol treatment (similar for all films). The long-range order, periodicity and spacing (cylinder spacing = 42 nm and PEO cylinder diameter = 18 nm) of the BCP pattern are essentially unchanged by this process. Topographic AFM images (**Figures 6.2(a-c)**) demonstrate contrast enhancement following ethanol ultrasonic treatment. No thickness change on ethanol treatment was observed for the respective films as measured by ellipsometry. No deformation or discontinuity of the nanoporous template was observed. The process is effective for a variety of PEO cylinder lengths formed under different solvent annealing time (**Figure AII.2**). Inset of **Figure 6.2(a)** demonstrate nanoporous line-like pattern over an extended area (2 x 2 μm). **Figure 6.2(d)** demonstrates that the treatment is equally effective for films of mixed cylinder orientation.

It should be noted that the ethanol exposure time had to be carefully optimized as longer exposures/higher temperatures resulted in surface roughness or structural degradation of the film. **Figure 6.2(e)** depicts the morphology of the polymer film (1.0 wt. %) after the ethanol immersion for 14 h. The cylinders have become discontinuous and swollen suggesting initial film decomposition and intermediate stage of the modification. In the case of the thicker films (3.0 wt. %, 24 h ethanol treatment, **Figure 6.2(f**)), the film consists of different layers of cylinder

arrangements where films in different layers are no longer parallel. It is apparent that the longer exposure removed regions of the upper cylinder layers whilst allowing movement of the layers. The same discontinuities as seen in **Figure 6.2(e)** are also observed.

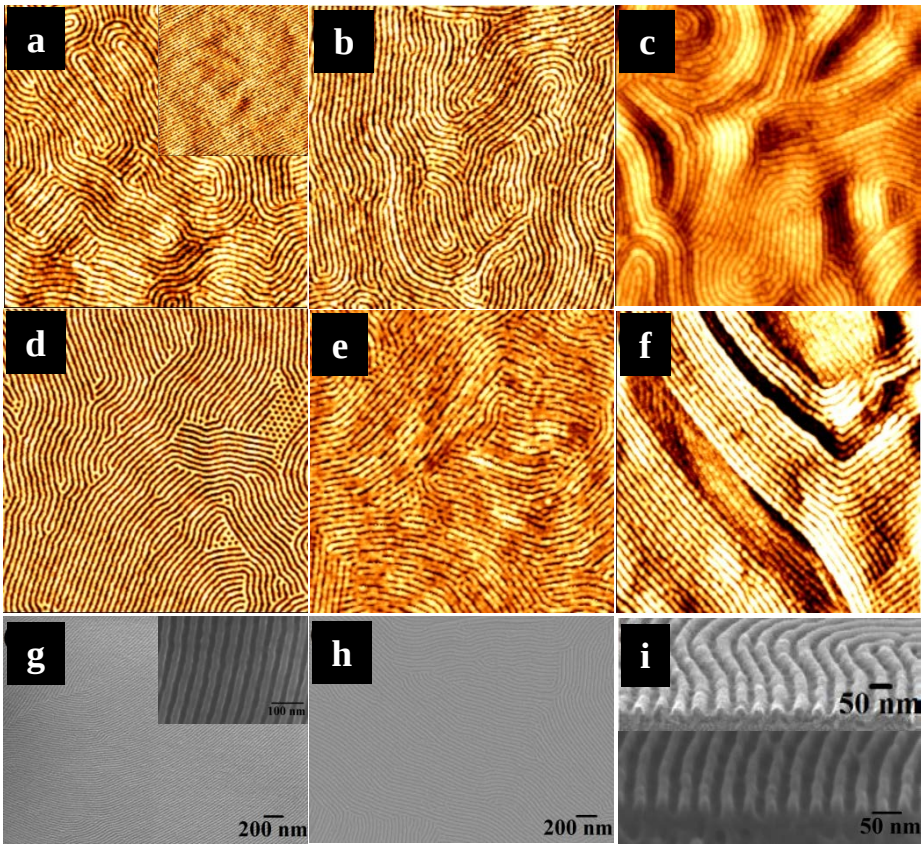

Figure 6.2. AFM and SEM images of the nanoporous template after ethanol treatment for **(a, a-inset, g, g-inset)** 1.0 wt. %, **(b, h)** 2.0 wt. % and **(c)** 3.0 wt. % polymeric solution respectively. **(d)** nanoporous template with mixed morphology. Ethanol treated film for **(e)** 1.0 wt. % film after 14 h and **(f)** 3.0 wt. % film after 24 h. **(i)** cross sectional SEM images of the template with 1.0 wt. % solution. All the AFM images are 2 x 2 μm.

The ability to produce high contrast SEM images for the 1.0 wt. % and 2.0 wt. % polymeric films (**Figures 6.2(g)** and **6.2(h)** respectively) also suggest a height variation across the surface and modification/removal of the PEO. This is confirmed by cross-sectional SEM images in **Figure 6.2(i)** for 1.0 wt. % polymeric film after ethanol treatment. The images were taken from different area of the film and the contrast was adjusted to reveal the underneath polymer layer on top of the silicon

substrate (top image) and the 'missing' PEO cylinders (bottom image). The measured thickness of the template is 40 nm, in close agreement with ellipsometry measurements. We suggest a PS contact layer exists at the substrate interface below the missing cylinders which is further confirmed by TEM (below).

Either the ultrasonic treatment or a certain temperature is required to create the nanoporous templates for the generation of oxide nanostructures. The ethanol treatment process requires comment as acid treatments are normally used for reconstruction or etching of these systems **[21, 28]**. Here, ethanol was preferred as an etching solvent because of its' vapour pressure, selected solubility into PEO (since they have similar solubility parameters) and chemistry. We suggest that the acoustic cavitation during ultrasonication generates free radicals for bond cleavage of the PS-PEO bond. Acoustic cavitation is more aggressive in solvents with a lower vapour pressure (5.95 kPa at 293 K) **[29]**. It was also found that ethanol was the most appropriate of the alcohols. This might suggest that the similarity of the chemical structures of PEO monomers [(CH_2CH_2O)-] and ethanol molecules (H-CH_2CH_2O-H) is important. In this way, the ethanol is highly effective in dissolving PEO fragments and also providing an ideal solvent to allow crystallization of the PEO **[24]**. When ultrasound was ceased, the PEO chains that remains attached to PS form a thin crystalline layer when there is still some ethanol molecules present in the adjacent regions to act as a solvent. Thus, the layer section consists of both ethanol and crystalline PEO as some ethanol is confined within the crystalline PEO layer **[30]**. This appears to be why it is important to take out the film from the solution and dry it as quickly as possible.

6.4.3. TEM and XPS characterization of nanoporous template

Careful cross-sectional TEM helps to resolve the morphology of these films (**Figures 6.3(a)** and **6.3(b)**). Prior to ethanol treatment, (**Figure AII.3**) the similarity of the PS (1.05 g cm^{-3}) and amorphous PEO (1.12 g cm^{-3}) densities results in featureless TEM micrographs. This suggests that solvent annealing does not result in PEO crystallization even at a temperature higher than its melting point since the crystalline form has higher density (1.24 g cm^{-3}) **[31]** and might be expected to provide TEM contrast **[32]**. For both the thickest (3.0 wt. %, **Figure 6.3(a)**) and thinnest (1.0 wt. %, **Figure 6.3(b)**) films indicate that the cylinders affected by the

ethanol treatment are located at the exterior surface. It is also clear that the interior PEO domains below the surface are not altered by the ethanol treatment. The polymer film shows no indication of deformation or delamination at the substrate interface and the TEM derived thicknesses of 113 nm and 40 nm (3.0 wt. % and 1.0 wt. % respectively) are consist with ellipsometry measurements. In the

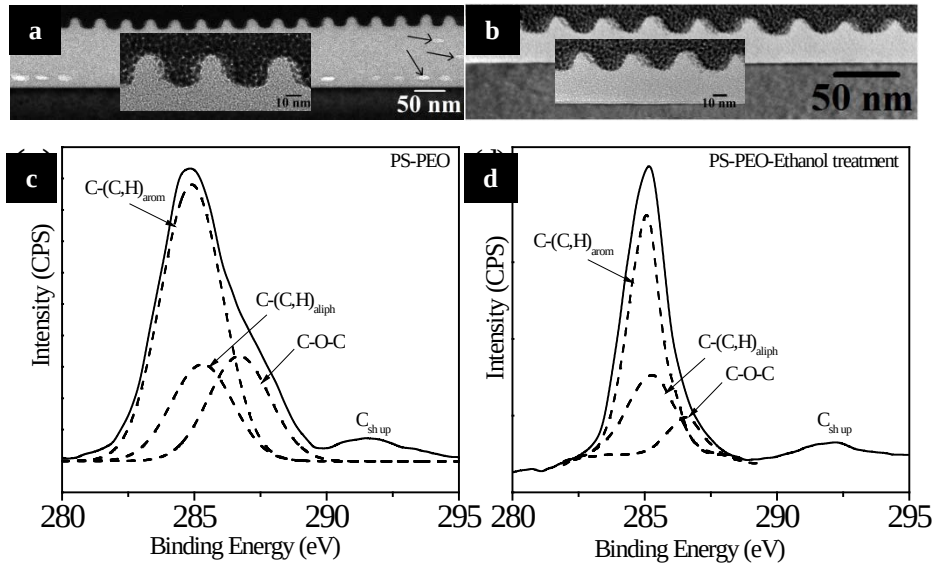

Figure 6.3. FIB thinned cross sectional TEM images of the nanoporous template after ethanol treatment for **(a)** 3.0 wt. % and **(b)** 1.0 wt. % polymeric solution respectively. XPS C1s spectra for **(c)** PS-*b*-PEO solvent annealed and **(d)** ethanol treated film respectively.

3.0 wt. % film, a few elliptical areas within the film can be seen and these are at a similar repeat distance (42 nm) as the cylinder spacing observed above (**Figure 6.3(a)**). We assert that there are crystalline PEO cylinders that are deformed by in plane surface strain **[33]** and demonstrate multilayer formation. Note these are only visible if they are in the correct orientation in the TEM lamellae. We believe some crystallization can occur at 313 K **[31]** and the elliptical regions appear due to the density or contrast enhancement. The 'nanopores' formed by ethanol treatment are a consistent depth of 17 nm across the film. Higher magnification images (insets of **Figures 6.3(a)** and **6.3(b)**) give an average PEO width of 18 nm consistent with top-down images and suggesting that cylinders at the surface are not subject to significant strain. It was not possible to detect the thin layer section within the nanopores because of the thicker platinum layer. Compared to the thin film, a very

thick layer (96 nm) exists underneath the porous structures consisting of both PS and PEO. Whereas only a 23 nm non-porous PS layer exists on top of the silicon substrate as has been suggested before **[2]**.

XPS analyses were performed to provide further understanding of the ethanol process for the 1.0 wt. % film. The C1s peaks can be curve-fitted to reveal four components as illustrated in **Figures 6.3(c)** and 6**.3(d)**. Two of these can be attributed to carbon from the aromatic ring of PS (**C**-$(C,H)_{arom}$) and the aliphatic backbone of PS (**C**-$(C,H)_{aliph}$) at 284.9 eV and 285.3 eV respectively. A distinct high binding energy shoulder on the primary C1s peak can be seen particularly for the untreated sample and this is assigned to carbon involved in an ether link (**C**-O-**C**) from PEO at about 286.6 eV. A shake-up satellite assigned to the aromatic ring of PS ($\mathbf{C}_{sh\ up}$) at about 291.8 eV was also seen. From the total C1s peak area (includes adventitious signal), the calculated contribution of PEO component decreases from 28% to 9% after the ethanol treatment. This is consistent with PEO degradation but also suggests that some PEO remains possibly in a crystalline form.

6.4.4. Iron oxide nanowire characterization

The nanoporous line templates can be used to create ordered oxide nanowire arrays by the metal inclusion method through spin coating the precursor-ethanolic solution and subsequent UV/Ozone treatment. Following previous chapter **[23]**, where it was reported that iron oxide nanodots can be an excellent resistant mask for high aspect ratio silicon substrate patterning. Attempts were made to adopt this strategy to produce silicon nanowire arrays by use of the oxide wires as a hard mask. As shown below, the thinnest BCP film thicknesses produce the best nanowire arrays.

Figures 6.4(a-c) represents the AFM images of the iron oxide nanowires prepared using the templates of thicknesses 40 nm, 72 nm and 113 nm respectively using an equivalent amount of precursor solution. For the 40 nm films, ordered large area nanowire arrays were realized with uniform size/shape and their arrangement mimics that of the original BCP patterns (**Figure 6.4(a)**). The average diameter of the nanowires is 16 nm and equal throughout the entire length. For the thicker films, a few nanowires are seen in discrete areas but irregular, disconnected and agglomerated nanowire assemblies are dominant (**Figures 6.4(b, c** and **f)**). Further,

nanowires of varying diameter along their length are also seen. SEM images also confirm AFM observations as seen in **Figure 6.4(d)**. The thinner film clearly has well defined, large area nanowire arrays and the higher magnification image (inset of **Figure 6.4(d)**) reveals the continuous nature and smooth profile of the nanowires.

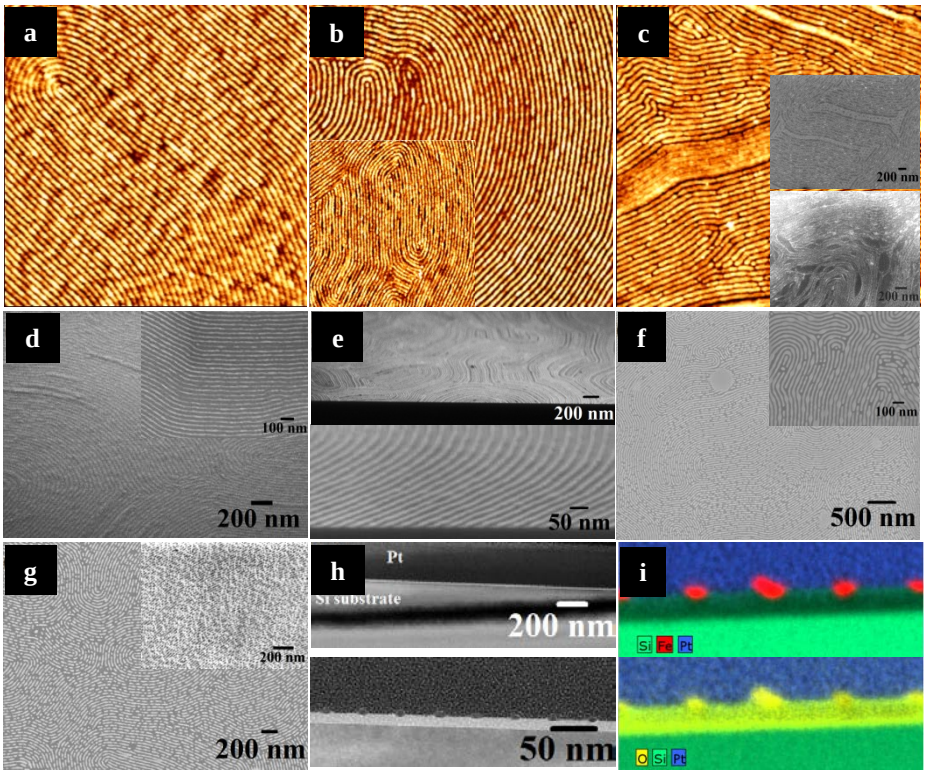

Figure 6.4. Iron oxide nanowires formed after UV/Ozone treatment for different polymeric solution **(a, d)** 1.0 wt. %, **(b, f)** 2.0 wt. % and **(c)** 3.0 wt. % respecticely. Iron oxide nanowires formed annealing at 1073 K for 1 h for different polymeric solution **(e)** 1.0 wt. %, **(f)** 2.0 wt. % and **(inset of c)** 3.0 wt. % respecticely. Oxide nanowires prepared for different concentrations of precursor **(g)** 4.0 wt. % and **(inset of g)** 5.0 wt. % respectively. **(h)** Cross sectional TEM images of iron oxide nanowires. **(i)** elemental mapping of Fe, O and Si.

The nanowires formed using these methods are well-adhered to the substrate and thermally robust. Typical data (**Figure 6.4(e)**) show large area views of the arrays after air calcination at 1073 K for 1 h. Higher magnification images reveals well-isolated, monodispersed arrays with a centre to centre spacing of 42 nm (as previous). As might be expected, for thicker films, disconnected (2.0 wt. %) and entangled (3.0 wt. %) nanowires were formed after air calcination as shown in the insets of **Figures 6.4(f)** and **6.4(c)** respectively. It should be noted that the

concentration of the iron precursor solution is critical and was carefully optimized (4.6 wt. %) to obtain isolated and continuous nanowires (**Appendix AII**). **Figure 6.4(g)** and inset shows the nanostructures formed with two different concentrations; lower concentration (4.0 wt. %) gave non-continuous nanowire-like structures whilst a 5.0 wt. % solution yielded an interconnected nanowire network.

The structural quality, composition and the interfaces were further analysed using FIB-thinned TEM cross-sections. The adhesion of the materials is reflected in the mechanical integrity (i.e. no interfacial cracks etc. at the interface of the wires with the substrate) of the structures during FIB processing. We suggest this approach offers advantages over lithographic patterning of a oxide film where interfacial tensions can result in delamination and mechanical damage under strain **[34]**. The cross-sectional TEM image shows well-separated nanowires supported on the passive silica substrate surface (**Figure 6.4(h)**). The wires are crystalline (**Figure AII.6**) and of average diameter/height 15/6 nm respectively (as previously seen by AFM and SEM). Elemental composition was confirmed by high resolution EDAX mapping and the distribution of Fe, O and Si are shown in **Figures 6.4(i)**. The Fe map shows a homogeneous distribution of Fe corresponding to each nanowire and a sharp elemental interface to the substrate surface suggesting no inter-diffusion occurs. The O and Si maps confirm the presence of oxides on the nanowire and passive layer and the substrate.

6.4.5. XPS analysis of iron oxide nanowires

The chemical composition of the iron oxide nanowires before (UV/Ozone alone) and after annealing was confirmed by Fe 2p XPS studies. Prior to annealing, the Fe 2p core level spectrum of the as-formed iron oxide nanowires (**Figure 6.5(a)**) consists of peaks at 711.1 eV (Fe $2p_{3/2}$) and 724.5 eV (Fe $2p_{1/2}$) which are broadened due to the presence of Fe^{+2} and Fe^{+3} ions. Curve-fitting using Gaussian-Lorentzian line shapes provides individual binding energies of 709.6/722.9 eV (assigned to Fe^{+2}) and 711.5/724.9 eV (Fe^{+3}) in agreement with literature assignments **[35]**. The Fe^{+3}/ Fe^{+2} ratio was estimated to about 2:1 as expected for Fe_3O_4. Following calcination the Fe 2p core level spectrum (**Figure 6.5(b)**) consists of two sharp peaks at 711.4/725.2 eV corresponding to the Fe $2p_{3/2}$ and Fe $2p_{1/2}$ signals. A high binding energy satellite (+8 eV shift) can also be seen and these data

are consistent with formation of Fe_2O_3 **[36, 37]**. A typical XPS survey spectrum (inset of **figure 6.5(b)**) of iron oxide nanowires after annealing confirms the expected presence of Si, O, C and Fe. The C1s feature is relatively small and

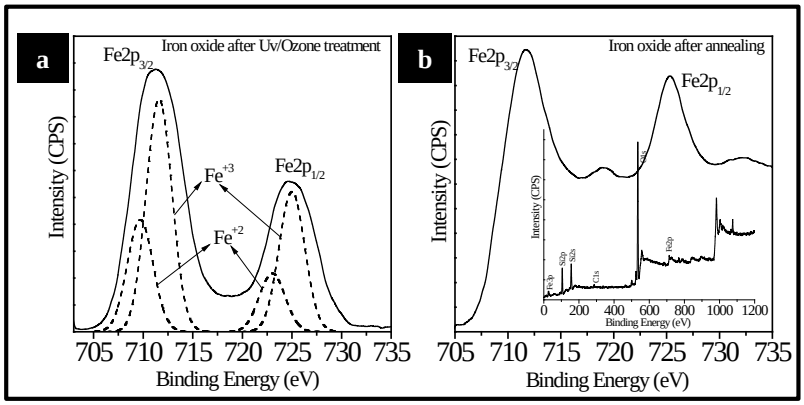

Figure 6.5. Fe 2p spectra of iron oxide nanowires after **(a)** UV/Ozone treatment and **(b)** annealing at 1073 K for 1 h. Inset of b shows XPS Survey spectrum for the annealed sample on silicon substrate.

demonstrates effective removal of carbon species during processing. Its intensity is consistent with adventitious material formed by adsorption and other contamination during sample preparation.

The metal ion inclusion into the nanoporous template is favoured by a combination of capillary forces and the affinity of PEO with the iron ion containing ethanol solution. The spin coating procedure is highly efficient and it is suggested that the PEO-ethanol layer accelerates the metal ion inclusion process probably via either intra- or intermolecular coordination via electron donation from the PEO block to oxygen species in the ethanol molecule **[24]**. The effectiveness of this simple solution mediated inclusion is consistent with the spectroscopic data suggesting the presence of PEO after the ethanol treatment. Had complete removal of the PEO been achieved, it would be highly unlikely that significant metal uptake would occur because the PS matrix would be hydrophobic. For the thicker films, the underlying layer of the nanoporous template consists of both PS and PEO as suggested before and during spin coating, metal ions were incorporated only into the surface pores because the non-porous PEO cylinders underneath were protected by the PS matrix. In this case, UV/Ozone treatment cross-links the polymers, oxidizes the metal-complex, remove the polymer simultaneously and all these processes are kinetically

controlled. The iron oxide nanostructures were interrupted while settles down to the substrate through the thick polymer layer. Increment of polymer layer thickness to a certain extent, the nanostructures experiences diameter variation, edge roughness and periodic irregularity.

6.4.6. Silicon nanowire fabrication using iron oxide as hardmask

In order to create silicon nanowire structures on the substrate surface, the iron oxide nanowires were used as a hardmask in the ICP etch process. A mild oxalic acid aqueous solution was used to remove undesired Fe_2O_3 from the as-formed Si nanowire arrays. **Figure 6.6(a)** shows cross-sectional SEM image of silicon nanowires over large substrate areas following 1 min silicon etch. A higher magnification image (inset of **Figure 6.6(a)**) demonstrate that the nanowires are continuous and of regular diameter (15 nm) along the length. The centre to centre nanowire spacing remained unchanged. This implies that the etching does not damage the original 'mask' to a significant extent. The depth of the nanowires can be varied by increasing the silicon etch time and **Figures 6.6(a-c)** represents the SEM images of the nanowire arrays following etches of 1-3 min. All the images reveal large scale fabrication of ordered continuous silicon nanowires. As the etch time is increased pattern contrast is enhanced and the cross-sectional SEM data give approximate nanowire heights of 50, 100 and 150 nm for 1, 2 and 3 min etches respectively. In all cases, the cross-sectional SEM images show wires of uniform width (with height) and smooth sidewalls demonstrating the mask effectiveness. Note that further increases in etch time may results in nanowire discontinuity in few areas (**Figure AII.5**). It is not clear of this is due to etch degradation or mechanical weakness of the samples. To demonstrate the use of these for making silicon devices, the process was also demonstrated on silicon-on-insulator (SOI) substrates of 30 and 70 nm silicon device layers using adjusted silicon etch times of 30 and 70 s respectively. The top-down SEM reveals similar nanowire assembly on SOI (not shown). The iron oxide nanostructures prepared for lower and higher concentrations of precursors also shows significant contrast enhancement with identical pattern after the silicon etch as shown in **Figure 6.6(d)** and inset. Thus, the fabricated silicon nanopatterns were solely following the original mask patterns on silicon substrate.

Cross-sectional TEM was used to fully characterize the nanowires. **Figures 6.6(e)** and **6.6(f)** show micrographs of the array of 2 min etched nanowires on silicon substrates following iron oxide removal. The images reveal nanowires of about 100 nm long as the expected 42 nm spacing. Contrast at the surface of the wires is seen due to the presence of the original passive layer or due to fluoride formation during etching **[23]**. All of the wires investigated had a rectangular profile with smooth sidewalls and there little variation of wire width along its length as seen in the inset

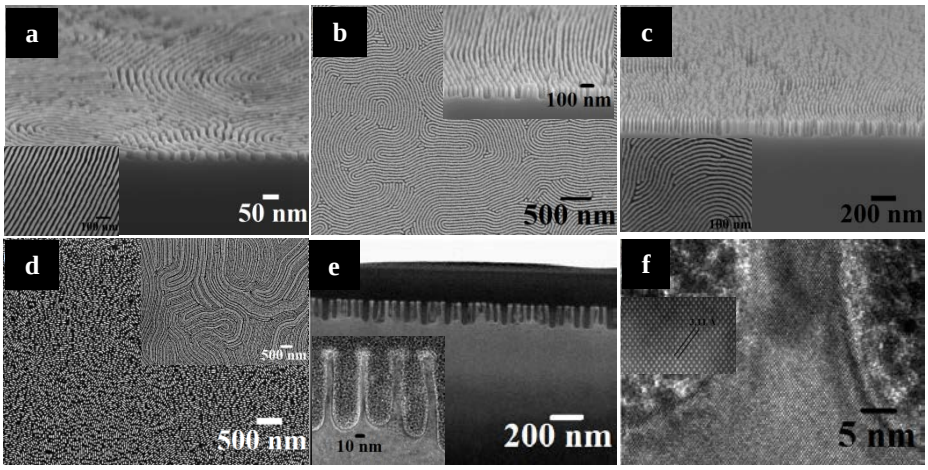

Figure 6.6. SEM images of horizontal silicon nanowires with iron oxide as a hard mask after **(a)** 1 min **(b)** 2 min and **(c)** 3 min silicon etch respectively. **(d)** and inset shows pattern transferred nanostructures for lower and higher concentrations of precursor respectively. **(e)** Cross sectional TEM and **(f)** HRTEM images of silicon nanowires after iron oxide removal.

of **Figure 6.6(e)**. Note that the nanowires are unaltered by iron oxide removal. Importantly, the HRTEM image (**Figure 6.6(f)**) reveals a highly crystalline structure with no sign of etch related amorphortization. Note also that the lattice fringes are continuous between bulk and nanowire silicon indicating no stacking or other defects and hence no re-crystallization during etching. The image in the inset of **Figure 6.6(f)** shows the lattice fringes with spacing 3.11 Å across the wires agrees reasonably well with silicon fcc (111) interplanar distances **[38]**. The 54^{o} angle of the (111) fringes with the substrate surface plane is consistent with the (100) orientation of the silicon wafer. Thus, highly dense uniform 1-D silicon nanowire arrays with controlled crystallographic orientation could be created through selective etching of the silicon wafers of chosen orientations.

6.5. Conclusion

In conclusion, we present a simple and cost effective large-scale fabrication of horizontal, uniform Si nanowire arrays with precise placement on substrate based on insitu hard mask microphase separated BCP approach. Hexagonally arranged self-assembled PS-*b*-PEO nanopatterns were realized by a simple solvent annealing process and the morphological evolution was investigated as function of film thickness and annealing time. This morphological variability is attributed primarily to the trapping of residual solvent (toluene) within the film and the differences in the interfacial energies between the polymer, air and the substrate. Compared to the thicker films, thin film of monolayer cylinders depicts uniform thicknesses and stable surface patterns throughout the film. An effective ethanol ultrasonication/immersion protocol for the degradation or modification of the PEO cylinders was developed to create templates for the generation of inorganic materials without pattern damage. The films of PEO cylinders with parallel orientation were applied for the generation of iron oxide nanowire arrays based on a methodology of selective metal ion inclusion and subsequent UV/Ozone treatment. Monolayer thin films are proven to generate large scale, uniform diameter and smooth sidewall, horizontal iron oxide nanowire arrays while disconnected oxide patterns formed with increasing the film thickness. The nanowires are structurally arranged in a mimic of the original self-assembled BCP pattern and show strong adherence to the substrate to high temperature. Large area, identical ordered, crystalline, horizontal Si nanowire arrays is fabricated with a smooth sidewall profile by using these iron oxide nanowires as a hard mask over silicon. This self-assembled hardmask nanolithography can be employed to fabricate as-made devices of electrically separated Si nanowires with controlled crystallographic orientation on SOI substrate which can be an important component in the manufacturing of nanoscale devices with high throughput and low cost.

6.5. References

[1] Emerging research devices, *The International Technology Roadmap for Semiconductors*, 2011, 1.

[2] Borah, D.; Ozmen, M.; Rasappa, S.; Shaw, M. T.; Holmes, J. D.; Morris, M. A.; *Langmuir*, **2013**, 29, 2809.

[3] Wang, Q.; Nealey, P. F.; de Pablo, J. J.; *Macromolecules*, **2001**, 34, 3458.

[4] Rasappa, S.; Borah, D.; Faulkner, C. C.; Lutz, T.; Shaw, M. T.; Holmes, J. D.; Morris, M. A.; *Nanotechnology*, **2013**, 24.

[5] Borah, D.; Shaw, M. T.; Rasappa, S.; Farrell, R. A.; O'Mahony, C.; Faulkner, C. M.; Bosea, M.; Gleeson, P.; Holmes, J. D.; Morris, M. A.; *J. Phys. D-Appl. Phys.*, **2011**, 44, 174012.

[6] Segalman, R. A.; Yokoyama, H.; Kramer, E. J.; *Adv. Mater.*, **2001**, 13, 1152.

[7] Thurn-Albrecht, T.; Schotter, J.; Kastle, C. A.; Emley, N.; Shibauchi, T.; Krusin-Elbaum, L.; Guarini, K.; Black, C. T.; Tuominen, M. T.; Russell, T. P.; *Science*, **2000**, 290, 2126.

[8] Cheng, J. Y.; Mayes, A. M.; Ross, C. A.; *Nat. Mater.*, **2004**, 3, 823.

[9] De Rosa, C.; Park, C.; Thomas, E. L.; Lotz, B.; *Nature*, **2000**, 405, 433.

[10] Zhao, J. C.; Jiang, S. C.; Ji, X. L.; An, L. J.; Jiang, B. Z.; *Polymer*, **2005**, 46, 6513.

[11] Mokarian-Tabari, P.; Collins, T. W.; Holmes, J. D.; Morris, M. A.; *ACS Nano*, **2011**, 5, 4617.

[12] Fasolka, M. J.; Mayes, A. M.; *Ann. Rev. Mater. Res.*, **2001**, 31, 323.

[13] Peng, Q.; Tseng, Y. C.; Darling, S. B.; Elam, J. W.; *Adv. Mater.*, **2010**, 22, 5129.

[14] Nandan, B.; Gowd, E. B.; Bigall, N. C.; Eychmuller, A.; Formanek, P.; Simon, P.; Stamm, M.; *Adv. Funct. Mater.*, **2009**, 19, 2805.

[15] Gu, X. D.; Dorsey, P.; Russell, T. P.; *Adv. Mater.*, **2012**, 24, 5505.

[16] Potemkin, II, *Macromolecules*, **2004**, 37, 3505.

[17] Farrell, R. A.; Petkov, N.; Shaw, M. T.; Djara, V.; Holmes, J. D.; Morris,; *Macromolecules*, **2010**, 43, 8651.

[18] Kim, E.; Ahn, H.; Park, S.; Lee, H.; Lee, M.; Lee, S.; Kim, T.; Kwak, E. A.; Lee, J. H.; Lei, X.; Huh, J.; Bang, J.; Lee, B.; Ryu, D. Y.; *ACS Nano*, **2013**, *7*, 1952.

[19] Gu, X. D.; Liu, Z. W.; Gunkel, I.; Chourou, S. T.; Hong, S. W.; Olynick, D. L.; Russell, T. P.; *Adv. Mater.*, **2012**, 24, 5688.

[20] Ruiz, R.; Sandstrom, R. L.; Black, C. T.; *Adv. Mater.*, **2007**, 19, 587.

[21] Xu, J.; Hong, S. W.; Gu, W. Y.; Lee, K. Y.; Kuo, D. S.; Xiao, S. G.; Russell, T. P.; *Adv. Mater.*, **2011**, 23, 5755.

[22] Ghoshal, T.; Maity, T.; Godsell, J. F.; Roy, S.; Morris, M. A.; *Adv. Mater.*, **2012**, 24, 2390.

[23] Ghoshal, T.; Senthamaraikannan, R.; Shaw, M. T.; Holmes, J. D.; Morris, M. A.; *Nanoscale*, **2012**, 4, 7743.

[24] Ghoshal, T.; Shaw, M. T.; Bolger, C. T.; Holmes, J. D.; Morris, M. A.; *J. Mater. Chem.*, **2012**, *22, 12083.*

[25] Mishra, V.; Fredrickson, G. H.; Kramer, E. J.; *ACS Nano*, **2012**, 6, 2629.

[26] Zhang, X. H.; Berry, B. C.; Yager, K. G.; Kim, S.; Jones, R. L.; Satija, S.; Pickel, D. L.; Douglas, J. F.; Karim, A.; *ACS Nano*, **2008**, 2, 2331.

[27] Garcia-Turiel, J.; Jerome, B.; *Colloid Polym. Sci.*, **2007**, 285, 1617.

[28] Mao, H. M.; Hillmyer, M. A.; *Macromolecules*, **2005**, 38, 4038.

[29] Zhao, Y. Y.; Bao, C. G.; Feng, R.; Mason, T. J.; *J. Appl. Polym. Sci.*, **1998**, 68, 1411.

[30] Ho, D. L.; Hammouda, B.; Kline, S. R.; Chen, W. R.; *J. Polym. Sci. Pt. B-Polym. Phys.*, **2006**, 44, 557.

[31] Chen, W. Y.; Zheng, J. X.; Cheng, S. Z. D.; Li, C. Y.; Huang, P.; Zhu, L.; Xiong, H. M.; Ge, Q.; Guo, Y.; Quirk, R. P.; Lotz, B.; Deng, L. F.; Wu, C.; Thomas, E. L.; *Phys. Rev. Lett.*, **2004**, 93, 028301.

[32] Michler, G. H.; *Electron Microscopy of Polymers* Springer, **2008**.

[33] O'Driscoll, B. M. D.; Griffiths, G. H.; Matsen, M. W.; Hamley, I. W.; *Macromolecules*, **2011**, 44, 8527.

[34] Martin, C. R.; Aksay, I. A.; *J. Electroceram.*, **2004**, 12, 53.

[35] Prakash, R.; Choudhary, R. J.; Chandra, L. S. S.; Lakshmi, N.; Phase, D. M.; *J. Phys.-Condes. Matter*, **2007**, 19.

[36] Mills, P.; Sullivan, J. L.; *J. Phys. D-Appl. Phys.*, **1983**, 16, 723.

[37] Fujii, T.; de Groot, F. M. F.; Sawatzky, G. A.; Voogt, F. C.; Hibma, T.; Okada, K.; *Physical Review B*, **1999**, 59, 3195.

[38] Peng, K. Q.; Wu, Y.; Fang, H.; Zhong, X. Y.; Xu, Y.; Zhu, J.; *Angew. Chem.-Int. Edit.*, **2005**, 44, 2737.

In order to maintain Moore's Law, it appears to be necessary to introduce some form of self-assembly process. Block copolymer lithography is the most promising of the various self-assembly techniques and is cost-effective and scalable. However, block copolymer structures typically have a large number of defects and lack long-range order. Further, some of the processing is slow and in this thesis, we tried to respond to this particular challenge with our attempts to reduce the phase separation time from hours to less than a minute using a non-conventional microwave technique. In this thesis, we also demonstrated fabrication of well determined silicon nanostructures was demonstrated using three different block polymers: PS-*b*-PDMS, PS-*b*-PMMA and PS-*b*-PEO.

In chapter two and three, silicon nanostructures were fabricated using PS-*b*-PDMS block copolymer. The choices of the interfacial layer between the substrate and the polymer is critical and we showed that a HMDS layer offers some advantage in terms of an increase in coherence length and lower defect density compared to a conventional brush layer. In the next chapter, in order to reduce the processing time, a non-conventional microwave assisted technique was used for nanopattern fabrication using PS-*b*-PMMA and PS-*b*-PDMS block copolymers. In the microwave assisted technique, the main advantage is that the processing time has been reduced to a few seconds compared to conventional thermal annealing and this may allow development of processes to facilitate the introduction of this technique in industry. In the last two chapters the PS-*b*-PEO block copolymer is used to fabricate large area ordered vertically and horizontally aligned silicon nanowires and nanopillars. Here an iron oxide hard mask was used to increase the aspect ratio of the nanopatterns which may can be an important component in the manufacturing of nanoscale devices with high throughput and low cost. Perhaps the most valuable work in this thesis does not centre only on pattern formation, but rather realizing these patterns as valuable substrates via pattern transfer. A constant theme to all of this work has been use of etch processes and we have pioneered this aspect of research and made a valuable contribution to the field.

Bottom-up, chemical nanopatterning, nanophase separation, all common expressions amongst a myriad of terms used to describe potential techniques for how surfaces and substrates can be nanoengineered without the use of physical methods

such as lithography. Despite the promise of this approach there are relatively few examples where self-assembly has had a real impact in a commercial sense. One clear example has been the development of mesoporous materials that are manufactured for chromatography and sorption applications **[1]**.

Indeed, self-assembly has been closely associated with nanotechnology and the development of nanosized electronic devices and, apart from some demonstrators, the goal of having arrays of devices formed by self-assembly has yet to be achieved **[2]**. However, one form of self-assembly/organization is moving rapidly towards device manufacture. Block copolymer nanolithography is becoming a viable, scalable and realizable method for line space (interconnects, devices) and contact hole (via) patterning at ultra-small feature sizes **[3, 4]**. However, if block copolymer lithography techniques are to be implemented into a commercially viable fabrication process, we must have control over the defect structures and long-range lateral order in the thin films. Here, using techniques such as grapho- and chemi-epitaxy, the microphase separation of BCPs can achieve extremely ordered arrangements through chemical interactions between the constituent polymer blocks. The polymer patterns can be integrated into current fabrication schemes as a non-UV lithographic on-chip etch mask provided one block in the pattern can be selectively removed.

The work in BCP nanolithography has been driven by the challenges, financial and technical, in providing sub 8 nm resolution in transistor circuitry and has dominated academic and industrial research in this area **[4]**. However, we have learned a great deal about how these patterns can be achieved, morphology and structural control as well as choices of polymers and how a range of materials can be realized **[3, 4]**. It is worthwhile saying that these methods are capable of varying a widespread form of surface engineering across a range of industries. They may be a way of using lithographic type surfaces in other low-cost industries. Outside their electronic fabrication uses, their applications in fields that require patterning of sub 50 nm feature size in a range of materials has been somewhat neglected despite their low cost. Outside microelectronics, the need for absolute precise positioning and dimensional regularity are somewhat reduced. Indeed, the challenges in terms of their commercial integration move from precision related problems to:-

a) Realizing patterns in different materials (i.e. Si, III-Vs, metal oxides, metals),

b) Developing processes to reduce the defect densities in block copolymer thin film that leads a way to implement this process in industries,

c) Extension to other substrates such as glass, polymer, metal,

d) Developing routes around low capital investment requirements that allow fabrication at smaller scale and low cost,

e) Using these materials to generate patterned functionality.

These materials might generate nanopatterned applications in a number of ways.

The most obvious application of these structured materials is to use the continuous block morphologies to create membrane structures of controlled nanoporous structures by one block removal. The formation and structure of these has been detailed elsewhere and they have applications in size selective filtration, particle growth and even selective crystal phase development **[5]**. The key to these materials, since relatively thick films are usually required, is often to develop wet etches that can selectively remove one block by either designing blocks that are cross-linkable to prevent chemical attrition or blocks that have groups prone to scission. Block copolymer structures can also be used directly as photonic crystals and in applications based on the properties of these materials **[6]**. They can also be modified by inclusion of inorganics such as TiO_2. In the simplest form of application, they can be used as e.g. solvent sensors where solvent swelling induces periodicity changes that sponsors colour changes but temperature, pH and molecular detection is all possible. A related but somewhat different interesting application of block copolymer films is as superhydrophobic surfaces **[7]**. Here, the nanosized structure and inherent polymer hydrophobicity combine to give surfaces which will not wet and have applications in areas such as anti-biofouling surfaces.

Other applications make use of the ability of block copolymers to pattern materials by deposition or targeted inclusion. An obvious application is sensing where the small feature size obtainable provides high surface area for sorption. In our laboratories we have fabricated highly sensitive ethanol, hydrogen peroxide and other electrochemical sensors by using the selected infiltration route to generate iron oxide nanodots on indium-tin-oxide (ITO) surfaces. Briefly, a polystyrene-b-poly ethylene oxide (PS-*b*-PEO) hexagonal forming BCP was deposited onto an ITO surface to create vertical PEO cylinders that were exposed to iron solutions and

processed to yield the iron oxide array. The sensor prepared in this way showed good linear sensitivity and performance equivalent to more expensively prepared materials. In another application, copper was deposited into polystyrene-b-polymethylmethacrylate templates to create copper based capacitors with possible applications in energy storage **[8]**. As a final example we have used a similar method to that described above for iron oxide nanodots to create silver metal nanodots for antimicrobial application.

Thus, it is clear that block copolymer nanopatterning can be highly effective in a range of applications including nanoelectronic device fabrication. The ability to pattern at very small scale, the materials options available and the low cost make this an important platform technique of nanopatterning engineering.

References

[1] Farrell, R. A.; Petkov, N.; Morris, M. A.; and Holmes, J. D.; *J. Coll. Interface Sci.*, **2010**, 349, 449.

[2] Lee. Y. S.; *J Wiley and Sons, Hobroken, New Jersey*, **2011**.

[3] Farrell, R. A.; Fitzgerald, T. G.; Borah, D.; Holmes, J. D.; and Morris. M. A.; *J. Mol. Sci.*, **2009**, 10, 3671.

[4] Jeong, S-J.; Young Kim, J.; Hoon Kim, B.; Moon, H-S.; Ouk Kim. S.; *Materials Today*. **2013**, 16, 468.

[5] Hillmyer. M.; *Adv. Poly. Sci.*, **2008**, 190, 137.

[6] Wang, H.; Zhang. K-Q.; *Sensors*, **2013**, 13, 4192.

[7] Tung, P-H.; Kuo, S-W.; Jeong, K-U.; Cheng, S. Z. D.; Huang, C-F.; *Macromolecular Rapid Communications*, **2007**, 28, 271.

[8] Rasappa, S.; Borah, D.; Senthamaraikannan, R.; Faulkner, C. C.; Holmes, J.D.; dnd Morris. M. A.; J. Nanosci. Nanotechnol, **2014**, 14, 5221.

Appendix I

Chapter 4: Supporting information

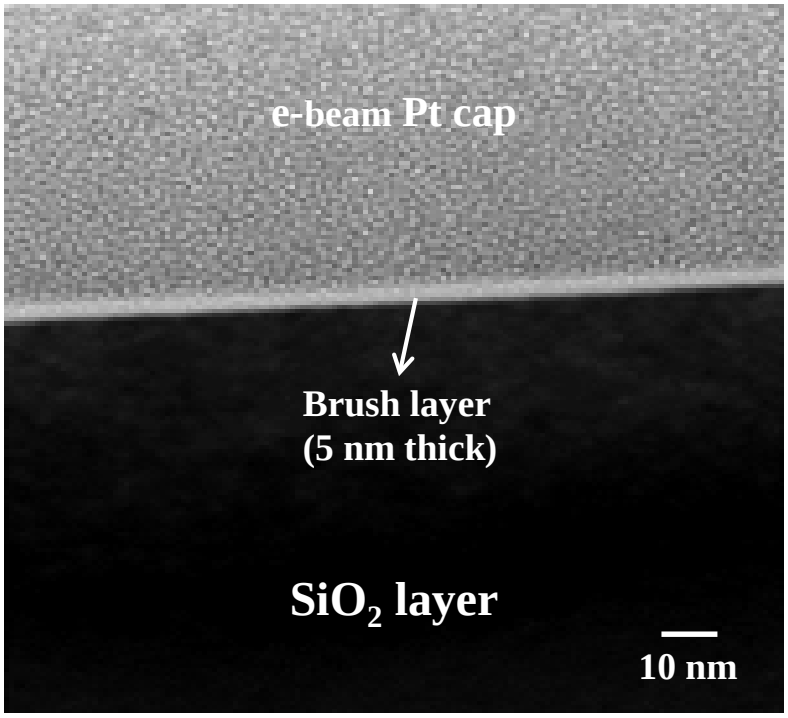

Figure AI.1. TEM cross-section image of polymer brush: TEM cross-section image of polymer brush, HO-PS-*r*-PMMA layer anchored to silicon substrate. The polymer brush was deposited from a 1.0 wt. % solution of the polymer in toluene and thermally annealed at 443 K for 6 h and subsequently cleaned by sonicating and rinsing in toluene. It shows the good uniformity and coverage (95 to 100% of substrate surface) of the methodology used here with a brush layer thickness of ~5 nm. Polystyrene and polymethylmethacrylate adopt a random coil structure and is modelled by $\langle h^2 \rangle_0 = M_w * 0.43$ and $\langle h^2 \rangle_0 = M_w * 0.42$ respectively, where $\langle h^2 \rangle 0$ is the mean-square end-to-end distance of the polymer coil and M_w is the molecular weight **[1]**. The random coil size can be estimate at about 7 nm which is in reasonable agreement with the measured brush layer thickness by ellipsometery and from TEM cross-section since some surface strain/relaxation in the thin film is expected. Assuming $\langle h^2 \rangle_0 = M_w * 0.425$ for PDMS-OH, the value estimated is 4.6 nm and measured at 4.3 nm. This would suggest that a complete monolayer of polymer molecules is formed from the brush procedure used here and provides an excellent surface for block copolymer deposition.

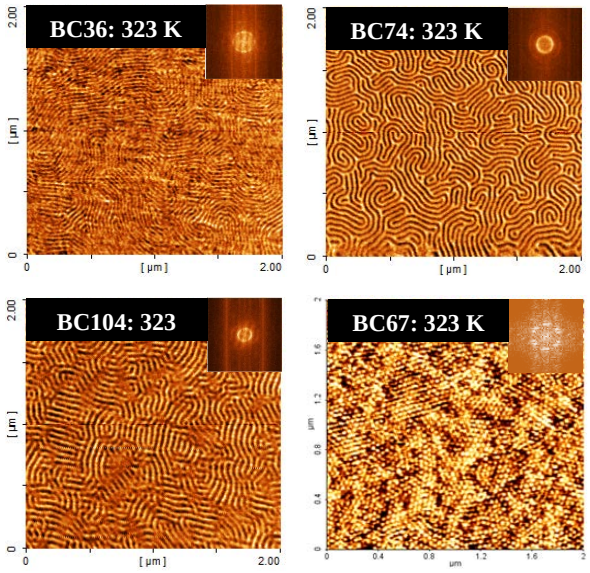

Figure AI.2. AFM topography images of PS-*b*-PMMA BCP films: *2-D* Tapping mode AFM topography images (inset, FFTs of topography images) of microwave annealed PS-*b*-PMMA BCP films of various molecular weights (BC36, BC74, BC104 and BC67) deposited on HO-PS-*r*-PMMA polymer brush coated silicon substrates. The BCP films were microwave annealed at a target temperature of 323 K for 60 s.

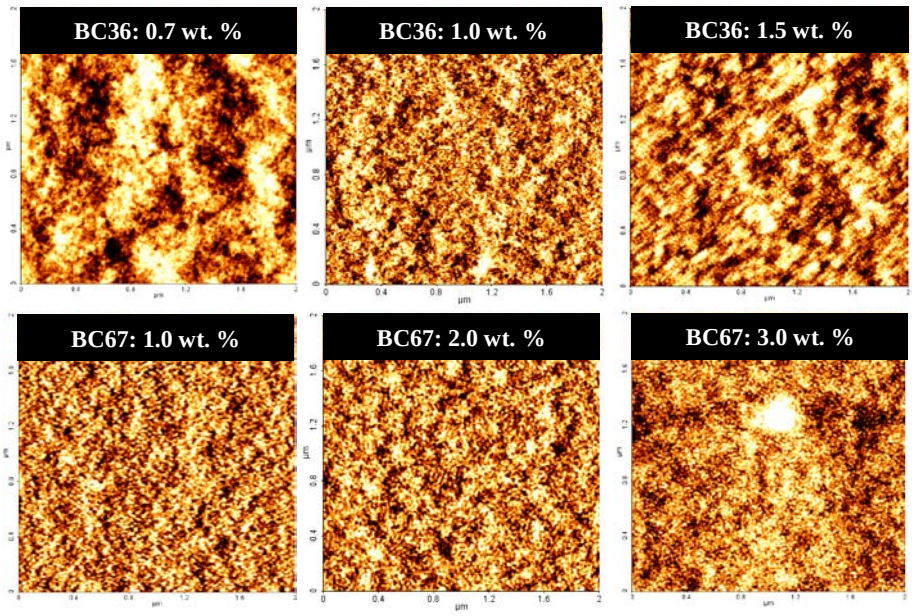

Figure AI.3. Effect of BCP film thickness: *2-D* Tapping mode AFM topography images of thermally annealed PS-*b*-PMMA BCP films of various molecular weights (BC36 and BC67) deposited on HO-PS-*r*-PMMA polymer brush coated silicon substrates. The BCP film thicknesses were varied as labelled in the images and the samples were thermally annealed at 323 K for 60 s.

Figure AI.4. Effect of anneal time: *2-D* Tapping mode AFM topography images of thermally annealed PS-*b*-PMMA BCP films of various molecular weights (BC36, BC74, BC104 and BC67) deposited on HO-PS-*r*-PMMA polymer brush coated silicon substrates. Top-down SEM images of thermally annealed PS-*b*-PDMS BCP films after plasma removal of the top PDMS wetting layer and partial PS matrix, (light grey lines are PDMS and darker lines/holes are voids created following PS removal). Prior to thermal anneal, the PS-*b*-PDMS BCP films were deposited on PDMS-OH polymer brush coated silicon substrates. All the BCP films were thermally annealed at a target temperature of 323 K for different time periods as labelled in the images.

Figure AI.5. Effect of anneal temperature: *2-D* Tapping mode AFM topography images of thermally annealed PS-*b*-PMMA BCP films of various molecular weights (BC36, BC74, BC104 and BC67) deposited on HO-PS-*r*-PMMA polymer brush coated silicon substrates. Top-down SEM images of thermally annealed PS-*b*-PDMS BCP films after plasma removal of the top PDMS wetting layer and partial PS matrix, (light grey lines are PDMS and darker lines/holes are voids created following PS removal). Prior to thermal anneal, the PS-*b*-PDMS BCP films were deposited on PDMS-OH polymer brush coated silicon substrates. All the BCP films were thermally annealed at a target temperature as labelled in the images for 60 s.

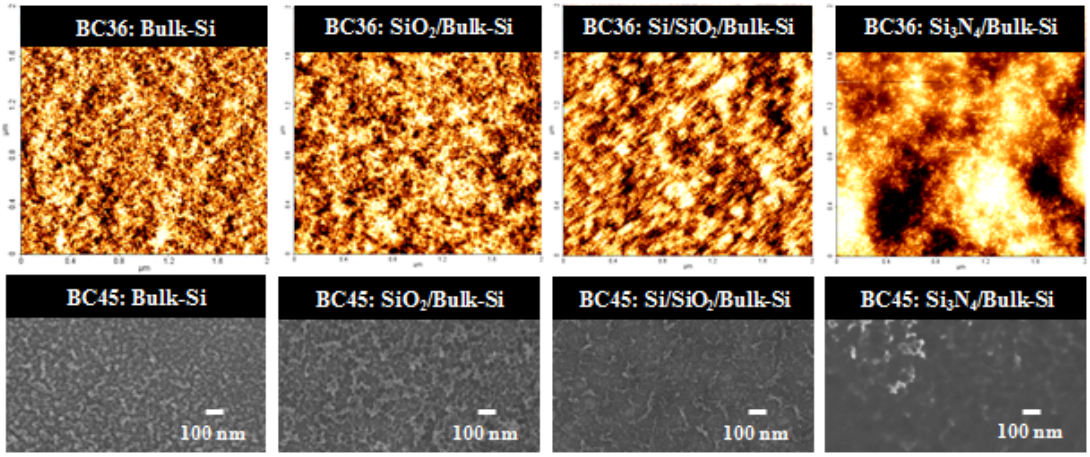

Figure AI.6. Effect of substrate surface type: *2-D* Tapping mode AFM topography images of thermally annealed PS-*b*-PMMA BCP (BC36) films deposited on HO-PS-*r*-PMMA polymer brush coated substrates of different types as labelled in the images. Top-down SEM images of thermally annealed PS-*b*-PDMS BCP films after plasma removal of the top PDMS wetting layer and partial PS matrix, (light grey lines are PDMS and darker lines/holes are voids created following PS removal). Prior to thermal anneal, the PS-*b*-PDMS BCP films were deposited on PDMS-OH polymer brush coated silicon substrates. All the BCP films were thermally annealed at a target temperature of 323 K for 60 s.

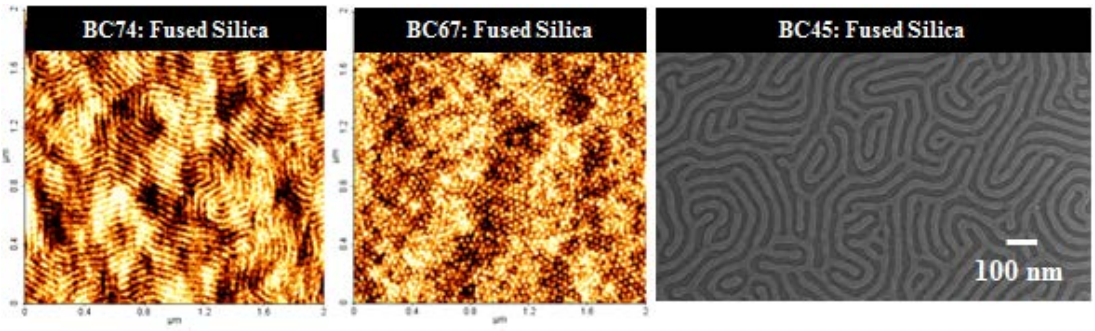

Figure AI.7. Microwave assisted self-assembly on fused silica substrates: *2-D* Tapping mode AFM topography images of microwave annealed PS-*b*-PMMA BCP films of two molecular weights (BC74 and BC67) deposited on HO-PS-*r*-PMMA polymer brush coated fused silica substrates. Top-down SEM image of microwave annealed PS-*b*-PDMS BCP (BC45) film after plasma removal of the top PDMS wetting layer and partial PS matrix, (light grey lines are PDMS). Prior to microwave anneal, the PS-*b*-PDMS BCP film was deposited on PDMS-OH polymer brush coated on fused silica substrate. All the samples were microwave annealed at a target temperature of 323 K for 60 s.

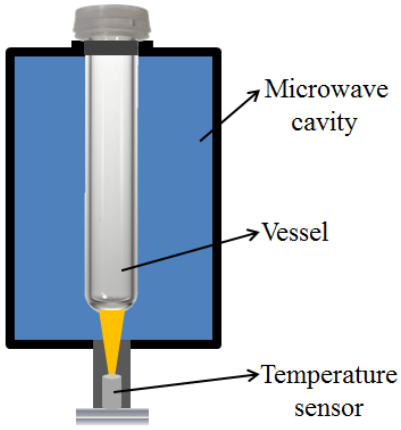

Scheme AI.1. Temperature sensor in microwave chamber: Schematic showing the microwave chamber with temperature sensor that records the temperature profile during microwave anneal.

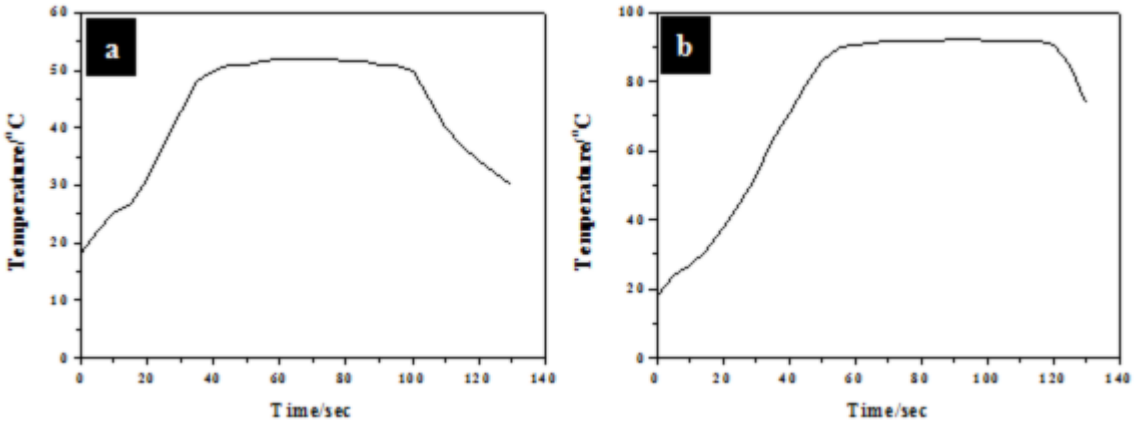

Figure AI.8. Temperature profiles during microwave anneal: Representative temperature profiles of the (BCP + substrate) system at **(a)** 323 K and **(b)** 363 K for 60 s.

References

[1]. Matsushita, Y.; Mori, K.; Saguchi, R.; Nakao, Y.; Noda, I.; Nagasawa, M. Molecular Weight Dependence of Lamellar Domain Spacing of Diblock Copolymers in Bulk. *Macromolecules* **1990**, *23*, 4313.

Appendix II

Chapter 6: Supporting information

Variation of film thickness

The film thickness can be varied by varying the concentrations of the polymeric solution which increases with increasing the concentrations. **Figure AII.1** shows the microscopic images of the 1.0 wt. %, 2.0 wt. % and 3.0 wt. % polymeric films after solvent annealing in toluene for 2 h 30 min respectively. Thinner film (**Figure AII.1(a)**) shows lighter contrast compared to the thicker films. Further, smooth surface was observed. The thickness dissimilarity and wavy nature of the film surface was evident from **Figures AII.1(b)** and **AII.1(c)** for thicker films.

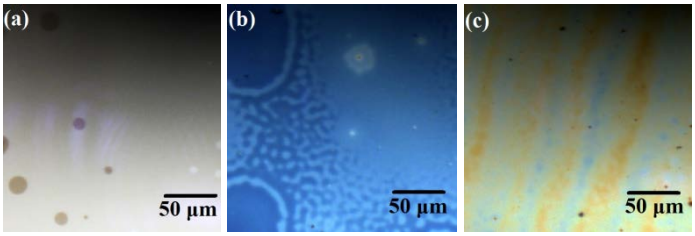

Figure AII.1. Microscopic images of 1.0 wt. %, 2.0 wt. % and 3.0 wt. % polymeric films after solvent annealing for 2 h 30 min.

Solvent annealing for thicker films

For thicker films (2.0 wt. % and 3.0 wt. %), parallel and perpendicular cylinders coexist with parallel orientation as a major assembly for longer annealing time (2 h 30 min). Topographic AFM images (**Figures AII.2(a)** and **AII.2(b)**) confirm long line-like patterns but thickness variation is noticed.

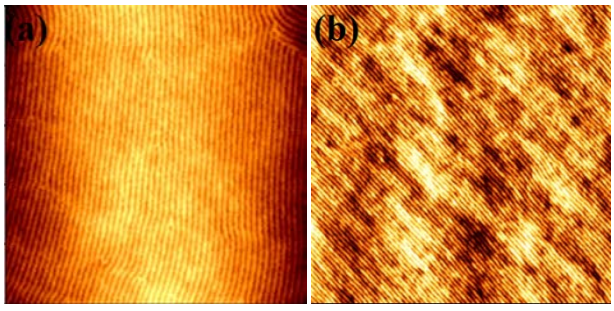

Figure AII.2. AFM images of 2.0 wt. % and 3.0 wt. % polymeric films after solvent annealing for 2 h 30 min. Scale bar: **(a)** 2 x 2 µm. **(b)** 3 x 3 µm.

Nanoporous templates after ethanol treatment

Figures AII.3(a) and **AII.3(b)** demonstrate that the ethanol treatment is well effective to create nanoporous template for a variety of PEO cylinder length for 2.0 wt. % and 3.0 wt. % polymeric film respectively. The films were immersed in ethanol for 21 h.

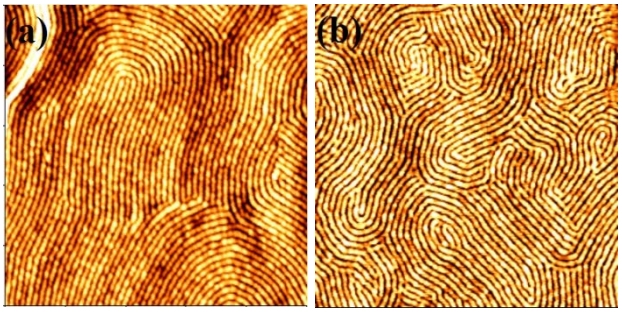

Figure AII.3. AFM images of the **(a)** 2.0 wt. % and **(b)** 3.0 wt. % polymeric film after ethanol treatment for 21 h.

TEM cross-sectional image of the PS-PEO thin film before ethanol treatment

It is not possible to reveal the arrangement of PS and PEO in the non-ethanol treated film due to lack of contrast difference between them as the density of PS (1.05 g cm^{-3}) and amorphous PEO (1.12 g cm^{-3}) are similar shown in **Figure AII.4**. The thickness of the film is 40 nm.

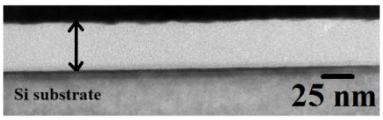

Figure AII.4 TEM cross-sectional image of the PS-PEO solvent annealed thin film for 1.0 wt. % polymeric solution.

Preparation of iron oxide nanowire arrays, concentration and aging effect

The iron nitrate precursors were dissolved in anhydrous ethanol and spin coated onto the nanoporous template. The solution was stirred for 30 min to prepare a homogeneous solution. **Figure AII.5(a)** and **AII.5(b)** shows the AFM images of iron oxide prepared after UV/Ozone treatment for the solution stirred for 2 h and 24 h. Though the nanowires follow a certain pathway, it experiences a high density of defects and aggregated particles all over the substrate. The anhydrous ethanol has a tendency to absorb moisture from the atmosphere. While stirring the solution for

longer time, the precursor started to oxidize at room temperature and smaller nanoparticles formed. As a result of anisotropic dipolar attraction, pristine nanoparticles of iron oxides tend to aggregate into large clusters with time.

The concentration of the precursor solution is also another important factor for the large scale fabrication of defect-free nanostructures. For a smaller concentration of 3.5 wt. %, discontinuous and smaller diameter nanowires are observed (**Figure AII.5(c)**). With increasing the concentration to a certain value, the adjacent segments of the nanowires started to coalesce with each other (**Figure AII.5(d)**). Further increment of concentrations leads to agglomerated nanowires all over the substrate (**Figure AII.5(e)** and **AII.5(f)**).

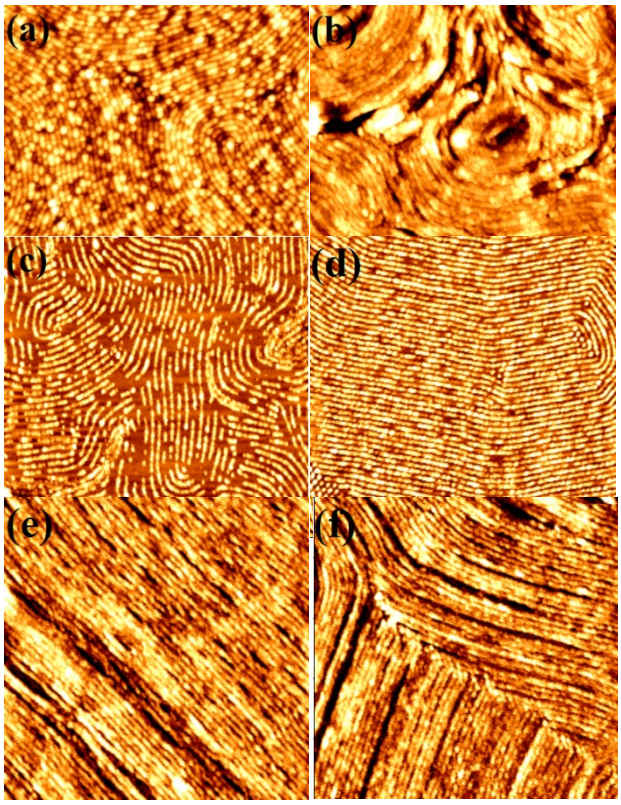

Figure AII.5 Iron oxide nanostructure prepared with 1.0 wt. % polymeric template. The precursor-ethanol solution stirred for **(a)** 2 h and **(b)** 24 h. The concentration of the precursor-ethanol solution is **(c)** 3.5 wt. %, **(d)** 4.25 wt. %, **(e)** 5.0 wt. % and **(f)** 5.5 wt. %.

Cross-sectional TEM image of the nanowire

Figure AII.6 reveals the cross-sectional TEM image of a single nanowire. High resolution image depicts the lattice fringes across the nanowire revealing the crystalline nature.

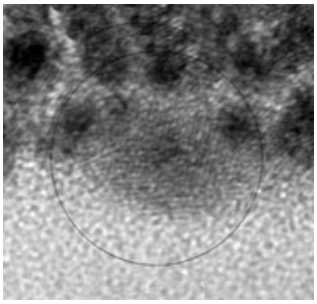

Figure AII.6 Cross-sectional High resolution TEM image of the nanowire.

Pattern transfer through ICP Si etch

Figure AII.7 shows the large area SEM image of the substrate after 3 min Si etch for the iron oxide prepared with a very high concentrations of precursor (10.0 wt. %). No pattern transfer is realized after 3 min etch revealing the applicability of iron oxide as an excellent resistant mask over silicon. Also, identical order nanowire patterns obtained after 5 min Si etch for the nanowires prepared with 4.6 wt. % precursor for the thinner film. The nanowires disconnected only in few places after this longer etch time. Further deeper (250 nm depth) nanowires are evident.

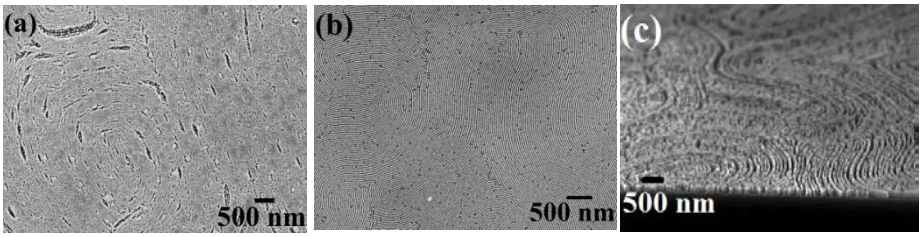

Figure AII.7 SEM images **(a)** after 3 min Si etch for the iron oxide prepared with 10.0 wt. % precursor solution and **(b)** and **(c)** after 5 min Si etch for the nanowires prepared with 4.6 wt. % precursor for the thinner film.